X-ray Birefringence Imaging and Other Fundamental Aspects of Solid Organic Inclusion Compounds

by

GREGORY RICHARD EDWARDS-GAU

Thesis Submitted for

DOCTOR OF PHILOSOPHY

SCHOOL OF CHEMISTRY

CARDIFF UNIVERSITY

September 2014

DECLARATION

This work has not been submitted in substance for any other degree or award at this or any other university or place of learning, nor is being submitted concurrently in candidature for any degree or other award.

Signed …………………………………… (candidate)   Date…………………………

STATEMENT 1

This thesis is being submitted in partial fulfillment of the requirements for the degree of …………………………(insert MCh, MD, MPhil, PhD etc, as appropriate)

Signed …………………………………… (candidate)   Date …………………………

STATEMENT 2

This thesis is the result of my own independent work/investigation, except where otherwise stated.
Other sources are acknowledged by explicit references. The views expressed are my own.

Signed …………………………………… (candidate)   Date …………………………

STATEMENT 3

I hereby give consent for my thesis, if accepted, to be available for photocopying and for inter-library loan, and for the title and summary to be made available to outside organisations.

Signed …………………………………… (candidate)   Date …………………………

STATEMENT 4: PREVIOUSLY APPROVED BAR ON ACCESS

I hereby give consent for my thesis, if accepted, to be available for photocopying and for inter-library loans **after expiry of a bar on access previously approved by the Academic Standards & Quality Committee.**

Signed …………………………………… (candidate)   Date …………………………

Acknowledgements

I would like to thank my supervisor Professor Kenneth D. M. Harris for providing me with guidance and support throughout my PhD. Furthermore working in has research group has been very stimulating and led to many interesting research opportunities.

I am thankful to the Diamond Light Source synchrotron for providing beamtime to conduct these experiments. In particular I would like to thank Professor Stephen Collins, Dr. Igor Dolbnya whose knowledge and technical expertise proved invaluable both in acquiring data and in interpreting it.

I am thankful to UK 850 MHz Solid-State NMR Facility for providing access to their 850 MHz solid-state spectrometer for this research, and I acknowledge Dr. Dinu Iuga in particular for his assistance.

I am thankful to Dr. Benson Kariuki for his single-crystal X-ray diffraction work and his insight on crystal structures.

I am thankful to all members of the Harris research group, past and present, for being good friends and good colleagues. Specifically I would like to mention Dr. Benjamin Palmer, Dr. Colan Hughes, Dr. Phillip Andrew Williams, Dr. Yuncheng Yan, Dr. Keat Lim, Dr Vasileios Charalampopoulos and Victoria Keast.

I am thankful to my parents for their help and unwavering support over the course of my PhD.

Finally I would like to acknowledge Cardiff University and the EPSRC for their funding and financial support to make all of this possible.

Abstract

This thesis presents new experimental techniques and utilizes these strategies in the analysis of solid organic inclusion compounds. This thesis also reports the production of a new series of co-crystals and examines their crystal structures.

Chapter 1 acts as an introduction to the materials studied in this research. It explains the properties of inclusion compounds and lists the chemical materials used for these experiments.

Chapter 2 explains the experimental techniques used in this research. Specifically it explains X-ray diffraction, X-ray birefringence and *in-situ* solid-state NMR.

Chapter 3 presents a new technique for spatially resolved mapping of specific bond orientations in anisotropic solid materials using wide beam linearly polarized X-rays and an area detector. Earlier work with a focussed beam and a point detector showed the sensitivity of X-ray Birefringence to the orientation of specific energy-matching bonds inside a material, but these experiments only probed a small section of the crystal. Our wide beam imaging technique (X-ray Birefringence Imaging) shows similar sensitivity but allows us to investigate the full crystal simultaneously, which allows us to identify different domains within a single crystal. We apply this technique to a model material (1-bromocyclohexane/thiourea) which undergoes a low temperature phase transition and serves to demonstrate the usefulness of imaging techniques - in the high temperature phase the relevant C−Br bonds are isotropically disordered and no birefringence is observed, in the low temperature phase the relevant C−Br bonds are ordered but there are three possible orientations for the bromocyclohexane molecule so different regions of the crystal exhibit different birefringent signal. This behaviour is very clear on an imaging technique, but can appear highly confusing when using point-detector techniques.

Chapter 4 utilizes X-ray Birefringence Imaging to investigate the dynamic rotational properties of guest molecules in a different set of solid organic inclusion compounds. By studying the known structures of 1,10-dibromodecane/urea and 1,8-dibromooctance/urea we have determined that XBI is a time-averaged and space-averaged

technique. Additionally this chapter utilizes a Ge(555) analyzer instead of the Si(555) analyzer, which results in better spatial resolution and a different beam shape on the final images.

Chapter 5 utilizes solid-state in-situ NMR to monitor crystallization processes as they occur and gain insight on competitive uptake of different guest molecules within the inclusion compound. These experiments use alkane and α,ω-dibromoalkane guest molecules inside urea inclusion compounds where the urea host structure (created in-situ) acts like a one-dimensional tunnel confining the guest. Every position within the urea tunnel is equivalent (a property of the incommensurate structure) which serves to simply the solid-state NMR spectra and means that for a given atom at the end of an alkane chain the only difference in NMR site comes from the neighbour molecule along the tunnel. This means in the solid phase we can observe peak splitting on certain atoms based on neighbour environment (e.g. the -$\underline{C}H_3$ in undecane will give a slightly different chemical shift if the neighbouring guest molecule is another undecane compared to if the neighbouring guest molecule is 1,8-dibromooctane) which in turn allows us to extract some information about the ordering within the inclusion compound. In these experiments we can also clearly distinguish between the same molecules in different phases, so as crystallization occurs we observe the loss of solution signal alongside the gain of solid signal. Additionally these experiments show no evidence of any intermediate structures or transition states.

Chapter 6 describes a new set of organic co-crystals formed by reacting thiourea with α,ω-diiodoalkane chains and examines the crystal structures of these materials.

Chapter 7 details further work and potential applications of this research.

Digital data includes animated videos of the X-ray birefringence imaging data obtained in Chapter 3 and CIF files of the structures determined in Chapter 6.

Table of Contents

Chapter 1 – Introduction

1.1 Inclusion Compounds

In physical chemistry the properties of a material depend not only on its chemical structure but also on the spatial arrangement of its molecules. This is most readily apparent with the phenomenon of polymorphism where the same chemical compound may exhibit different melting points, solubilities and biological activities based on its crystallographic arrangement, but it is also a fundamental consideration with inclusion phenomena. Confining one chemical species (the guest) inside another (the host) can result in a material with physical properties that differ substantially from the properties of either pure compound, without a chemical reaction taking place.

The wide variety of possible guests and possible hosts give inclusion compounds a huge number of potential combinations which in turn may give a broad range of structures and properties. In addition to this great diversity inclusion compounds also offer a degree of predictability – a specific host may produce a series of inclusion compounds with very similar structures and these structures may exert obvious size or shape constraints upon the guest. As host guest association depends on non-covalent interactions rather chemical bonding it is often reversible and proceeds under very mild conditions. This useful behaviour is why inclusion compounds are an avenue worthy of investigation.

The earliest reports of inclusion phenomena come from the 18th century with the discovery of zeolites [1] and clathrate hydrates [2, 3.] Subsequent research discovered graphite intercalates [4], cyclodextrin inclusion compounds [5], and choleric acid inclusion compounds [6] but this early work was stymied by the difficulties determining the structural features of these materials.

These materials remained as oddities for many years and it was only following the advent of X-ray diffraction that these structures would be resolved [7-14]. These crystal

structures demonstrated instances of host-guest association and led to many studies of inclusion phenomena [15] and their possible applications.

As inclusion compounds encompass a wide range of different materials it is useful to group them into subcategories based on their properties. The broadest measure is to split inclusion compounds into: i) molecular inclusion compounds, where the host is a molecule with a cavity or opening capable of including the guest, ii) solid inclusion compounds, where the host molecules self-assemble into a framework which can include the guest.[16-18]. These solid inclusion compounds can be further sub-divided into hard host inclusion compounds, where removal of the guest results in a stable empty framework, and soft host inclusion compounds, where removal of the guest results in collapse of the host solid.

Molecular inclusion compounds typically exhibit host-guest association in both the solution and solid states, and example hosts are crown ethers, cryptands, cyclodextrins and calixarenes.

Solid inclusion compounds only exhibit host-guest association in the solid state. Example hard hosts are aluminosilicates, aluminophosphates, metalloaluminophosphates, cyclophosphazenes, metal chalcogenides, and metal phosphonates). Example soft hosts are urea, thiourea, tri-ortho-thymotide, deoxycholic acid, cholic acid and perhydrotriphenylene.

Inclusion phenomena are utilized in many fields but often slightly different terminology is used. This thesis consistently refers to these materials as inclusion compounds but other work may call them inclusion complexes, host-guest complexes, clathrates or frameworks.

The materials used in this project are shown in Fig. 1.1. In Chapter 3 thiourea has been used as host for bromocyclohexane and 1-bromoadamantane guests. In Chapter 4 urea has been used as a host for 1,8-dibromooctane and 1,10-dibromodecane guests (i.e. α,ω-dibromoalkanes 8 and 10 carbons in length). In Chapter 5 urea has been used as a host for undecane, tetradecane 1,8-dibromooctane and 1,12-dibromododecane guests. In

2

Chapter 6 thiourea has reacted with 1,4-diiodobutane, 1,5-diiodopentane, 1,6-diiodohexane, 1,8-diiodooctane and 1,10-diiododecane (i.e. α,ω-diiodoalkanes 4, 5, 6, 8 and 10 carbons in length) to produce co-crystals rather than inclusion compounds.
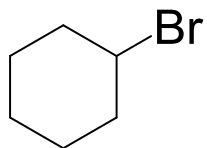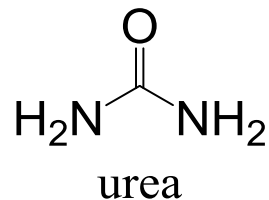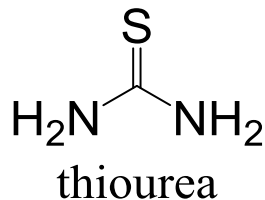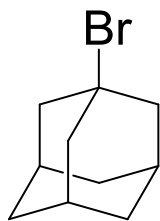
Fig. 1.1 Figure showing the chemicals used in this research.

1.1.1 Urea Inclusion Compounds

Urea inclusion compounds were discovered serendipitously in 1940 [19] by the researcher Bengen. Subsequent work determined that urea forms inclusion compounds with many aliphatic straight-chain hydrocarbons [20, 21] provided they exceed a certain chain length (approximately 5 carbons) and X-ray diffraction experiments have determined their precise structure [22, 23].

Urea inclusion compounds consist of long hexagonal tunnels of urea where the guest is contained within the tunnel. Urea inclusion compounds typically give long needle-shaped colourless crystals where the longer dimension corresponds to the tunnel axis (which tells us that crystal growth is usually faster along the tunnel than in other directions), but flat plate-shaped crystals are possible [24].

Urea inclusion compounds are well characterized and the properties of urea inclusion compounds can be summarized as follows. UICs possess:

- Linear parallel tunnels with a consistent tunnel diameter of 5.5-5.8 Å [24-28] (i.e. roughly cylindrical tunnels).

- Hexagonal shaped linear tunnels (as seen in Fig. 1.2) formed from extensive hydrogen bonding of urea molecules [24-28]. There is little opportunity for hydrogen bonding between the guest and the host [26-28].

- Chiral helixes of urea leading to chiral crystals in the space groups $P6_122$ or $P6_522$ [24-28].

- Substantial dynamic disorder (reorientation about the tunnel axis) of the guest molecules at ambient temperature [24, 26-28].

- Soft-host character. Removing the guest causes the tunnels to collapse and results in crystalline urea [24-28]. Guest replacement processes are still possible but the tunnel must remain filled throughout exchange [24, 26, 29].

- A requirement for long straight-chain guests (>5 carbons in length) [24-28]. Longer guests are more tolerant to branching/substitution [28] and give UICs with higher decomposition temperatures [30]. To prevent solvent inclusion it is best either to use a very small solvent (energetically disfavoured) or a very bulky solvent (unable to fit) [27, 28].

- Properties and behaviour which can be modified significantly by the encapsulated guest molecule [25, 26, 28].

- Low temperature phase transitions of the host structure which prompt changes in the UIC's dynamic properties and a change in symmetry (usually to orthorhombic) [24-28].
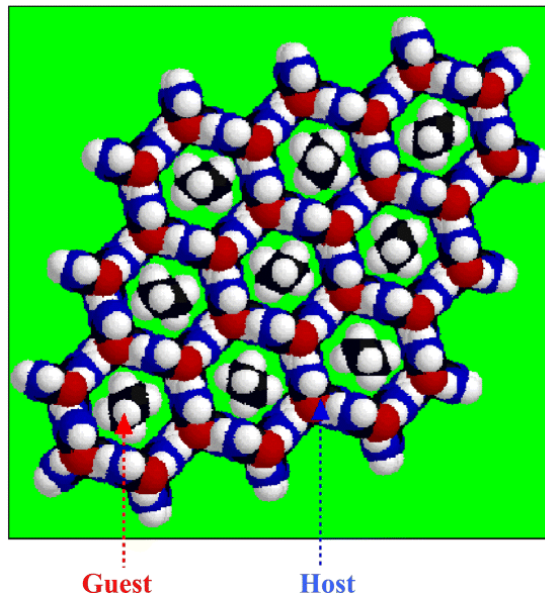
Fig. 1.2 *The hexadecane/urea inclusion compound structure when viewed along the tunnel axis at ambient temperature. Reproduced from reference 24.*

Additionally most urea inclusion compounds adhere to the same "conventional" structure under ambient conditions which show the following properties:

- Lattice parameters $a = b \approx 8.2$ Å, $c \approx 11.0$ Å, $\alpha = \beta = 90°$ and $\gamma = 120°$

- Incommensurate relationship between host periodicity and guest periodicity. Non-conventional commensurate structures do exist with certain guests e.g. $(\alpha+1)(\omega-1)$-alkanediones [25, 26].

Commensurate and incommensurate are terms with many applications but here they are used exclusively to refer to the relationship of periodicities between the host and the guest.

- Disordered - One (or more) of the components lacks a well-defined periodicity therefore precluding any consistent relationship between the two.

- Incommensurate - A well-defined periodicity for the guest and a well-defined periodicity for the host and an irrational relationship between the two. See figure 1.3.

- Commensurate - A well-defined periodicity for the guest and a well-defined periodicity for the host and a rational relationship between the two. See figure 1.4.
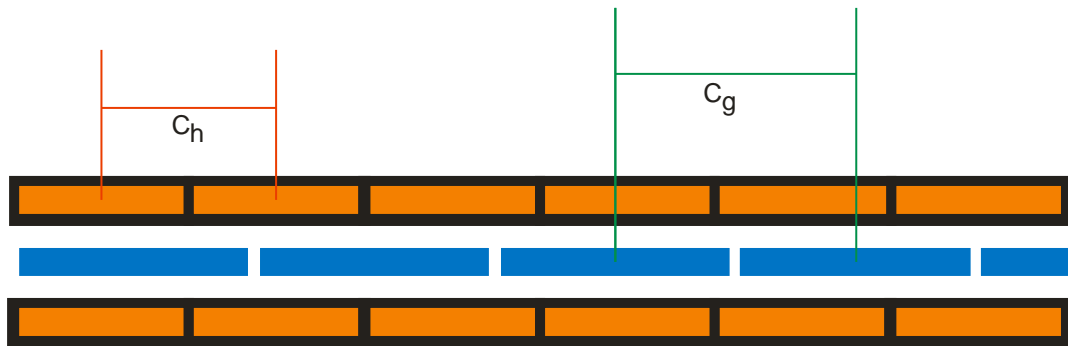
Fig 1.3 *An incommensurate structure. C_h is the periodicity of the host and C_g is the periodicity of the guest, but there is no rational relationship between the two periodicities.*
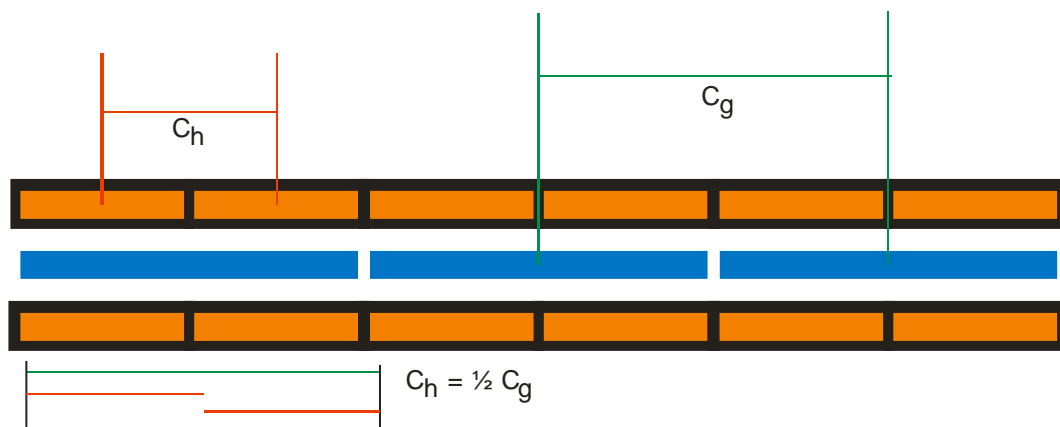
Fig 1.4 *A commensurate structure with $C_h = \frac{1}{2} C_g$. C_h is the periodicity of the host and C_g is the periodicity of the guest and they possess the rational relationship $C_h = \frac{1}{2} C_g$.*

To accommodate for experimental error it is better not to look for a rational relationship and instead to look for anything sufficiently close to a sufficiently small rational relationship. The importance of commensurate and incommensurate guest/host ratios is most easily demonstrated by contrasting UICs with their sulphur analogues – Thiourea Inclusion Compounds (TICs). UICs conventionally give incommensurate relationships but TICs conventionally give commensurate relationships (usually the repeat distance of the guest is half the repeat distance of the host) [25, 28, 31]. In TICs the tunnels are non-uniform and possess distinct contractions (diameter ~5.8 Å) and bulges (~7.1 Å) [24, 25, 27, 28, 31]. The difference in tunnel diameter is so pronounced that the thiourea host framework can be considered a cage-based structure rather than a tunnel structure. So it is apparent that TICs commensurate guest/host relationships arise because thiourea host tunnels influence guest periodicity and guest ordering by having sites that are favoured and disfavoured; i.e. the desires of the guest molecule are mediated by the availability of spatially preferred sites. This serves as an explanation as to why TICs typically give the same commensurate relationship rather than a range of many commensurate relationships.

Incommensurate behaviour leads to guest molecules sampling a range of different environments within the host structure whilst commensurate behaviour leads to guests locking in to specific positions. This results in different energetic properties when guest

molecules are moved along the tunnel, the average host-guest interaction energy per guest molecule will behave differently for commensurate and incommensurate systems. A commensurate structure will give large energy fluctuations whilst an incommensurate structure will give small energy fluctuations (in principle the energy should be constant) [25, 28]. This relationship can be used to determine whether a guest-host structure is commensurate or incommensurate and illustrates why incommensurate structures are an interesting avenue for frictionless transport.

Original interest in urea inclusion compounds stemmed from their applications in chemical separation [32] but their soft-host nature is a disadvantage here and other materials are more widely used for this purpose (e.g. zeolites).

1.1.2 Thiourea Inclusion Compounds

Thiourea inclusion compounds were discovered in 1947 [33], a few years after the discovery of urea inclusion compounds and many similarities can be drawn between the two types of material. Both are soft-hosts which only include guests in the solid state, both consist of linear tunnels held together by hydrogen bonds, both undergo low temperature phase transitions and both allow significant dynamic disorder of guest molecules.

However crucial differences arise when the shape of the tunnel is inspected more closely. UIC tunnels possess a mostly uniform diameter but TIC tunnels have distinct bulges and constrictions (diameter ~5.8 Å to ~7.1 Å) meaning thiourea can form inclusion compounds with bulky guests [34-36] rather than long chains and the presence of different sites within the tunnel encourages commensurate structures (though incommensurate structures are still possible) [37]. This effect is so pronounced that at times it is better to consider TICs as cage like structures rather than tunnel structures as bulkier guests only occupy the preferred sites where the tunnel is at its widest.

The host structure in thiourea inclusion compounds is generally rhombohedral or monoclinic. For guest molecules with a somewhat planar shape (such as 2,6-diethylnaphthalene; 2,3-dimethylbutadiene; and 1,5-cyclooctadiene) typically favour the monoclinic host structure at ambient temperature, with the guest molecules being

constrained in an ordered arrangement. At low temperatures the tunnel often deforms, lowering the symmetry from rhombohedral to monoclinic and forcing greater orientational ordering of the guest molecules. For guest molecules that have isotropic shapes (such as cyclohexane, chlorocyclohexane, and ferrocene), the host structure at ambient temperature is usually rhombohedral, and the guest molecules generally exhibit reorientational dynamics. In many cases, this rhombohedral structure transforms (via one or more solid-state phase transitions) to a monoclinic structure at sufficiently low temperature.

There is more variance in the structures of thiourea inclusion compounds but still a "conventional" host structure can be described. A conventional' thiourea inclusion compounds is rhombohedral in the space group $R\bar{3}c$ and with unit cell parameters of a≈15.5–16.2 Å and c=12.5 Å (hexagonal setting) [38-40]. It exhibits a significant variation in tunnel diameter on moving along the tunnel and guest molecules typically occupy specific sites along the host tunnel. Usually this gives one guest molecule within each ''cage'' in the host structure and corresponding to the commensurate relationship $c_h=2c_g$ (where c_h is the periodic repeat distance of the host structure along the tunnel, and c_g is the periodic repeat distance of the guest molecules along the tunnel). Thus, there are two guest molecules within the periodic repeat distance of the thiourea host structure along the tunnel, leading to a guest/thiourea molar ratio of 1/3. The well-defined positioning of the guest molecules at specific locations within each tunnel gives rise directly to three-dimensional (3-D) positional ordering of the guest molecules controlled by the 3-D periodicity of the host structure.

This cage-like structure grants TICs interesting applications in non-linear optics where the cage is used to direct guests into ordered conformations that would normally be disfavoured [25, 28, 31, 41, 42].

1.3 Aims of this Project

This project aims to:

- **Develop new crystalline materials.**

- **Improve our understanding of inclusion compound crystallization, using *in-situ* solid-state techniques**. Inclusion compounds are well characterized and well understood but still the exact process of crystallization hold some mysteries. *In-situ* techniques monitor a process as it occurs so they are ideal for following crystallization.

- **Pioneer new experimental techniques using inclusion compounds as simplified model systems.** With our knowledge of inclusion compounds we can exploit their well-defined structures in order to study specific guest materials more easily. By confining a guest molecule within a defined tunnel structure we can restrict its possible orientations and create a simpler packing arrangement than is found in the pure guest. By performing initial experiments on a simple material we can improve our understanding of the technique and build up onto more complicated materials.

1.4 References

[1]   A. F. Cronstedt, *Kongl. Vetenskaps Acad. Handl.*, **1756**, 17, 120, Stockholm.
[2]   H. Davy, *Phil. Trans. R. Soc.*, **1811**, 101, 30.
[3]   M. Faraday, *Quart. J. Sci.*, **1823**, 15, 71.
[4]   C. Schafthäutl, *J. Prakt. Chem.*, **1841**, 21, 129.
[5]   A. Villiers, *C. R. Hebd. Acad. Sci.*, **1891**, 112, 536.
[6]   H. Wieland, H. Sorge, *Hoppe-Seyler's Z. Physiol. Chem.*, **1916**, 97, 1.
[7]   D. E. Palin, H. M. Powell, *Nature*, **1945**, 156, 334.
[8]   D. E. Palin, H. M. Powell, *J. Chem. Soc.*, **1947**, 208.
[9]   H. M. Powell, *J. Chem. Soc.*, **1948**, 16, 61.
[10]   D. E. Palin, H. M. Powell, *J. Chem. Soc.*, **1948**, 2, 571.
[11]   D. E. Palin, H. M. Powell, *J. Chem. Soc.*, **1948**, 815.

[12]   H. M. Powell, *J. Chem. Soc.*, **1950**, 298.

[13]   H. M. Powell, *J. Chem. Soc.*, **1950**, 300.

[14]   H. M. Powell, *J. Chem. Soc.*, **1950**, 468.

[15]   E. Weber, *Top. Curr. Chem.*, **1987**, 140, 1.

[16]   D. D. MacNicol, J. J. McKendrick, D. R. Wilson, *Chem. Soc. Rev.*, **1978**, 7, 65.

[17]   K. D. M. Harris, in M. W. Roberts (Ed), *Monographs on Chemistry for the 21st Century: Interfacial Chemistry*, **1997**, 21, I.U.P.A.C./Blackwell Science, Oxford.

[18]   L. R. Nassimbeni, *Acc. Chem. Res.*, **2003**, 36, 631.

[19]   M. F. Bengen, *Ger. Pat. Appl.*, **1940**, OZ 123438.

[20]   M. F. Bengen, W. Schlen, *Experientia*, **1949**, 5, 200.

[21]   M. F. Bengen, *Angew. Chemie.*, **1951**, 63, 207.

[22]   A. E. Smith, *Acta Crystallogr.*, **1952**, 5, 224.

[23]   K. D. M. Harris, J. M. Thomas, *J. Chem. Soc., Faraday Trans.*, **1990**, 86, 2985.

[24]   K. D. M. Harris, *Supramolecular Chem.*, **2007**, 19, 47-53.

[25]   K. D. M. Harris, *Chem. Soc. Rev.*, **1997**, 26, 279-289.

[26]   K. D. M. Harris, in J. W. Steed, J. L. Attwood, (Eds.), *Encyclopedia of Supramolecular Chemistry*, **2004**, 1538-1549, Marcel Dekker, New York.

[27]   K. D. M. Harris, *J. Mol. Struct.*, **1995**, 374, 241-250.

[28]   M. D. Hollingsworth, K. D. M. Harris, in D. D. MacNicol, F. Toda, R. Bishop, (Eds.), *Comprehensive Supramolecular Chemistry*, **1996**, 6, 177-238, Pergamon Press, Oxford.

[29]   M. Marti-Rujas, A. Desmedt, K. D. M. Harris, F. Guillaume, *J. Phys. Chem.*, **2009**, 374, 241-250.

[30]   T. Nakaoki, H. Nagano, T. Yanagida, *J. Mol. Struct.*, **2004**, 699, 1-7.

[31]   K. D. M. Harris, in J. W. Steed, J. L. Attwood, (Eds.), *Encyclopedia of Supramolecular Chemistry*, **2004**, 1501-1507, Marcel Dekker, New York.

[32]   V. M. Bhatnagar, *Clathrate Compounds*, **1962**, 10, Chemical Publishing Co. Inc., New York.

[33]   B. Angla, *Compt. Rend.*, **1947**, 224, 1166.

[34]   L.C. Fetterly, in L. Mandelcorn, (Ed.), *Non-Stoichiometric Compounds*, **1964**, 491 Academic Press, New York.

[35]   J. F. Brown, D. M. White, *J. Am. Chem. Soc.*, **1960**, 82, 5671.

[36]   K. Takemoto, N. Sonoda, in J. L. Attwood, J. E. D. Davies, D. D. MacNicol, (Eds.), *Inclusion Compounds*, **1984**, 2, 47.Academic Press: London,

[37]   B. A. Palmer, B. M. Kariuki, V. K. Muppidi, et al., *Chemical Communications*, **2011**, 47, 13, 3760-3762.

[38]   H.-U. Lenné, *Acta Crystallogr.*,**1954**, 7, 1.

[39]   K. D. M. Harris, J. M. Thomas, *J. Chem. Soc., Faraday Trans.,* **1990**, 86, 1095.

[40]   E. Hough, D. G. Nicholson, *J. Chem. Soc., Dalton Trans.*, **1978**, 15.

[41]   W. Tam, D. F. Eaton, J. C. Calabrese, I. D. Williams, Y. Wang, A. G. Anderson, *Chem. Mater.* **1989**, 1, 128-140.

[42]   K. D. M. Harris, P. E. Jupp, *Chem. Phys. Lett.* **1997**, 274, 525-534.

Chapter 2 – Experimental Methods

This chapter explains the scientific techniques used in these experiments and describes the underlying theory behind them. Specifically it gives details for X-ray diffraction (XRD), Solid-State Nuclear Magnetic Resonance spectroscopy (SS NMR), and X-ray Birefringence.

2.1 X-Ray Diffraction

X-Ray Diffraction (XRD) is an extremely powerful tool for determining crystal structures and provides direct information on atom positions and bond lengths[1], in contrast with other solid state techniques which provide energetic information to be related back to crystallographic meaning. X-Ray Diffraction is only suitable for studying crystalline solids and is a non-destructive time-averaged and space-averaged technique. These properties make XRD representative of the bulk of a material but make it less sensitive to defects or surface effects. Defects do not produce diffraction peaks but they can result in peak broadening and stacking faults, therefore detailed Line Profile Analysis can extract information about defects and flaws within a material but only when other broadening effects are fully accounted for.

Diffraction is a phenomenon where a wave scatters coherently when it hits an obstacle or slit on the same order of magnitude as its own wavelength, resulting in regions of positive and negative interference. Crystalline solids possess periodic repeat distances of a number of angstroms so are capable of X-ray diffraction (wavelength 0.1 – 100 Å, scattered by electrons), electron diffraction (wavelength 200 - 1200 Å, scattered by charges and magnetic forces) and neutron diffraction (wavelength 1 Å, scattered by atomic nuclei and magnetic fields). As these techniques are sensitive to different parts within solid matter they often provide complementary information, but X-ray diffraction

is easier to perform (as it doesn't require a vacuum or a neutron source) and in many cases can singlehandedly solve a structure.

XRD always requires a crystalline solid but whether the material yields good crystals or a microcrystalline powder has a big impact on what techniques are suitable for structure determination. Single-crystal X-ray diffraction is the most widely used and the most informative technique for determining crystal structures[2-4] but it is limited to samples that produce single crystals of sufficient size and quality. In comparison powder X-ray diffraction (PXRD) is less widespread and less informative but remains effective on a wider range of samples so PXRD can be used on materials which are completely unsuitable for single crystal techniques.

PXRD is a technique to escape the sample restrictions of single crystal XRD, but sacrifices information in doing so. So structure determination by single crystal XRD is easier but if a material fails to give good crystals then single-crystal XRD simply cannot be performed. Structure determination by PXRD is comparatively harder, but you can fall back on PXRD when obtaining a suitable single crystal sample is impossible. In both cases the fundamental process is essentially the same, (i.e. X-rays of an appropriate wavelength are fired at the sample and diffraction occurs based on the periodic repeat distances within the sample), but the level of information that can be extracted is significantly different. Single crystal XRD patterns provide 3-dimensional 'reciprocal space' information, whilst PXRD patterns provide 1-dimensional compressed information. Data acquisition is typically faster with PXRD however.

To explain the difference between single crystal XRD and PXRD it is perhaps useful to examine the differences between the samples themselves. Single crystal XRD uses a large individual crystal in a single orientation, which gives rise to diffraction spots. Conversely a powder sample contains a multitude of randomly orientated small crystallites, so a powder examines all possible crystallite orientations simultaneously turning each diffraction spot into a cone. In effect this compresses the three dimensional diffraction pattern into a single dimension and results in a diffraction pattern of cones instead of spots (i.e. single crystal XRD and PXRD contain the same information on

repeat distances, but PXRD loses any information on dimensionality). This compression of information causes peak overlap on the PXRD pattern – all of this makes structure solution from powder more difficult than structure solution from single crystal. The distribution of crystallite orientations in a powder is random, but in some cases certain orientations may be preferred or disfavoured (e.g. if the shape of crystallites encourages them to stack together in a certain manner.)

In this thesis single-crystal XRD has been used to determine a number of new crystal structures, whilst PXRD has been used extensively as a 'fingerprinting' technique to confirm the identity of crystalline samples. Comparing the PXRD pattern of a newly prepared sample to the known patterns of the reagents and the desired product is a quick way to determine if crystallization has proceeded as planned and also to assess sample purity. Monochromatic molybdenum radiation has been used for single crystal XRD and monochromatic copper radiation has been used for PXRD.

Our method of structure determination PXRD[5, 6] first indexes the powder pattern to discern the space group and a plausible unit cell. Next the lineshape of the pattern is described using the Le Bail fitting method and the unit cell is confirmed. This unit cell is then populated with atoms according to chemical knowledge of the sample and trial structures are created. These trial structures are used to generate simulated powder patterns which are compared to the original acquired data. Molecule positions, bond angles and bond lengths are varied to produce many different powder patterns and genetic algorithms are used to generate successively better trial structures. These algorithms selectively retain the best structures and mix features between promising structures with the goal of creating better ones but also allow random changes to prevent stagnation. Creating hundreds of generations of trial structures is very processor intensive and quite time consuming. When a good structure is achieved refinement is used to fit the structure with the acquired powder pattern. Reciprocal space methods can also be used to solve PXRD structures which allows us to solve structures without additional chemical knowledge, but accuracy depends heavily on the structure factors extracted from the data so high resolution data may be necessary.

Structure determination from single crystal XRD proceeds by using specialized techniques to solve the phase problem (which arises because the acquired diffraction pattern has amplitudes but not relative phases). Such techniques include charge flipping, direct methods and electron density maps.

2.1.1 Theory of Diffraction

X-rays are scattered by the electrons in a sample and the vast majority of electrons are localized around atoms. Therefore a periodic repetition of atoms results in a periodic repetition of electrons which in turn will scatter X-rays at regular intervals. In most directions destructive interference cancels out the intensity of the diffracted X-rays but constructive interference occurs when X-rays are in phase with each other. This constructive interference occurs when the wavelength of the X-rays satisfies Bragg's Law (Equation 2.1) for a repeat distance within the material.[7]

$$n\lambda = 2d_{hkl}\sin\theta \tag{2.1}$$

Where n is a positive integer, λ is the wavelength of the incident X-rays, d_{hkl} is the lattice spacing for the planes described by Miller indices *hkl* and θ is the angle between the X-ray beam and the lattice plane. These parameters can be seen on Fig. 2.1 which shows constructive interference for X-rays reflected from parallel lattice planes. Note that the angle of reflection is the same as the angle of incidence and indeed certain comparisons can be made to the reflection of optical light by a mirror.
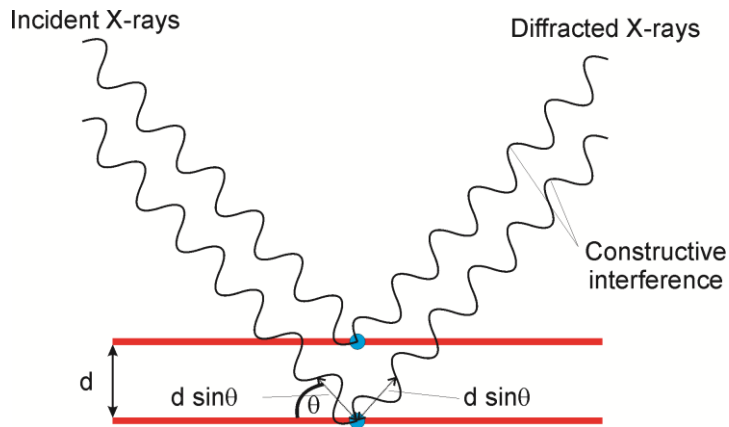
Fig. 2.1 *Figure illustrating the scattering of X-rays from parallel lattice planes.*

Constructive interference occurs when the path difference between the two X-rays is equal to an integer multiple of the X-ray wavelength and the Bragg equation describes the geometric conditions required to achieve this.

A Bragg reflection with the Miller indices *hkl* gives rise to a diffraction spot with intensity I_{hkl} proportional to the magnitude of the structure factor F_{hkl} squared (Equation 2.2). This structure factor describes the amplitude and phase of the reflection and it is generated by all the atomic scattering factors for all atoms within the unit cell.

$$I_{hkl} \propto |F_{hkl}|^2 \tag{2.1}$$

2.2 Birefringence

Birefringence is "double refraction" and occurs when light can be refracted differently depending on the relative orientation of the incident light and the refracting material. This phenomenon occurs in anisotropic materials where different axes possess appreciably different refractive indices.

Optical light birefringence is triggered by crystallographic anisotropy. No birefringence is possible in an isotropic material, but in a uniaxial material optical light may refract differently depending on whether its electric field vector is parallel or

perpendicular to the unique optical axis of the material. With non-polarized incident light the birefringence phenomenon causes a splitting effect - an ordinary ray (electric field vector perpendicular to material optical axis) and an extraordinary ray (electric field vector parallel to material optical axis) as evidenced in Fig. 2.2.
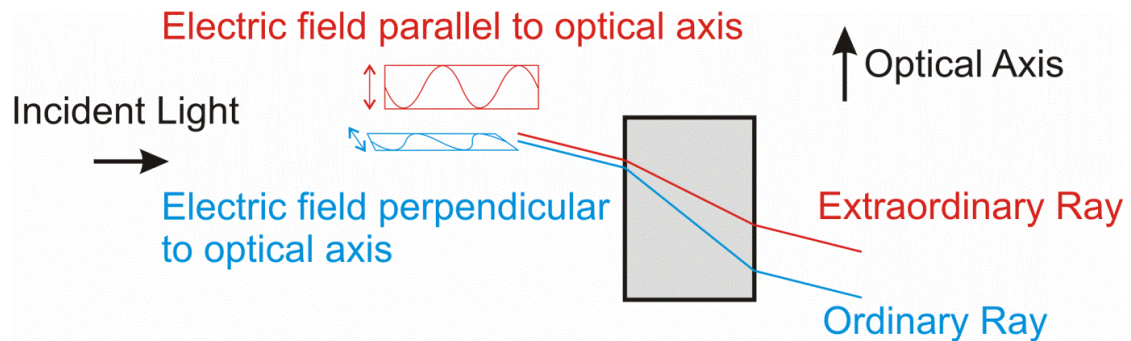
Fig. 2.2 *Schematic of a uniaxial material giving rise to birefringence.*

Birefringence also forms the basis of cross-polarized optical microscopy. Linearly polarized incident light will not pass through an analyser polarized at 90° to it, but a birefringent material orientated at 45° will split the incident light into ordinary and extraordinary components and components of these may pass through the analyser. Rotating the birefringent material away from 45° will result in a gradual decrease in transmitted intensity until the minimum is reached at 0° or 90°.

Birefringence is most easily understood in uniaxial materials but more complex phenomena are possible. Biaxial materials possess three different refractive indices and can give rise to more complicated refractive properties (occasionally called trirefringence). In these cases the fundamental process is the same but there are three different axes and three different refractive indices. Also it is important to note that whilst anisotropy is a prerequisite for birefringence the presence of anisotropy does not necessarily mean a material will exhibit significant birefringence, i.e. it is possible for uniaxial materials to exhibit negligible birefringence because the different axes have very similar refractive indices.

Optical birefringence is largely mentioned here as a gateway to X-ray birefringence but some polarizing optical microscopy experiments were carried out at ambient temperature using a Leica MZ12.5 stereomicroscope (Leica DFC 480 digital camera and Leica CLS 150X light source) with the polarizer and analyzer in crossed-polarizer configuration.

2.2.1 X-ray birefringence

X-ray birefringence shares many similarities with optical birefringence but the fundamental difference is that X-ray birefringence is triggered by the interaction of X-rays with core electrons[8-10] rather than the interaction of optical light with the entire crystal structure. This means the X-ray unique axis can be different from the optical axis and is not necessarily a crystallographic axis. The origin of X-ray birefringence also means that energy matching is critically important to the technique which in turn presents both advantages and disadvantages. X-ray birefringence can be tuned to the energies of specific elements in order to get information about specific bonds but conversely some energies may be harder to access or may suffer from greater absorption in the air.

X-Ray birefringence can be measured with a setup analogous to that of the polarizing microscope in optical microscopy, but uses more complex apparatus (Fig. 2.3). In this set up linearly polarized X-rays are fired at an analyser polarized in a different plane so that no signal is transmitted. However a birefringent sample at the right orientation can split the polarized X-rays into an ordinary and extraordinary component and a component of these can satisfy the cross-polarized analyser.

The need for highly polarized X-rays means X-ray birefringence experiments are much more suitable for synchrotron sources than lab sources and thus far all our experiments have been performed on beamlines B16 and I16 at the Diamond Light Source synchrotron.
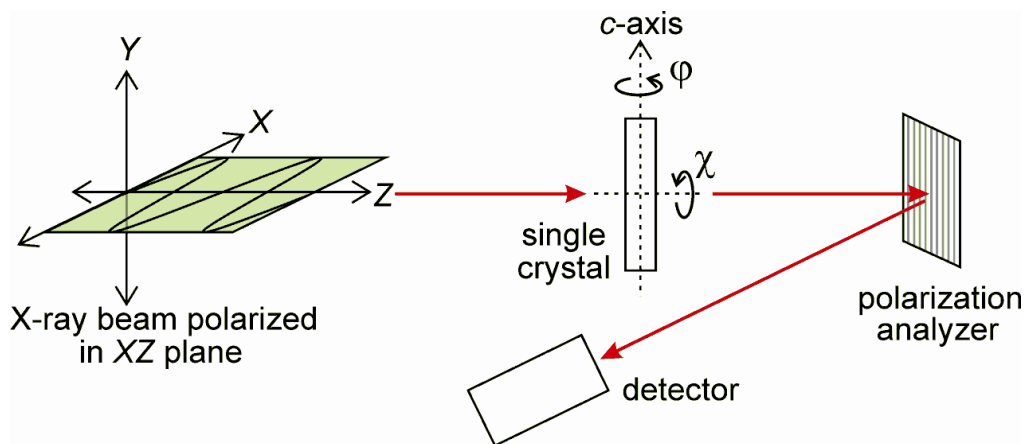
Fig. 2.3 *Experimental setup of the X-ray birefringence focused beam experiments.*

If the X-ray axis is aligned with the optical axis then the material will exhibit the same birefringence properties with optical light and X-rays, but if the two axes are different then significantly different properties may be observed. An example of the former is the 1-bromoadamantane/thiourea inclusion compound which shows almost ideal uniaxial X-ray birefringence (Fig. 2.4) and optical birefringence as all its C-Br bonds are aligned with each other along the unique c-axis[8]. As the X-ray unique axis and the optical axis are the same the same information is obtained from X-ray birefringence and polarizing optical microscopy.
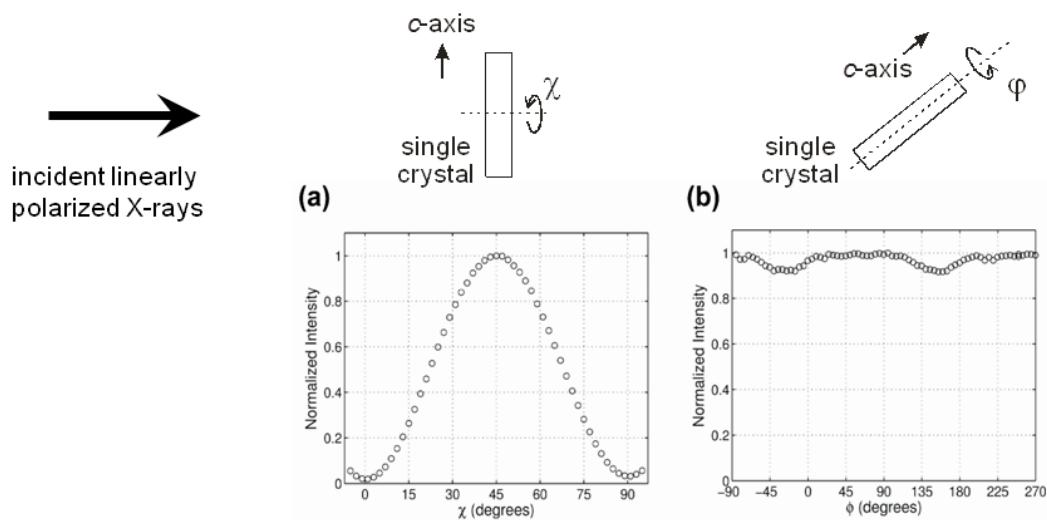
Fig. 2.4 *Transmitted X-ray intensity of a single crystal of 1-bromoadamantane/thiourea a) as a function of χ, with φ fixed and b) measured as a function of φ, with χ fixed at 45°.*

X-ray birefringence experiments on the bromocyclohexane/thiourea inclusion compound are perhaps a more interesting result as in this case the technique yields different results compared to polarizing optical microscopy. Polarizing optical microscopy of the bromocyclohexane/thiourea shows birefringence with the c-axis (the direction of the thiourea tunnel) in both the high temperature and low temperature phases. However in the high temperature phase the C-Br bonds are isotropically disordered and no X-ray birefringence is observed, in the low temperature phase there is local ordering of the C-Br bonds and X-ray birefringence is observed on an axis 52.5° from the crystallographic *c*-axis[11] . This demonstrates X-ray birefringence's specificity to certain bonds and in fact the C-Br bond angle determined by X-ray birefringent measurements shows good agreement with the value known XRD structure determination (52.5° vs 53.7°).

X-ray birefringence requires overall anisotropy of electron density and the technique is insensitive to a number of materials including: 3-dimensionally ordered centrosymmetric materials, isotropically disordered materials and ionic materials where the selected element exists as a spherical free ion. In each of these cases there can be no X-ray unique axis so X-ray birefringence cannot occur.

As X-ray birefringence arises from the difference between parallel and perpendicular interactions X-ray birefringence is only sensitive to the orientation of a bond, and not the direction (i.e. a material with all the relevant bonds in one direction is indistinguishable from a material where the relevant bonds are all aligned but alternate between parallel and anti-parallel directions)

Thus far the technique has been used on crystalline solids where the structure was already determined by XRD but one can imagine applications in investigating locally ordered but non-crystalline materials such as liquid crystals and glasses where XRD would be ineffective.

2.2.2 X-ray Birefringence Imaging

X-ray Birefringence Imaging (XBI) is a new technique pioneered in conjunction with Diamond Light Source and utilizing their B16 beamline. Schematically it bears many similarities to the focussed beam X-ray birefringence technique with a simple switch to wide slits and an area detector (Fig. 2.5). However it yield significantly different results and is subject to different challenges.
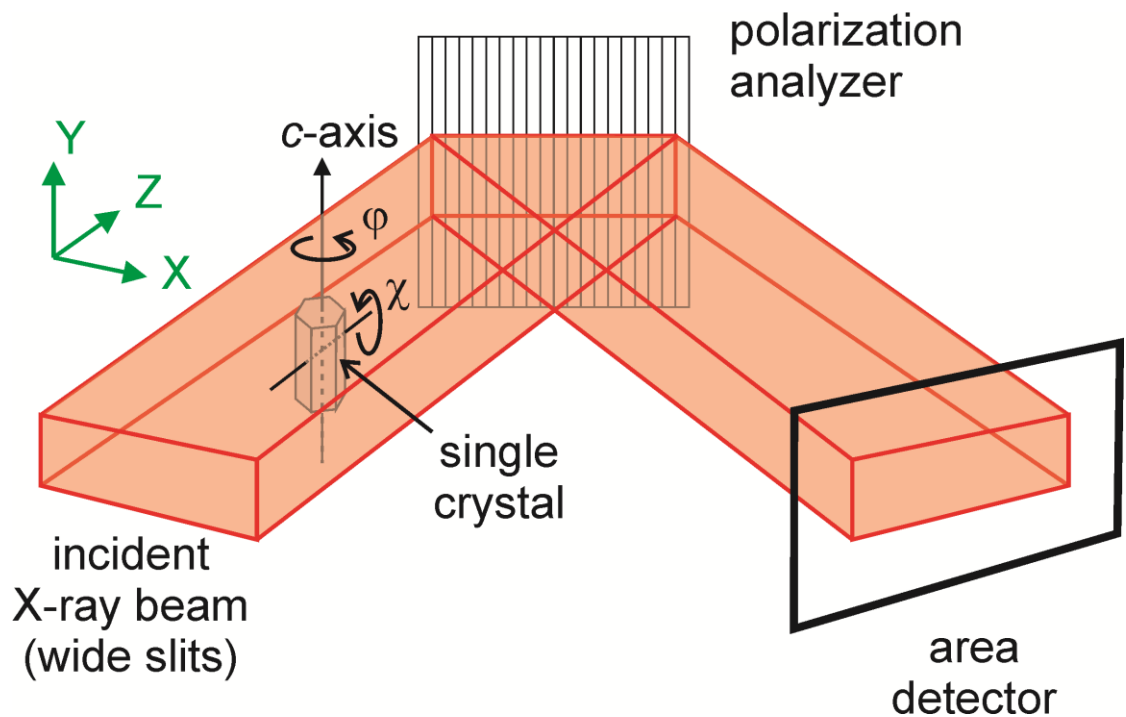
Fig. 2.5 *Experimental setup of the X-ray birefringence imaging experiments. A wide beam and an area detector are used to image the entire crystal.*

XBI experiments use a large-area linearly-polarized X-ray beam [with dimensions 0.8 mm (vertical) × 4.0 mm (horizontal)] incident on the sample. The intensity of the wide X-ray beam emerging from the polarization analyzer is recorded using an area detector, mapping the XB of the material in a spatially resolved manner, with resolution of the order of 10 μm. This setup observes the entire crystal in one measurement which makes it easy to identify regions with different behaviour.

XBI requires a linearly polarized X-ray beam which matches the energy of core electrons of the target atom. In these experiments we have used the B16 beamline at the Diamond Light Source synchrotron to attain an X-ray beam with greater than 95% linear polarization in the horizontal plane and performed experiments at 13.493 keV. This energy corresponds to the midpoint of the Br K-edge, giving it sensitivity to the orientation of bromine bonds. Various exposure times have been experimented with, typically on the order of a few seconds (data reported in Chap 3 had a 1 second acquisition time, data reported in Chap 4 had a 4 second acquisition time).

In our work X-ray intensity has been measured using the B16 "X-ray eye" detector CCD miniFDI camera from Photonic Science Ltd area detector, but other devices were tested during preliminary work. The spatial resolution of the XB images in the vertical direction (*ca*. 13 μm) is limited by the resolution of the CCD-based detector and the spatial resolution in the horizontal direction is limited by the penetration of the beam into the polarization analyzer. In Chapter 3 the XBI experiments utilize the Si(555) reflection which gives a spatial resolution of *ca*. 28 μm but in Chapter 4 the XBI experiments utilize the Ge(555) reflection which gives a spatial resolution of *ca*. 11 μm.

Experiments with the two different analysers give significantly different background profiles and in both cases a rotation has been applied to correct a tilt observed in the beam (which we know must be horizontal). This tilt arises due to differences in the horizontal and vertical scattering angles but it is interesting to note that images produced using the Si(555) analyser show a beam 8° anticlockwise away from horizontal whilst the Ge(555) images show a beam 8° clockwise from the horizontal.

In the case of Bragg diffraction by a perfect analyzer crystal, the background signal (i.e. the X-ray intensity that would be detected with no sample present) in the crossed-polarizer configuration scales with $|\cos(2\theta)|$ in the case of dynamical diffraction and scales with $\cos^2(2\theta)$ in the case of kinematical diffraction, where 2θ is the diffraction angle of the analyzer crystal. In the ideal case, $2\theta = 90°$ and the background intensity would be zero (giving a black background in the XB images). In practice, it is necessary to find a good match of the incident X-ray beam energy ($E = 13.493$ keV; $\lambda = 0.9188$ Å)

to a Bragg reflection of an analyzer crystal that gives a diffraction angle as close as possible to $2\theta = 90°$. In Chapter 3, we employed the Si(555) reflection with $2\theta = 94.2°$, and hence $|\cos(2\theta)| = 0.073$ and $\cos^2(2\theta) = 0.005$. Thus, depending on the relative contributions of dynamical and kinematical diffraction, between *ca.* 0.5% and 8% of the incident X-ray intensity is transmitted by the analyzer. In Chapter 4, we employed the Ge(555) reflection with $2\theta = 89.4°$, and hence $|\cos(2\theta)| = 0.010$ and $\cos^2(2\theta) = 0.0001$. Thus, depending on the relative contributions of dynamical and kinematical diffraction, between *ca.* 0.01% and 1% of the incident X-ray intensity is transmitted by the analyzer. For this reason, the background in both sets of images does not correspond to exactly zero intensity.

Note that the use of X-rays theoretically enables a better resolution limit than optical light due to the shorter wavelength, but with our current apparatus we have only achieved a resolution on the order of 10 μm. The most immediate way to improve this value is with better X-ray detectors and higher quality analyser crystals, and these changes could conceivably give a resolution of approximately 1 μm but still this is not competitive with optimized optical microscopy and electron microscopy. It is difficult to predict what is practical and feasible with XBI as it is a new technique with much scope for improvement, but still it seems unlikely that XBI would supersede the established imaging techniques.

As our XBI data is acquired digitally on a per pixel basis it is possible to extract numerical intensity values from the images for specific regions of the crystal. Therefore the information obtained in a focussed beam X-ray birefringence experiment can be extracted from XBI images, with two notable differences. Firstly XBI measures the entire crystal, so intensity can be extracted from multiple regions within the crystal rather than just one. Secondly focussed beam experiments can use mirrors to produce a more intense incident beam and obtain higher quality data.

2.3 Solid-State Nuclear Magnetic Resonance Spectroscopy

Much like solution NMR solid-state NMR involves using radio waves to 'flip' the state of spin-active nuclei inside an applied magnetic field, then allowing these nuclei relax to their ground state and measuring the energy emitted. However solid-state NMR is much less routine than solution NMR as it requires more complicated apparatus and the data can be more difficult to interpret.

Solid-State NMR can provide detailed information on the number of chemical environments within a sample but it brings a number of challenges and difficulties. In solution the rapid random tumbling of molecules simplifies spectra because it reduces some interactions to isotropic values and eliminates the orientational dependency on the external field and averages out the macroscopic chemical shielding of the external magnetic field. The same movement does occur in the solid state but it is much slower and the longer timescale makes it less effective. This means solid samples experience less change in positional and magnetic environment, so have less time-averaged character and can give much broader peaks (Fig. 2.6).
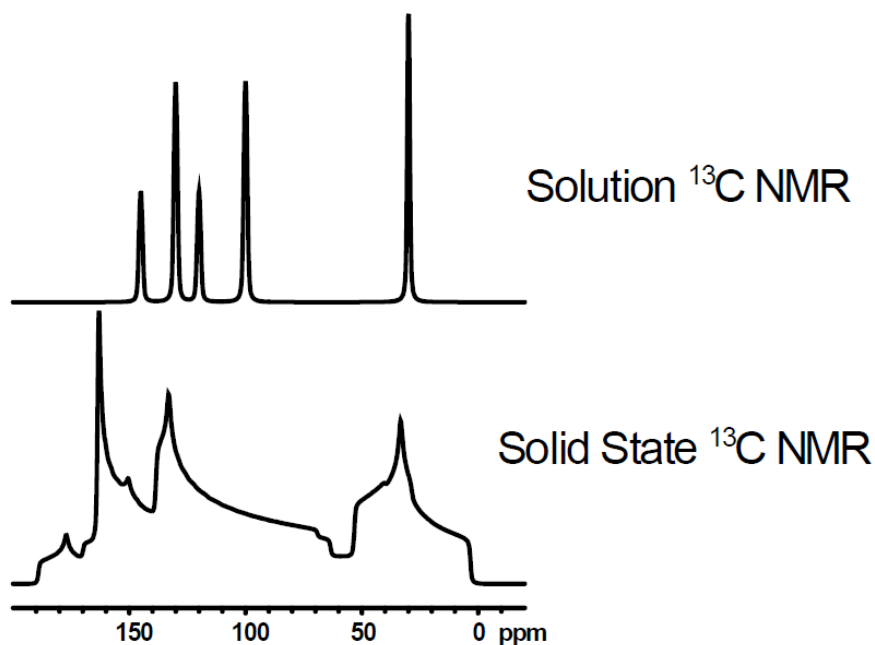
Fig. 2.6 *Illustration of the broader line shapes observed in solid state NMR for the same molecule.*

Comparing solution-state NMR and solid-state NMR highlights how solid-state NMR can be subject to several additional factors:

- Different molecule orientations give different responses. A molecule aligned parallel to the external field will give different signal than one orientated perpendicular to the field. Therefore different crystal orientations will give different spectra and a powdered sample gives information on all possible orientations.

- Different macroscopic locations give different responses. As the applied field penetrates through the sample it is increasingly masked by induced local fields. Hence molecules on the far side of the sample are subject to greater shielding than molecules on the near side.

- Dipole-dipole interactions and the 1st order component of quadrupolar interactions cause additional broadening effects cause broadening in solid state NMR but these factors are averaged to zero in solution.

There are a number of strategies that can be used to simplify or intensify solid state NMR spectra and obtain more meaningful information. Of the many available techniques the only ones utilised in this thesis were Magic Angle Spinning, Cross-Polarisation and Direct Excitation.

Magic Angle Spinning (MAS) is a technique designed to mimic the rapid random tumbling of molecules in liquids[12] By rapidly spinning a sample at an angle of 54.74° to the applied field (see Fig. 2.7) it is possible to average out the effect of the external field as well as average dipolar interactions and the 1st order component of quadrupolar interactions to isotropic values. Often the spinning is not fast enough to give a single peak and instead results in a series of spinning side-band peaks, spaced at integer multiples of the spinning rate away from the isotropic peak. In preliminary work on our 300 MHz spectrometer our guest/urea inclusion compounds were spun at 6 kHz and noticed sidebands on the urea peak. The urea peak 164ppm produced a sideband at 84.5ppm and occasional hints of a second sideband at 5ppm. Note that the centreband is not necessarily

the most intense peak but it is always easy to identify because it does not move with different spinning frequencies. For our work at the 850 MHz spectrometer at the UK National High-Field Solid-State NMR Facility we typically used a spinning speed of 12 kHz and no spinning side bands were observed.
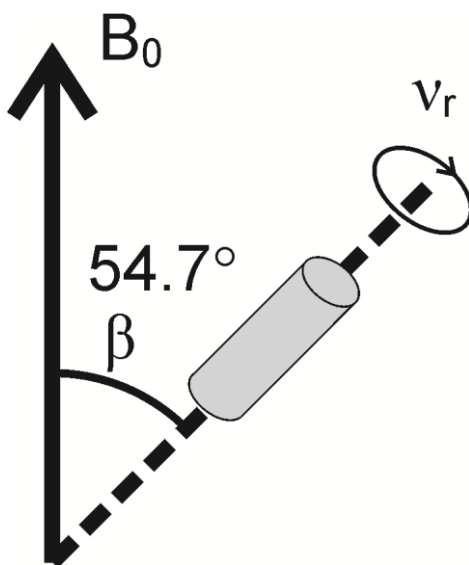
Fig. 2.7 *Schematic of magic angle spinning. B_0 is the applied field, β is the spinning angle of 54.7° and v_r is the rotational velocity.*

Cross-Polarisation (CP) is a signal enhancement technique that uses abundant spins (I) to enhance the signal from dilute spins (S) [12,13]. A typical example is using ^{1}H nuclei (99.985% abundance) to increase the signal from ^{13}C nuclei (1.1% abundance). The fast spin-lattice relaxation of ^{1}H allows the CP operation to be repeated rapidly to accumulate signal which is then transferred to ^{13}C. Note that cross-polarisation varies in efficiency with different positions and different molecules so it cannot be interpreted quantitatively. CP is extremely common in SS NMR but the inclusion compounds investigated in this thesis gave good signal on proton decoupled ^{13}C direct excitation (HPDEC) so CP was only used sparingly. We attribute the surprising efficiency of Direct Excitation to high guest mobility within the urea tunnel which results in faster relaxation. Halogen nuclei can also be used for SS NMR experiments[14] but this experiment focuses on ^{13}C as both ^{79}Br and ^{81}Br are quadrupolar and give broad signals.

2.3.1 In-Situ Solid-State NMR

In-situ experiments are techniques designed to monitor a process as it occurs, rather than merely examining the reactants (*ab initio*) or the products (*ex situ*), and our *in-situ* NMR strategy examines a sample during the crystallization. Acquiring information during the evolution of the crystallization process is particularly advantageous as it can inform us of intermediate states, changes in concentration and lag times all of which would not be evident in *ex situ* techniques (which only give information on the starting point or the end point, they cannot follow a process as it occurs).

In-situ NMR is performed by cooling an undersaturated solution from high temperature to low temperature inside the NMR rotor so that the solution becomes supersaturated (Fig. 2.8). At this lower temperature crystallization is thermodynamically favoured, and the time-dependence of the crystallization process is monitored by repeatedly recording high-resolution NMR spectra as a function of time. In order to follow a process accurately we require good time-resolution and the time-resolution of *in-situ* NMR depends crucially on the time taken to record an individual NMR spectrum of sufficient quality. We need good enough data to identify different phases, distinguish different forms and monitor changes, but we also need to acquire the data quickly enough to track the crystallization process. Sensitivity to small amounts of sample is also advantageous as it grants us information on earlier stages of the crystallization process. With all this in mind it follows that *in-situ* NMR techniques require a great deal of optimization in order to gather good data in the shortest possible time. One such way to minimize acquisition time is through the use of high field spectrometers and indeed our *in-situ* NMR work has been carried out at the UK National High-Field (850 MHz) Solid-State NMR Facility for precisely this reason. Isotopic labelling is also effective at boosting signal and cutting acquisition time, but is not always practical and has not been employed in this work. Do note that *in-situ* NMR is performed on a standard solid-state NMR machine, but it requires well-sealed NMR rotors to prevent sample leaks.
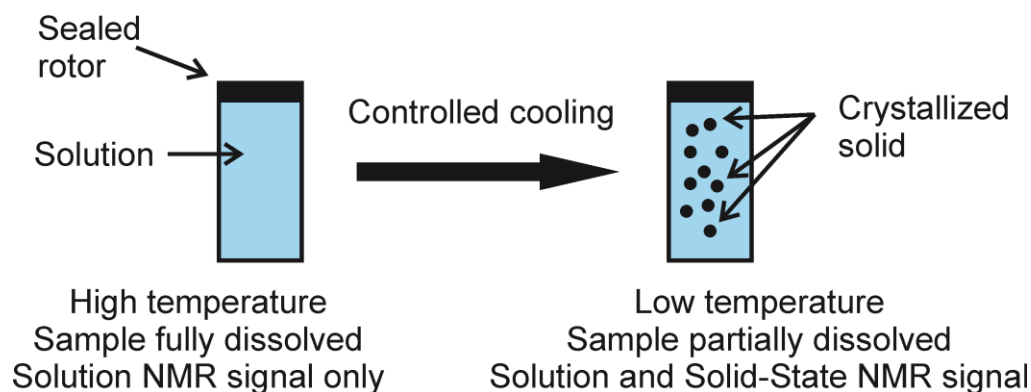
Fig. 2.8 *Schematic of the in-situ NMR crystallization process.*

Another key advantage to *in-situ* NMR is the ability to selectively detect only the solid within the sample, ignoring contributions from both the solvent and solute. Depending on what pulse sequences we use we can examine the solution inside the rotor or we can choose to specifically examine the crystallized solid or alternating between the two[15] (Fig. 2.9). For an organic material recording ^{13}C spectra under $^{1}H{\rightarrow}^{13}C$ cross polarization conditions allows us to gather signal exclusively from the solid phase[16, 17] with this selectivity arising due to different dynamic behaviours of molecules in the solid and solution state. Therefore even if only a small fraction of the solute has crystallized (as may be the case in the early stages of the crystallization experiment), it is only these solid particles that contribute to the measured NMR spectrum. The dissolved solute molecules may be present in much greater amount in the early stages of crystallization but are "invisible" to the measurement.

Conversely *in-situ* crystallization studies using X-ray or neutron techniques are sensitive to both the crystallized solid and the solution. As a result scattering from the solution phase may dominate the data, particularly when there is only weak scattering from the solid (if the crystallization process is in its infancy or if little solid is crystallized). Additionally SS NMR examines the full material within the NMR rotor (an entire crystallization system, albeit on a small scale) whilst most *in-situ* X-ray

and neutron experiments use a finely focused beam that only probes a small part of the sample.
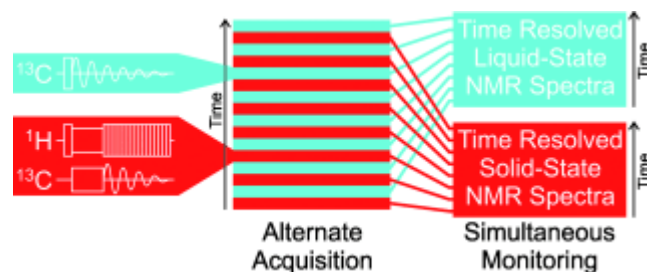
Fig. 2.9 *Schematic of the CLASSIC in-situ NMR experiment.*

Note that *in-situ* NMR requires A) a solute/solvent combination that exhibits a noticeable difference in solubility across the temperature range available to the NMR spectrometer and B) a sample at the right concentration to properly exploit this temperature dependency. If these conditions are met then the NMR sample is completely solvated at high temperatures but as the sample is cooled the solution becomes supersaturated and solid material crystallizes out of solution. If these conditions aren't achieved then the solid might not dissolve completely at high temperature (so representative of a seeded crystallization process not a spontaneous one) or very little solid material will crystallize out at low temperature (resulting in little solid signal). For this reason detailed solubility measurements usually precede *in-situ* NMR.

2.4 References

[1]   L. Smart, E. Moore, *Solid State Chemistry, an Introduction*, Second Edition, **1995**, Chapman & Hall, London.

[2]   J. P. Glusker, K. N. Trueblood, *Crystal Structure Analysis – A Primer*, **1985**, Oxford University Press, Oxford.

[3]   J. D. Dunitz, *X-Ray Analysis and the Structures of Organic Molecules*, **1995**, Verlag Helvetica Chimica Acta, Basel.

[4]   G. M. Sheldrick, *Acta Crystallogr.* **2008**, Sect. A64, 112.

[5]   K. D. M. Harris, *Mater. Manuf. Processes*, **2009**, *24*, 293

[6]   K. D. M. Harris, *Top. Curr. Chem.*, **2012**, *315*, 133.

[7]   W. L. Bragg, *Proc. R. Soc. London, Ser. A,* **1913**, *89*, 248-277

[8]   B. A. Palmer, A. Morte-Ródenas, B. M. Kariuki, K. D. M. Harris, S. P. Collins, *J. Phys. Chem. Lett.*, **2011**, 2, 2346-2351.

[9]   S. P. Collins, D. Laundy, K. D. M. Harris, B. M. Kariuki, C. L. Bauer, S. D. Brown, P. Thompson, *J. Phys.-Condens. Mat.*, **2002**, 14, 123-134.

[10]   C. Brouder, *J. Phys.-Condens. Mat.*, **1990**, 2, 701-738.

[11]   B. A. Palmer, B. M. Kariuki, A. Morte-Ródenas, K. D. M. Harris, *Cryst. Growth Des.* **2012**, 12, 577-582.

[12]   D. L. Bryce, G. M Bernard, M. Gee, M. D. Lumsden, K Eichele, R. E. Wasylishen, *Can. J. Anal. Sci. Spect.* **2001**, 46, 46-82.

[13]   W. Kolodziejski, A. Corma, K Wozniak, J. Klinowski, *J. Phys. Chem.* **1996**, 100, 7345-7351.

[14]   R. P. Chapman, C. M. Widdifield, D. L.Bryce, *Prog. Nucl. Mag. Res. Sp.* **2009**, 215-237.

[15]   C. E. Hughes, P. A. Williams, K. D. M. Harris, *Angew Chemie Int Ed.* **2014**, 53(34), 8939-43.

[16]   R. K. Harris, *Analyst*, **2006**,131, 351-373.

[17]   M. J. Duer, *Introduction to Solid-State NMR Spectroscopy*, **2004**, Blackwell Publishing Ltd., Oxford.

Chapter 3 – X-ray Birefringence Imaging on Brominated Thiourea Materials

3.1 Introduction

During our focused beam X-ray birefringence experiments[1-4] on the bromocyclohexane/thiourea inclusion compound, we were able to construct surface plots of intensity with φ and at χ various temperatures (Fig. 3.1) and structural modelling of this data allowed us to elucidate the orientation of the C-Br bond (Fig. 3.2) in good agreement with X-ray diffraction data. However the bromocyclohexane/thiourea inclusion compound lent itself to a strange observation – at some positions on the crystal we saw noticeably weaker or even negligible birefringent signal, even when scanning wide ranges of φ and χ. This phenomenon could be explained by the remaining guest disorder at low temperatures but, nonetheless, we endeavoured to investigate further, with a technique that would enable spatially resolved mapping of the material.
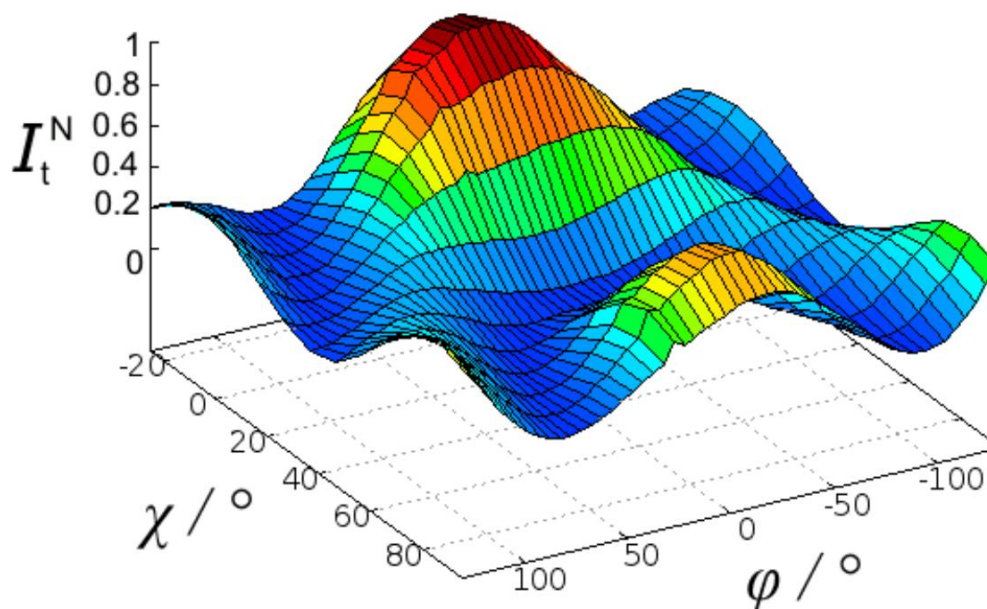
Fig. 3.1 *Surface plot of intensity vs φ and χ for the bromocyclohexane/thiourea inclusion compound at 100 K. Structural modelling of these surface plots yields information on the orientation of the C-Br bond.*
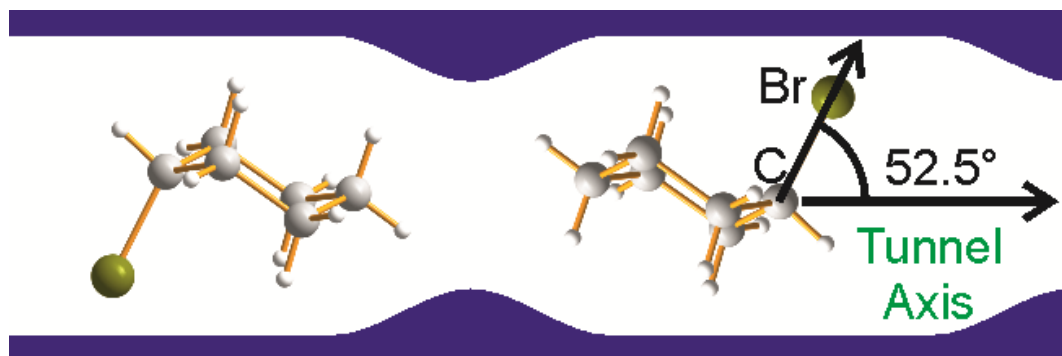
Fig. 3.2 *Graphic of the C-Br bond of bromocyclohexane inside the thiourea tunnel. The 52.5° angle has been determined from XRD data, which is remarkably close to the 53.7° angle we obtained from our model.*

We designed an experimental set-up (Fig. 3.3) that allows XB measurements to be carried out in imaging mode, using a large-area linearly-polarized X-ray beam [with dimensions 0.8 mm (vertical) × 4.0 mm (horizontal)] incident on the sample[5] The intensity of the wide X-ray beam emerging from the polarization analyzer is recorded using an area detector, mapping the XB of the material in a spatially resolved manner, with resolution of the order of 10 μm.

The spatial resolution of the XB images in the vertical direction (*ca*. 13 μm) is limited by the resolution of the CCD-based detector and the spatial resolution in the horizontal direction (*ca*. 28 μm) is limited by the penetration of the beam into the polarization analyzer [Si(555) reflection]. The latter could be reduced to less than 1 μm by using high-quality crystals of heavier elements. In the reported work the time to record each XB image was 1 s, but in preliminary experiments various exposure times were employed.
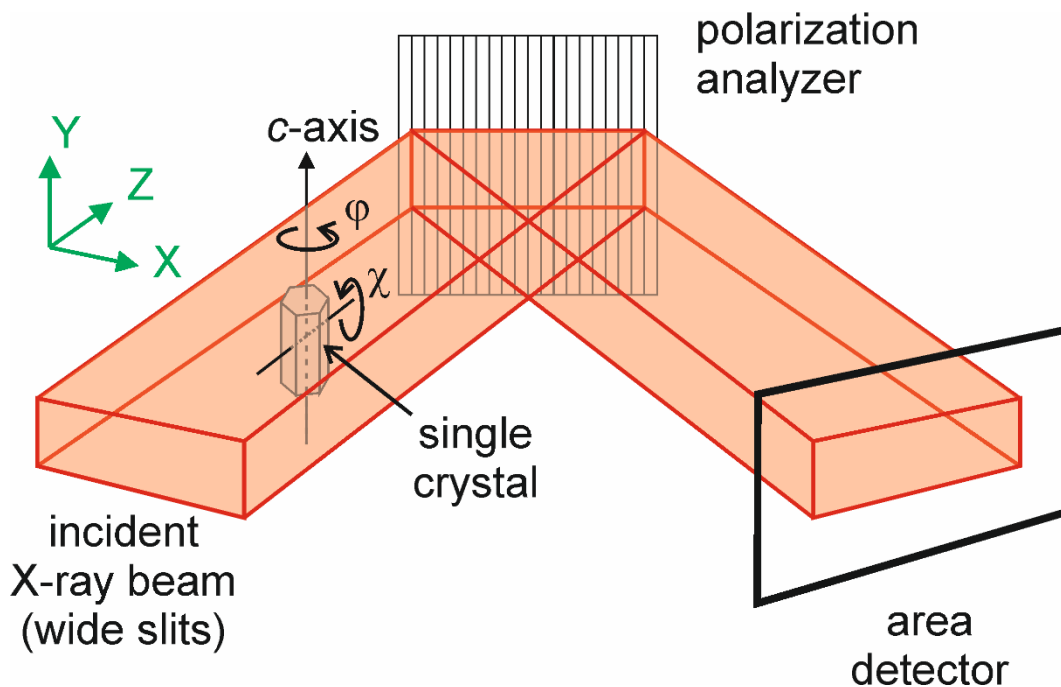
Fig. 3.3 *Experimental set-up for XBI. The incident X-ray beam propagates along the z-axis and is linearly polarized along the x-axis. The tunnel axis (c-axis; long-needle axis of crystal morphology) of the crystal was maintained in the plane (xy-plane) perpendicular to the incident X-ray propagation direction (z-axis). The crystal orientation was altered by variation of angles χ and φ, where χ refers to rotation of the c-axis of the crystal around the laboratory z-axis and φ refers to rotation of the crystal around its c-axis.*

This X-ray Birefringence Imaging (XBI) technique is analogous to the polarizing optical microscope and in order to gauge the potential of XBI it is useful to look at the achievements of polarizing optical microscopy. Since its invention in the 19th century the polarizing optical microscope has found numerous applications in mineralogy[6], crystallography[7, 8], materials science[9, 10] and biology[11, 12] to investigate the structural properties of birefringent materials. From liquid crystals[13] to collagen fibres in tendons[14] and cartilage[15], and from amyloid plaques[16] to butterfly wings[17] and spider silk[18], the polarizing optical microscope has been used to establish the relationship between the structural anisotropy of materials and their function. In the phenomenon of birefringence, the refractive index of an anisotropic material depends on the orientation of the material with respect to the direction of linearly polarized incident radiation. When such a material is viewed in a polarizing optical microscope in crossed-polarizer configuration, the intensity of light transmitted through the polarization analyzer depends

on the orientation of the optic axis/axes relative to the direction of polarization of the incident light. By measuring the intensity of transmitted light as a function of the orientation of the material, information on the orientation of the optic axis/axes can be established. Furthermore, if the material comprises orientationally distinct domains, the spatial distribution and orientational relationships between the domains may be revealed.

XBI is a new technique so its true applications have yet to be determined but still our results demonstrate the utility and potential of XBI as a sensitive technique for imaging the local orientational properties of anisotropic materials, including characterization of changes in molecular orientational ordering associated with solid-state phase transitions and identification of the size, spatial distribution and temperature dependence of domain structures[19].

Although X-ray and optical birefringence share several common characteristics, optical birefringence relates to the anisotropy of the material as a whole (e.g. for a crystalline material, it depends on the overall symmetry of the crystal structure), whereas X-ray birefringence (XB), when studied at an X-ray energy close to the absorption edge of a specific type of atom in the material, depends on the local anisotropy in the vicinity of the selected type of atom. Thus, XB depends on the orientational properties of the bonding environment of the X-ray absorbing atom. As a consequence, the "optic axis" in the case of XB is not necessarily related to a crystallographic optic axis, and measurement of XB has the potential to yield structural information on the local orientational properties of individual molecules and/or bonds For molecular solids, XB depends on the orientational properties of the molecule containing the X-ray absorbing atom, and in particular depends on the bonding environment of this atom in the molecule. Here we focus on XB studies at the Br K-edge for materials containing brominated organic molecules. In this case, XB behaviour can be rationalized simply on the basis of the orientational properties of the C–Br bonds[1, 2].

3.2 Experimental

Crystals of the 1-bromoadamantane/thiourea and bromocyclohexane/thiourea inclusion compounds were prepared by cooling solutions of thiourea and 1-bromoadamantane or bromocyclohexane (*ca*. 3:1 molar ratio of thiourea:guest) in methanol from 55 to 20 °C over *ca*. 29 h. The crystals were needle-shaped, with the needle axis corresponding to the tunnel axis of the thiourea host structure (*c*-axis). In each case, powder X-ray diffraction confirmed that the product was a monophasic sample of the thiourea inclusion compound.

All X-ray birefringence imaging experiments reported here were carried out on beamline B16 at the Diamond Light Source[20] employing a five-circle, vertical-scattering, Huber eulerian diffractometer. On beamline B16, the incident X-ray beam is greater than 95% linearly polarized in the horizontal plane. All measurements were carried out with an incident X-ray energy of 13.493 keV, which corresponds to the midpoint of the Br K-edge and the position of maximum birefringence (Figs 3.4 & 3.5 show how the position of maximum birefringence relates to X-ray adsorption) [2]. The Br K-edge was established from X-ray absorption spectra of BrCH/thiourea recorded in the high-temperature phase, for which the Br K-edge X-ray absorption spectrum is essentially independent of crystal orientation as a consequence of the isotropic orientational disorder of the BrCH guest molecules in the high-temperature phase. For temperature control, a cryogen-free helium gas-jet cooler (supplied by Cryoindustries of America; base temperature *ca*. 18 K) was used.
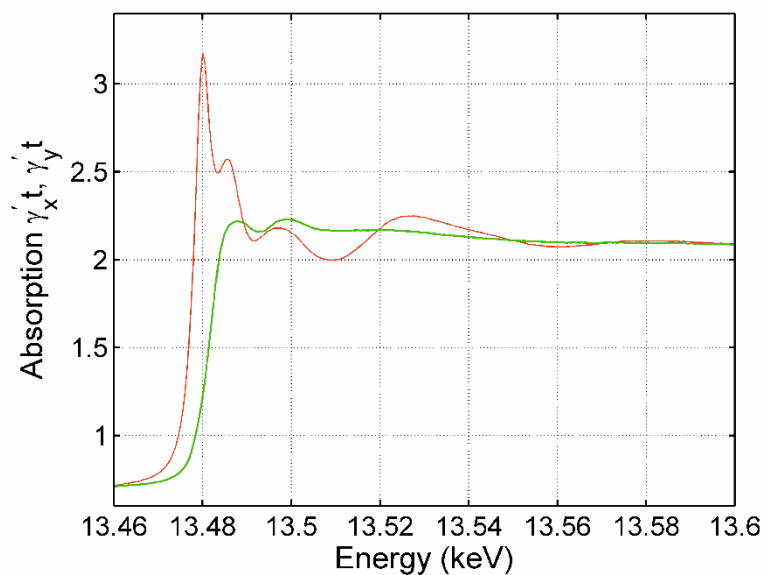
Fig 3.4 *X-ray absorption spectra measured with the c axis of a single crystal of 1-BA/thiourea parallel (red line) and perpendicular (green line) to the plane of polarization of the incident X-ray beam.*
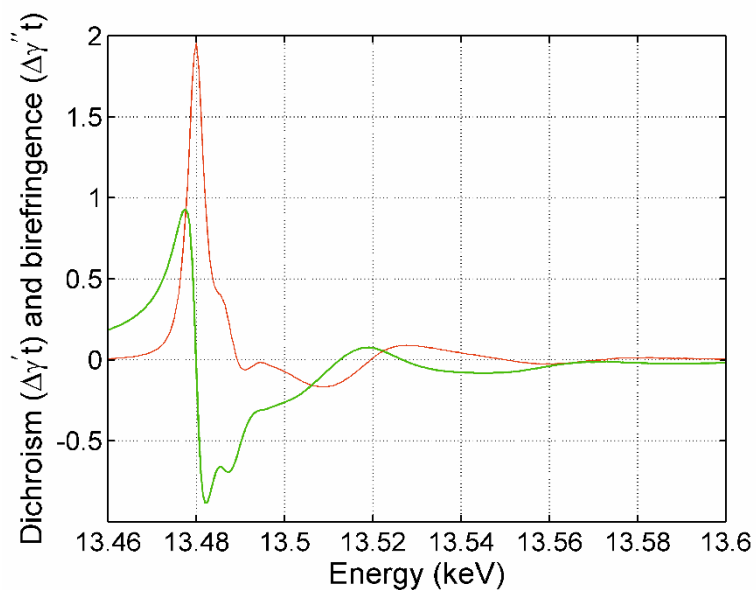
Fig 3.5 *Measured X-ray dichroism spectrum (red line, the difference between the two curves in Fig 3.4) and the calculated X-ray birefringence spectrum (green line). Exact energy values used in this section differ slightly from this figure due to slightly different energy calibration on the beamline but the same technique was used to find the position of maximum X-ray birefringence.*

In our experimental set-up for XBI (see Fig. 3.3), the transmission of linearly polarized X-rays through a single crystal of 1-BA/thiourea or BrCH/thiourea was studied in the "crossed-polarizer" geometry. As shown in Fig. 3.3, the tunnel axis of the crystal of the thiourea inclusion compound was maintained in the plane (*xy*-plane) perpendicular to the direction of propagation of the incident beam (*z*-axis), with the incident X-ray beam linearly polarized along the *x*-axis (horizontal). The crystal orientation was varied by rotation about the angles χ and φ defined in Fig. 3.3, where χ refers to rotation of the *c*-axis of the crystal around the laboratory *z*-axis and φ refers to rotation of the crystal around its *c*-axis. The dimensions of the crystals were *ca*. 3 mm along the tunnel axis of the thiourea host structure and *ca*. 0.5 mm perpendicular to this axis. To carry out XBI measurements, a large unfocused incident beam [0.8 mm (vertical) × 4.0 mm (horizontal)] was used, and a spatially resolved map of the transmitted X-ray intensity for the crystal was measured using an area detector (specifically, the B16 "X-ray eye" detector, CCD miniFDI camera from Photonic Science Ltd). The spatial resolution of the XB images in the vertical direction (*ca*. 13 μm) is limited by the resolution of the CCD-based detector and the spatial resolution in the horizontal direction (*ca*. 28 μm) is limited by the penetration of the beam into the polarization analyzer [Si(555) reflection] (the latter could be reduced to less than 1 μm by using high-quality crystals of heavier elements). With this experimental set-up, the exposure time to record each XB image was 1 s. Other area detectors and exposure times of up to 3 s were used in preliminary work before we settled on this setup.

In the case of Bragg diffraction by a perfect analyzer crystal, the background signal (i.e. the X-ray intensity that would be detected with no sample present) in the crossed-polarizer configuration scales with $|\cos(2\theta)|$ in the case of dynamical diffraction and scales with $\cos^2(2\theta)$ in the case of kinematical diffraction, where 2θ is the diffraction angle of the analyzer crystal. In the ideal case, $2\theta = 90°$ and the background intensity would be zero (giving a black background in the XB images). In practice, it is necessary to find a good match of the incident X-ray beam energy (E = 13.493 keV; λ = 0.9188 Å) to a Bragg reflection of an analyzer crystal that gives a diffraction angle as close as possible to $2\theta = 90°$. In the present work, we employed the Si(555) reflection with $2\theta =$

94.2°, and hence $|\cos(2\theta)| = 0.073$ and $\cos^2(2\theta) = 0.005$. Thus, depending on the relative contributions of dynamical and kinematical diffraction, between *ca*. 0.5% and 8% of the incident X-ray intensity is transmitted by the analyzer. For this reason, the background in our images does not correspond to exactly zero intensity.

The displayed images were produced using a monochrome colour scheme with an intensity range of 2600 counts to 6000 counts (Fig. 3.10), anything below this range appears as pure black and anything above this range appears as pure white. This range was selected to provide maximum contrast within the region of the beam and produce the most meaningful images. Alternative intensity ranges for the same dataset are shown in Figs 3.6, 3.7, 3.8 to justify our selected intensity range and show no information is being lost. Artificial colour schemes were also experimented with but did little to improve the clarity of the images (see Fig. 3.9).
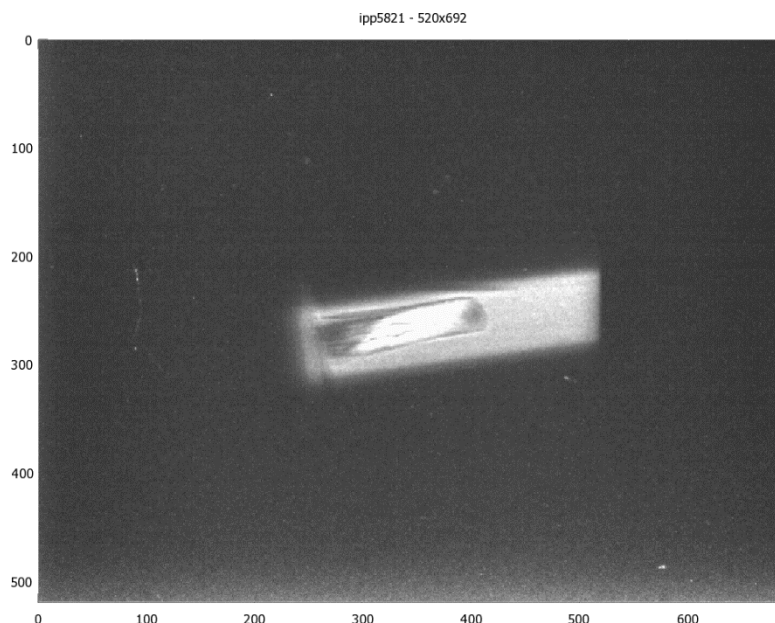
Fig. 3.6 *Raw imaging data (520 pixels by 692 pixels) of a single crystal of BrCH/thiourea at χ = 10°, φ = 0°, T = 20 K with an intensity range of 1250 - 4800.*
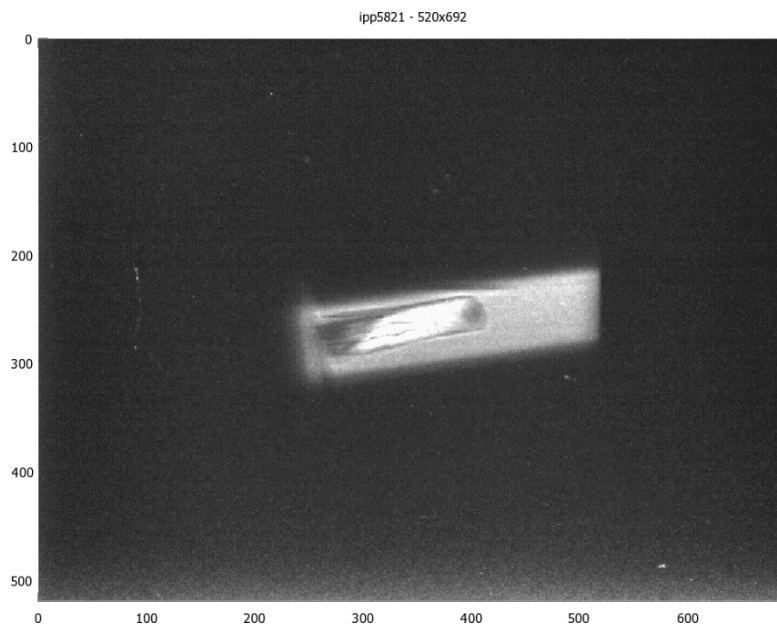
Fig. 3.7 *Raw imaging data (520 pixels by 692 pixels) of a single crystal of BrCH/thiourea at χ =
10°, φ = 0°, T = 20 K with an intensity range of 1500 - 5000.*
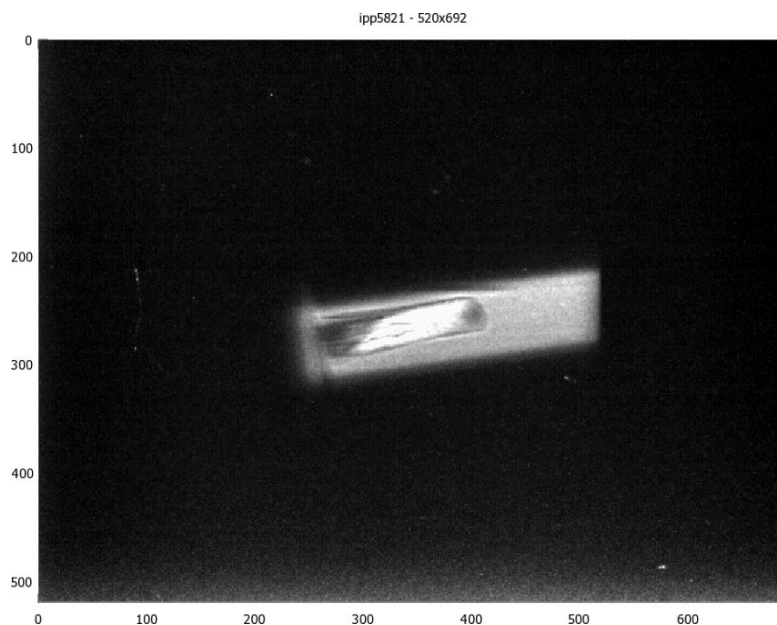
Fig. 3.8 *Raw imaging data (520 pixels by 692 pixels) of a single crystal of BrCH/thiourea at χ =
10°, φ = 0°, T = 20 K with an intensity range of 2000 - 5000.*
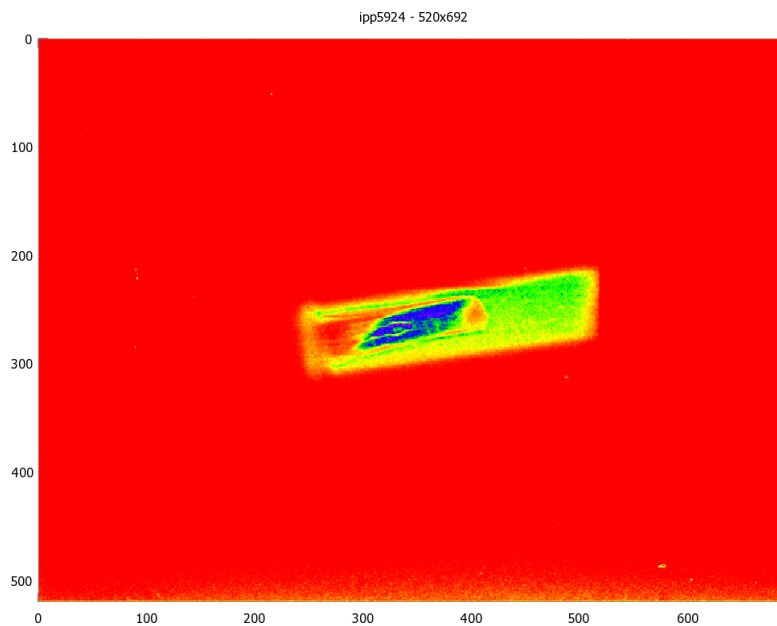
Fig. 3.9 *Raw imaging data (520 pixels by 692 pixels) of a single crystal of BrCH/thiourea at χ = 10°, φ = 0°, T = 20 K with a Rainbow colour scheme and intensity range 2000 - 5000.*
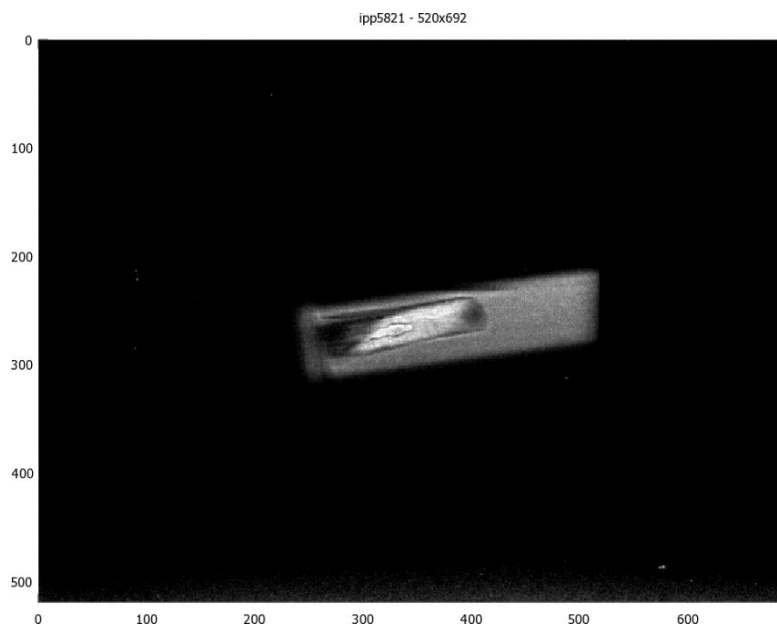
Fig. 3.10 *Raw imaging data (520 pixels by 692 pixels) of a single crystal of BrCH/thiourea at χ = 10°, φ = 0°, T = 20 K with an intensity range of 2600 - 6000.*

To prepare the XB images shown in the figures and movies, the raw data from the detector were rotated clockwise by 8° to correct for the fact that, in the raw data, the true horizontal direction of the beam (*x*-axis) is tilted by 8° from the horizontal direction of

41

the detector (this tilt arises from a correlation between the vertical and horizontal scattering angles, which is a consequence of the fact that they are each correlated with the wavelength). Fig 3.11 shows the same data set as Figs 3.6, 3.7, 3.8, and 3.10 but with the tilt correction and labelling applied.
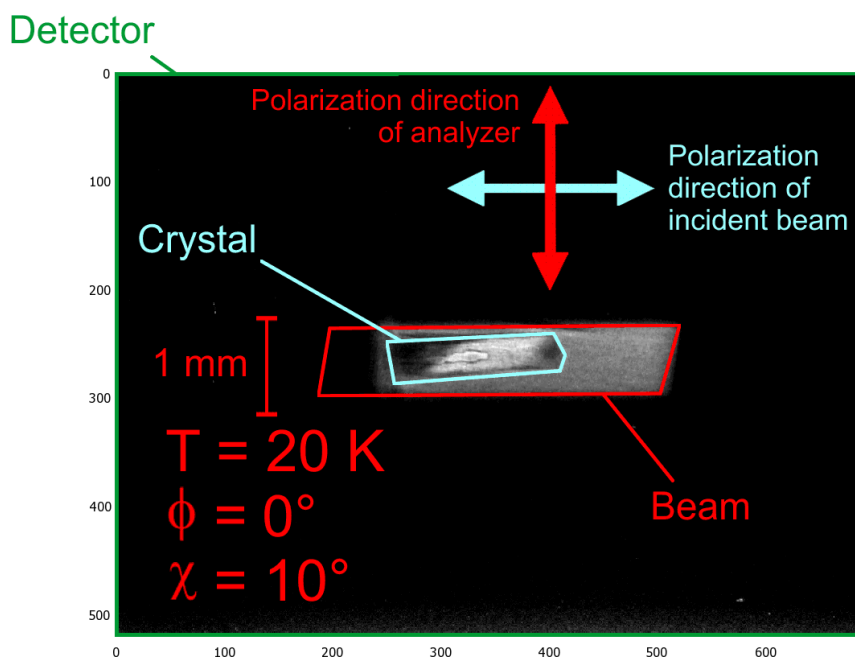
Fig. 3.11 *Imaging data of a single crystal of BrCH/thiourea at $\chi = 10°$, $\varphi = 0°$, $T = 20 K$ with Tilt corrected and labelled image.*

After correction for the 8° tilt, the XB images shown in the composite image figures were prepared by cropping the raw data to show only the region of the detector corresponding to the X-ray beam. In all figures, cropping in the vertical direction was done to show the full width of the beam (vertical width *ca*. 0.8 mm). In the horizontal direction, the raw data from the detector were cropped in the following ways: (a) to prepare Figs 3.14 and 3.17a, the raw data were cropped to show the full width of the beam (horizontal width *ca*. 4.0 mm), and (b) to prepare Figs 3.13, 3.18, 3.19 and 3.20, the raw data were cropped to show only the region containing the crystal (horizontal width *ca*. 3.15 mm). In the XB images in Figs 3.17a, 3.18, 3.19 and 3.20, the goniometer head appears at the left-hand side of the image. The XB images shown in the movies comprise the full raw data from the detector after correction for the 8° tilt.

Polarizing optical microscopy (Fig. 3.17b) was carried out at ambient temperature (293 K) for a single crystal of BrCH/thiourea using a Leica MZ12.5 stereomicroscope (Leica DFC 480 digital camera and Leica CLS 150X light source) with the polarizer and analyzer in crossed-polarizer configuration. The crystal was mounted on a glass slide with the c-axis of the rhombohedral thiourea host tunnel structure horizontal (i.e. perpendicular to the direction of view). The c-axis is parallel to the long-needle axis of the crystal morphology and is the optic axis of the uni-axial (rhombohedral) crystal. As shown in Fig. 3.17b, the orientation of the crystal was changed by rotation about an axis parallel to the direction of view (i.e. perpendicular to the c-axis) in steps of 10°, and the polarizing optical micrograph was recorded for each orientation.

Finally, we consider sources of experimental error in the XBI measurements reported here. Alignment of the crystal on the goniometer was carried out by visual inspection, with the long axis of the needle morphology (c-axis) aligned parallel to the φ rotation axis of the goniometer. As a consequence of the visual alignment procedure, an experimental error of the order of a few degrees may be introduced into the values of χ and φ. Moreover, the experimental error in the value of χ may be correlated to the value of φ and vice versa. In this regard, slight misalignment of the crystal is evident from the movies (Movies S2, S4 and S5) that involve variation of φ for fixed χ, in which the c-axis of the crystal is actually observed to precess slightly around the φ rotation axis (as a consequence, the value of χ is not strictly constant, and fluctuates slightly as φ is varied). These experimental errors in crystal alignment may also contribute to the fact that values of χ measured directly from the XB images (i.e. the angle between the long-axis of the crystal morphology (c-axis) and the horizontal direction in the image) differ by a few degrees from the values of χ quoted from the experimental set-up (corresponding to average discrepancies of $ca.$ 4.7° for the images in Fig. 3.13 and $ca.$ 6.6° for the images in Fig. 3.18). A contribution to these discrepancies may also arise from any errors inherent in the estimated tilt correction discussed above.

3.3. Results

To demonstrate the XB imaging (XBI) technique, we focus on materials containing brominated organic molecules, using incident linearly polarized X-rays from a synchrotron source (beamline B16 at the Diamond Light Source[20]) with energy corresponding to the Br K-edge. In this case XB depends on the orientation of C–Br bonds relative to the incident polarized X-ray beam[1, 2, 21-23].

3.3.1 X-ray Birefringence Imaging on 1-Bromoadamantane/Thiourea Inclusion Compound

To demonstrate the sensitivity and utility of XBI for spatially resolved mapping, our first experiment focused on a model material in which all C–Br bonds are parallel to each other – specifically, the thiourea inclusion compound containing 1-bromoadamantane (1-BA) guest molecules (Fig. 3.12)[24]. The orientation of the crystal relative to the linearly polarized incident X-ray beam is specified by crystal orientation angles χ and φ defined in Fig. 3.3.
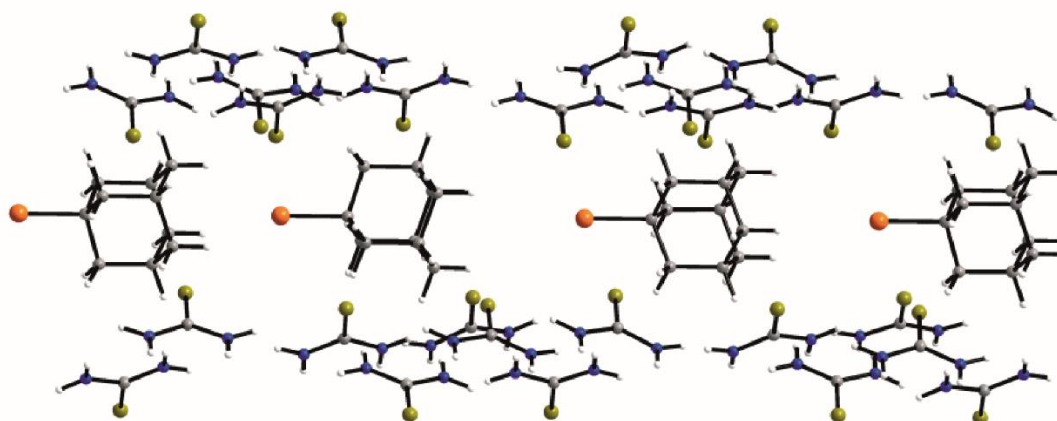
Fig. 3.12 *Structure of 1-BA/thiourea viewed perpendicular to the thiourea host tunnel (horizontal); the C–Br bonds of all 1-BA guest molecules are parallel to the tunnel axis (c-axis) which is also parallel to the long-needle axis of the crystal morphology.*

Fig. 3.13 and Movie S1 show XB images for a single crystal of 1-BA/thiourea as a function of χ (with φ fixed). Each image shows the transmitted X-ray intensity for a

specific orientation of the crystal (brightness scales proportionally with intensity). In Fig. 3.13, the intensity varies significantly as a function of χ, with maximum brightness at $\chi \approx 45°$ and minimum brightness at $\chi \approx 90°$

For $\chi = 0°$, the crystal c-axis is horizontal (xz-plane), parallel to the linearly polarized incident X-ray beam. Maximum intensity arises when the orientation of the C–Br bonds is at *ca*. 45° with respect to the direction of linear polarization of the incident X-ray beam. For each crystal orientation, the transmitted intensity is uniform across the entire crystal, indicating that the crystal comprises a single orientational domain. The observed dependence of intensity on χ is directly analogous to the behaviour of a uni-axial crystal in the polarizing optical microscope. Fig. 3.14 and Movie S2 show XB images recorded for 1-BA/thiourea as a function of φ (with χ fixed at 40°, close to the maximum transmitted intensity in Fig. 3.2). As the orientational properties of the C–Br bonds are not altered by rotation around the bond axis, no significant change in transmitted intensity as a function of φ is observed.
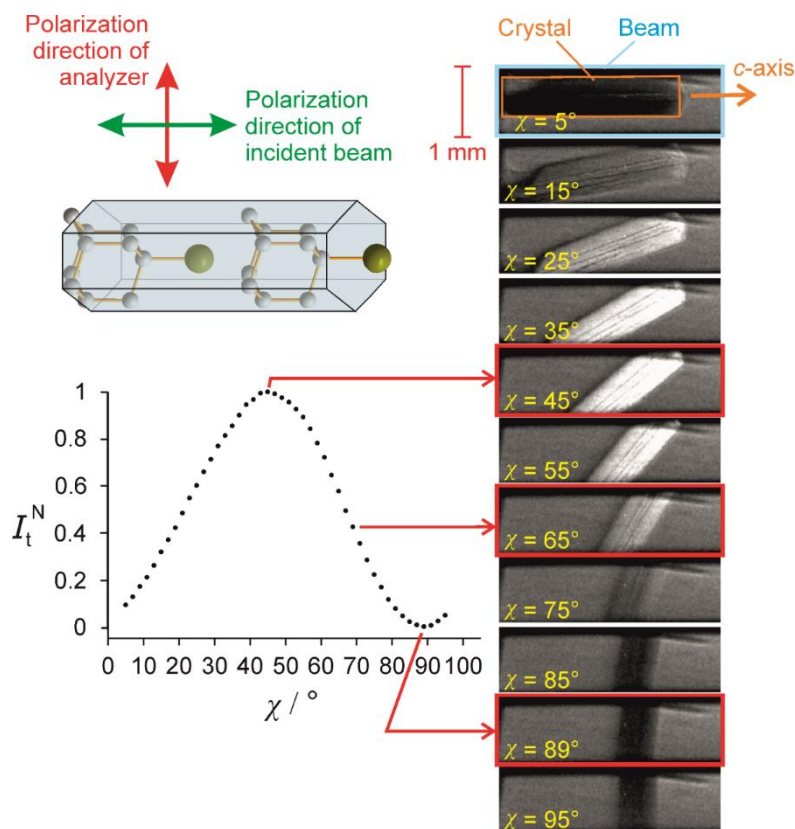
Fig. 3.13 *XB images for a model material with uni-directional alignment of C–Br bonds. XBI data recorded at 280 K for a single crystal of 1-BA/thiourea as a function of χ (with φ fixed). The images represent spatially resolved maps of transmitted X-ray intensity across the crystal. Relative brightness in the images scales with X-ray intensity. The variation of normalized transmitted intensity (I_t^N) as a function of χ is shown in the plot at the left side, using data from all images recorded in the experiment (with χ varied in steps of 2°). To construct this plot, transmitted intensity I_t was measured by integrating the intensity across a region of the image with dimensions 62.5 μm × 192 μm at the centre of the crystal, and was scaled to give a normalized value in the range $0 \leq I_t^N \leq 1$.*
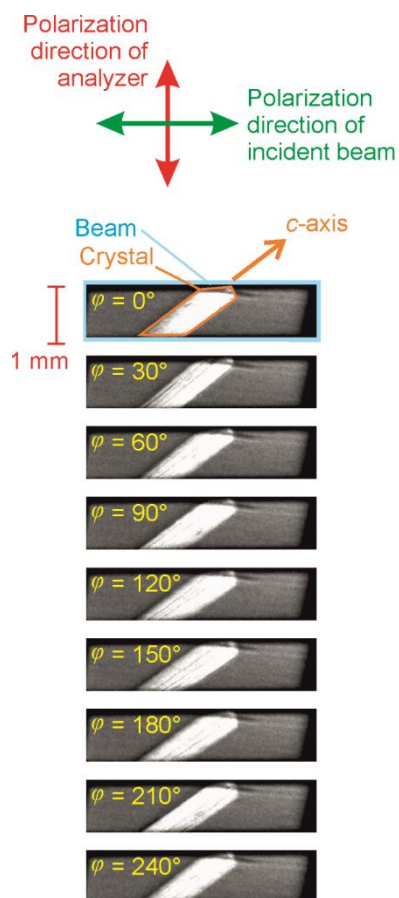
Fig. 3.14 *XBI data recorded at 280 K for a single crystal of 1-BA/thiourea as a function of φ with χ fixed at 40° (i.e. close to maximum transmitted intensity in Fig. 3.13, which corresponds to χ = 45°).*

3.3.2 VT X-ray Birefringence Imaging Bromocyclohexane/Thiourea Inclusion Compound

To assess the potential to exploit XBI to probe changes in molecular orientational distributions as a function of temperature, XBI experiments were carried out on a single crystal of the thiourea inclusion compound containing bromocyclohexane (BrCH) guest molecules. This material is known to undergo a phase transition at 233 K[25] from a high-temperature phase in which the orientational distribution of the BrCH guest molecules is essentially isotropic (as a result of rapid molecular motion) to a low-temperature phase in which the BrCH molecules become orientationally ordered (Fig. 3.15). Specifically the C–Br bonds of all BrCH molecules are oriented at $\psi \approx 52.5°$ and $\omega \approx 3.5°$ with respect to the thiourea host structure, as defined in Fig. 3.16.
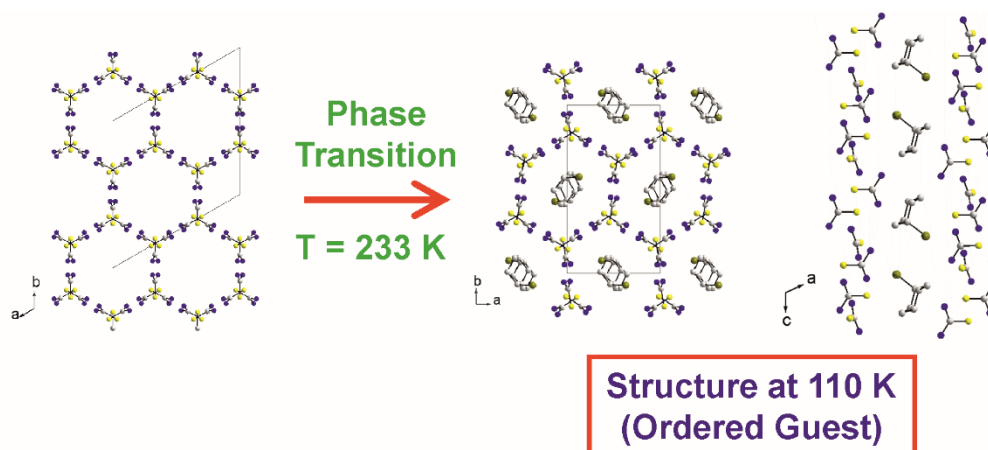
Fig. 3.15 *Structural changes associated with the phase transition in BrCH/thiourea. Left: rhombohedral high-temperature phase viewed along the thiourea host tunnels (the isotropically disordered BrCH guests are not shown). Middle and right: monoclinic low-temperature phase (110 K) viewed along the host tunnels (middle) and perpendicular to the tunnel (right) (H atoms omitted for clarity); the C–Br bonds of all BrCH guests form an angle $\psi \approx 52.5°$ with respect to the tunnel axis (vertical in right-hand figure).*
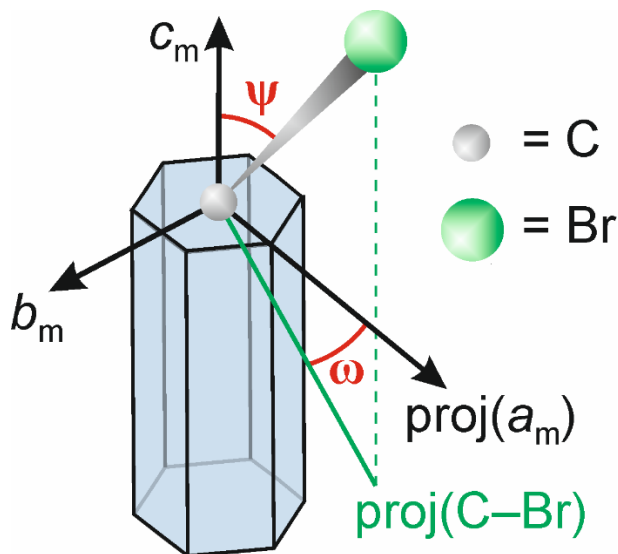
Fig. 3.16 *Definition of angles ψ and ω specifying the orientation of the C–Br bond relative to the thiourea host structure in the low-temperature phase.*

XB images recorded for BrCH/thiourea at 298 K (Fig. 3.17a; Movies S3, S4) demonstrate that, for the high-temperature phase, there is no variation in transmitted X-ray intensity as a function of crystal orientation, fully consistent with the isotropic orientational distribution of the C–Br bonds of the BrCH guest molecules in this phase.

48

In contrast, under the same conditions in the polarizing optical microscope in crossed-polarizer configuration (Fig. 3.17b), a single crystal of BrCH/thiourea exhibits the classical behaviour of a uni-axial crystal, with minimum transmitted intensity when the optic axis is parallel to the polarizer or analyzer and with maximum transmitted intensity when the optic axis is at 45° to these directions (for BrCH/thiourea, the optic axis is the c-axis of the rhombohedral thiourea host structure, parallel to the long-needle axis of the crystal morphology in Fig. 3.17b). These results clearly demonstrate the difference between optical and X-ray birefringence: the former depends on the overall crystal symmetry whereas the latter depends on the local orientational properties in the vicinity of the X-ray absorbing atom within the material (i.e. in the present case, the orientational distribution of the C–Br bonds).
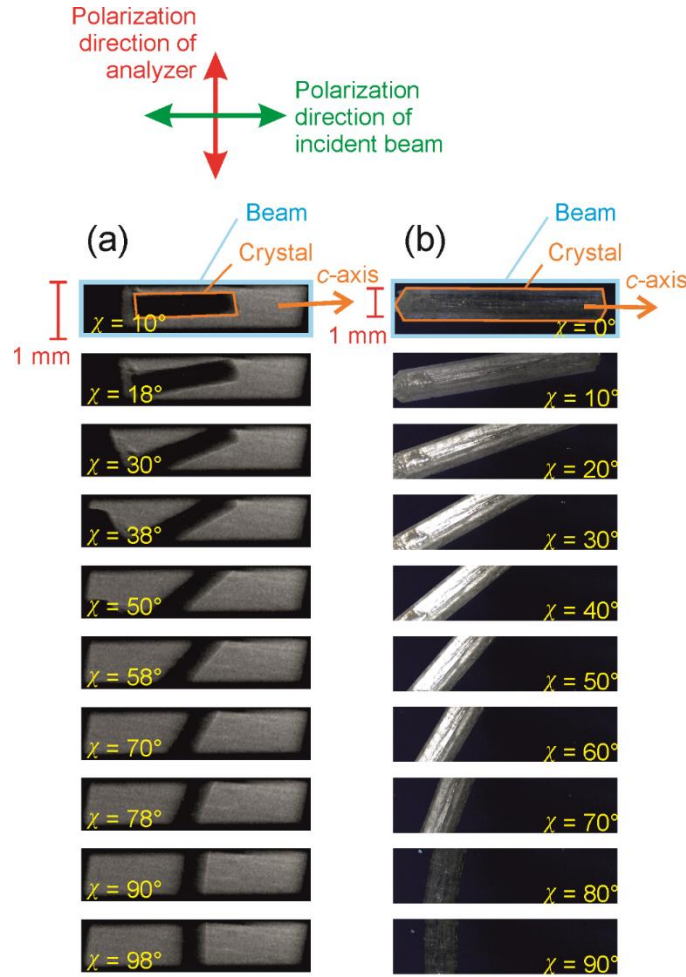
Fig. 3.17 *Comparison of XBI and polarizing optical microscopy. (a) XB images and (b) polarizing optical microscope images recorded as a function of χ for single crystals of BrCH/thiourea in the high temperature phase [298 K for (a) and 293 K for (b)].*

In the low-temperature phase of BrCH/thiourea, the XB behaviour changes dramatically thanks to increased order following the phase transition. For BrCH/thiourea, the c-axis is the tunnel axis of the thiourea host structure in both the HT and LT phases. With respect to the hexagonal unit cell (a_h, b_h, c_h) of the HT phase, the crystal orientation $\{\chi = 0°,\ \varphi = 0°\}$ has the c_h-axis parallel to the laboratory x-axis and the (100) plane perpendicular to the z-axis. With respect to the monoclinic unit cell (a_m, b_m, c_m) of the LT phase, in the crystal orientation $\{\chi = 0°,\ \varphi = 0°\}$, the c_m-axis is parallel to the laboratory x-axis, the b_m-axis is parallel to the z-axis, and the projection of the a_m-axis on the plane perpendicular to the c_m-axis [denoted proj(a_m)] is perpendicular to the xz-plane.

At 20 K, for the crystal orientation {$\chi = 10°$, $\varphi = 0°$} (top-left image in Fig. 3.18; top image in Fig. 3.19), it is evident that the crystal comprises orientationally distinct domains. Thus, a large parallelogram-shaped domain (with dimensions of a few hundred μm) dominates the central region of the crystal (bright region in the image), with two smaller domains (dark regions) at each end of the crystal. The domain boundaries between the major domain and the two minor domains are parallel to each other and intersect the c-axis at an angle of ca. 136°, allowing the domain boundary to be assigned as the crystallographic ($10\bar{1}$) plane. For crystal orientation {$\chi = 10°$, $\varphi = 180°$}, the XB image (top-right image in Fig. 3.18; see also Movie S5) is essentially an "inverted" form of the image for {$\chi = 10°$, $\varphi = 0°$}, as expected given that these crystal orientations correspond to the incident X-ray beam passing in opposite directions through the crystal.
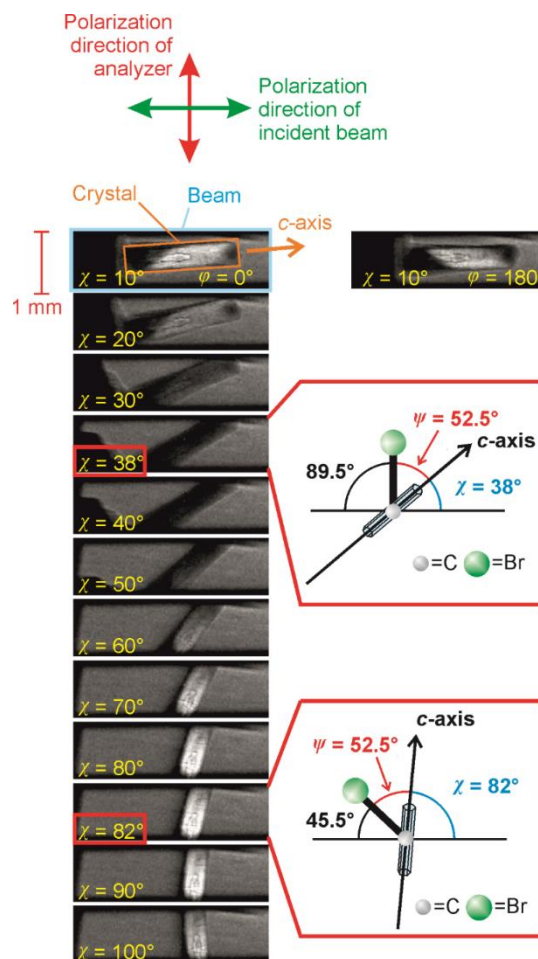
Fig. 3.18 *XB images for the orientationally ordered phase of BrCH/thiourea. XBI data recorded at 20 K for a single crystal of BrCH/thiourea as a function of χ (with φ fixed at 0°). Maximum brightness (for the large central domain) arises when the C–Br bonds form an angle of ca. 45° with respect to the linearly polarized incident beam (achieved at χ ≈ 82°) and minimum brightness arises when the C–Br bonds form an angle of ca. 90° with respect to the linearly polarized incident beam (achieved at χ ≈ 38°).*

Fig. 3.18 (left side) and Movie S6 show XB images recorded as a function of χ (with φ fixed at 0°) for BrCH/thiourea in the low-temperature phase. For $\varphi = 0°$, the C–Br bonds in the major domain are very nearly perpendicular to the direction of propagation of the incident X-ray beam.
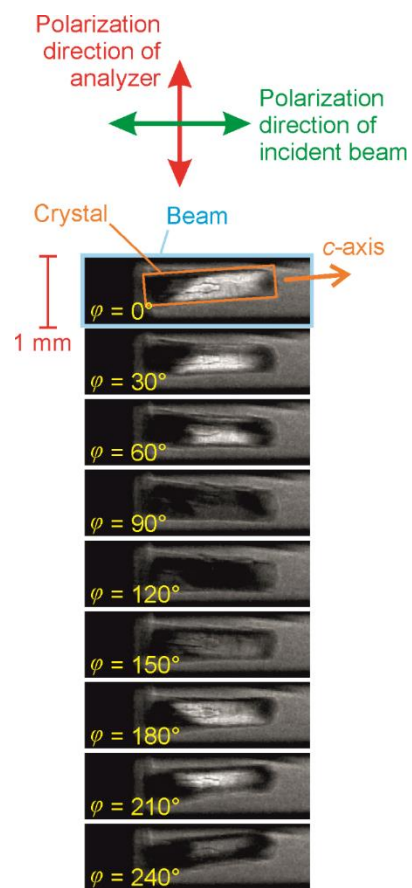
Fig. 3.19 *XBI data recorded at 20 K for a single crystal of BrCH/thiourea as a function of φ (with χ fixed at 10°). The images for the specific orientations {χ = 10°, φ = 0°} and {χ = 10°, φ = 180°} are also shown in Fig. 3.6 and discussed in the text.*
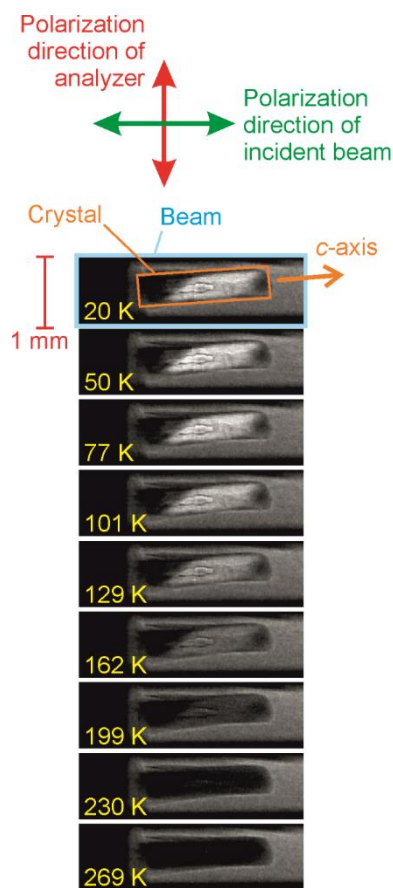
Fig. 3.20 *XBI data recorded for BrCH/thiourea as a function of temperature, with the crystal orientation fixed at {χ = 10°, φ = 0°}. The phase transition temperature is 233 K. The XB images for a more comprehensive set of temperatures within the same range are shown in Movie S7.*

For $\varphi = 0°$, the b_m-axis of the crystal in the LT phase is parallel to the laboratory z-axis. Hence, as the angle ω (defined in Fig. 3.1e) is known[25] to be only *ca.* 3.5°, the C–Br bonds in the major domain are very nearly perpendicular to the direction of propagation of the incident X-ray beam.

The transmitted intensity for the major domain varies significantly with χ; maxima in intensity are separated by $\Delta\chi = 90°$ and the intervening minimum is separated from these maxima by $\Delta\chi = 45°$. As shown in Fig. 3.18 and given that the C–Br bonds are known[25] to form an angle $\psi \approx 52.5°$ with respect to the tunnel (*c*-axis) of the thiourea host structure in the low-temperature phase, the observed intensity maximum (at $\chi \approx 82°$) corresponds to the C–Br bonds forming an angle of *ca.* 45° with respect to the direction

54

of polarization of the incident X-ray beam (horizontal). Correspondingly, minimum transmitted intensity (observed at $\chi \approx 38°$ in Fig. 3.18) occurs when the C–Br bonds form an angle of $ca.$ 90° with respect to the direction of polarization of the incident X-ray beam.

For BrCH/thiourea, the c-axis is the tunnel axis of the thiourea host structure in both the HT and LT phases. With respect to the hexagonal unit cell (a_h, b_h, c_h) of the HT phase, the crystal orientation $\{\chi = 0°, \varphi = 0°\}$ has the c_h-axis parallel to the laboratory x-axis and the (100) plane perpendicular to the z-axis. With respect to the monoclinic unit cell (a_m, b_m, c_m) of the LT phase, in the crystal orientation $\{\chi = 0°, \varphi = 0°\}$, the c_m-axis is parallel to the laboratory x-axis, the b_m-axis is parallel to the z-axis, and the projection of the a_m-axis on the plane perpendicular to the c_m-axis [denoted proj(a_m)] is perpendicular to the xz-plane.

Thus, the χ-dependence of the XB images shown (for $\varphi = 0°$) in Fig. 3.18 is analogous to the behaviour of a uni-axial crystal in the polarizing optical microscope, with the direction of the C–Br bond representing the "optic axis" in the case of the XBI data. XB images (Fig. 3.19 and Movie S7) recorded as a function of temperature within the low-temperature phase indicate that there is no change in the domain structure with temperature.

The changes of transmitted X-ray intensity as a function of temperature in this material have been rationalized previously[2] from XB studies using a focused X-ray beam. However our imaging experiments explored a lower temperature range (a low point of 20K compared to a low of 100K) where the birefringence signal plateaus out and stops increasing as temperature decreases.
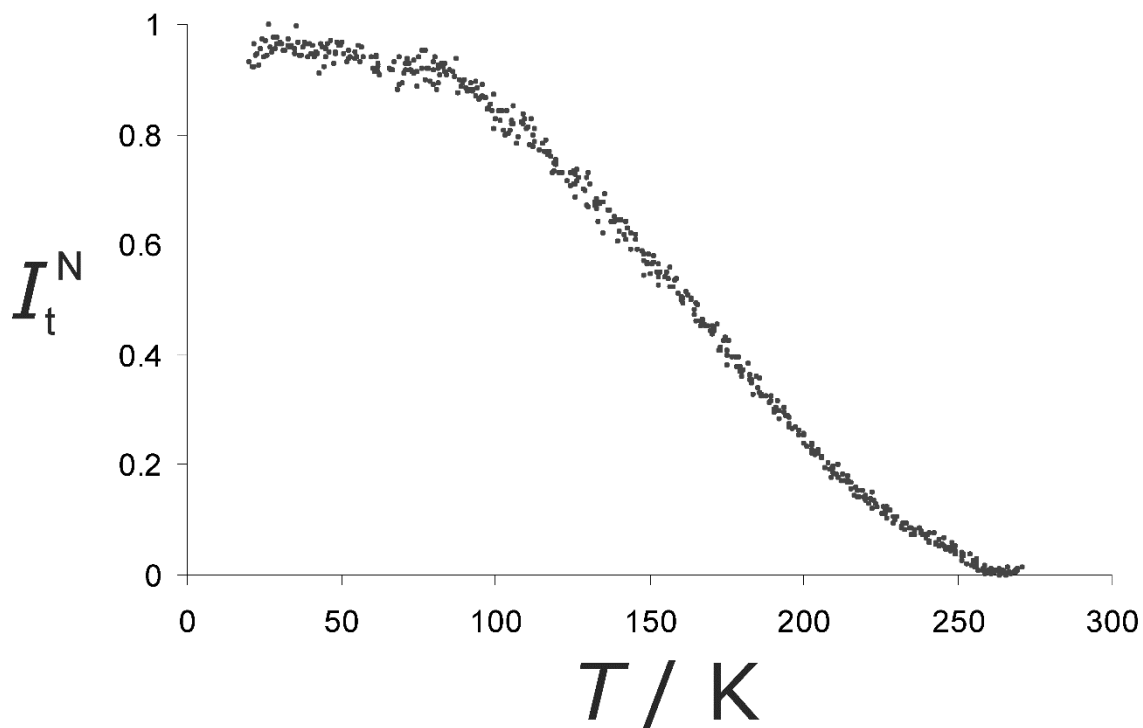
Fig. 3.21 *Plot of the normalized transmitted intensity as for a crystal of BrCH/thiourea as a function of temperature constructed by extracting intensities out of XBI data. To construct this plot, transmitted intensity I_t was measured by integrating the intensity across a region of the image with dimensions 62.5 μm × 192 μm at the centre of the crystal, and was scaled to give a normalized value in the range $0 \leq I_t^N \leq 1$.*
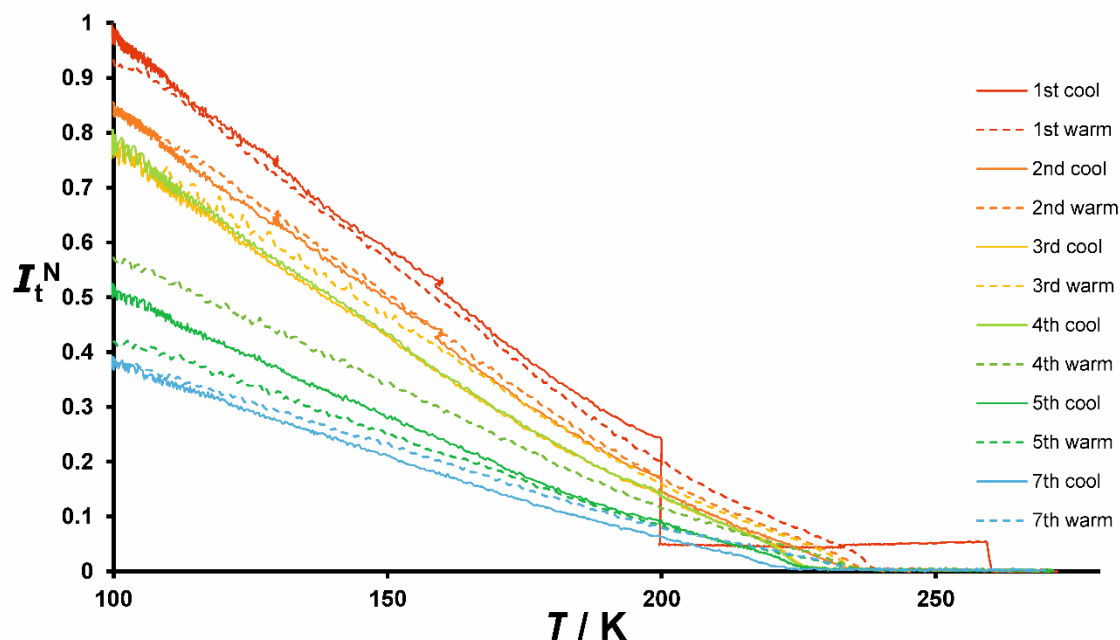
Fig. 3.22 *Plot of the normalized transmitted intensity as for a crystal of BrCH/thiourea as a function of temperature using point detector X-ray birefringence data. The large discontinuity during the first cool occurs when the φ value was altered to find the position of maximum birefringence, smaller discontinuities occur during the first cool and second cool when cooling was halted to perform χ and φ scans at different temperatures.*

Fig. 3.22 shows how repeated temperature cycles give progressively weaker birefringent signals with the seventh temperature cycle showing only ~40% of the birefringence of the first cycle. This reduction in signal might arise due to beam damage (prolonged exposure to X-rays at the adsorption edge might cause guest molecules to break apart) or it might arise due to loss of crystallinity (repeated phase transitions back and forth might damage the crystal structure). It is also interesting to note that the domain boundaries remain the same during repeated temperature cycles. Some hysteresis is also observed between the start of signal on cooling cycles and the end of signal on the warming cycles which suggests that there is an activation barrier associated with the order-disorder phase transition.

3.3.3. Animated Movies of Imaging Scans

Movies S1 to S7 consist of a sequence of still images with minor processing. Each movie starts with a title slide (shown for 4 s), followed by an annotated initial image (shown for 5 s), and then moves quickly through the subsequent images (each image is shown for 0.2 or 0.3 s) to show the sequence of changes in the XB images as a function of changing the orientation of the crystal about a specific axis at fixed temperature (for Movies S1 to S6) or as a function of temperature for fixed crystal orientation (for Movie S7).

Further details are now given of the specific XBI experiments in which the XB images shown in the figures and movies were recorded.

- Movie S1 - Animation constructed from XBI data recorded at 280 K for 1-BA/thiourea as a function of χ (5° to 93°) with φ fixed at 120°. A selection of the images contained in this animation are shown in Fig. 3.13.

- Movie S2 - Animation constructed from XBI data recorded at 280 K for 1-BA/thiourea as a function of φ (0° to 240°) with χ fixed at 40°. A selection of the images contained in this animation are shown in Fig. 3.14.

- Movie S3 - Animation constructed from XBI data recorded at 298 K for BrCH/thiourea as a function of χ (10° to 98°) with φ fixed at 0°. A selection of the images contained in this animation are shown in Fig. 3.17a.

- Movie S4 - Animation constructed from XBI data recorded at 298 K for BrCH/thiourea as a function of φ (0° to 240°) with χ fixed at 10°.

- Movie S5 - Animation constructed from XBI data recorded at 20 K for BrCH/thiourea as a function of φ (0° to 240°) with χ fixed at 10°.

A selection of the images contained in this animation are shown in Fig. 3.19.

- Movie S6 - Animation constructed from XBI data recorded at 20 K for BrCH/thiourea as a function of χ (10° to 98°) with φ fixed at 0°. A selection of the images contained in this animation are shown in Fig. 3.18.

- Movie S7 - Animation constructed from XBI data recorded for BrCH/thiourea as a function of temperature (from 20 K to 269 K) with the crystal orientation fixed at $\chi = 10°$ and $\varphi = 0°$. The phase transition temperature is 233 K. A selection of the images contained in this animation are shown in Fig. 3.20.

3.4 Conclusions

As demonstrated above, XBI enables spatially resolved mapping of the orientational properties of specific types of molecule (or bond) in materials, particularly in cases (e.g. partially ordered materials, multiply twinned crystals, or other materials with complex domain structures), for which the application of X-ray diffraction techniques may not be feasible. Although demonstrated here for the study of single-crystal samples, there is no requirement for crystallinity as XB is sensitive specifically to local molecular orientations; thus, XBI may be applied to any material (including liquids or amorphous solids) with an anisotropic distribution of molecular orientations. The results reported for BrCH/thiourea in the low-temperature phase highlight the potential to exploit XBI for spatially resolved analysis of orientationally distinct domains. Knowledge of domain structures (in particular, aspects such as domain sizes, the orientational relationships between domains and the nature of domain boundaries) can be critical for controlling the performance of electronic, optical and magnetic devices[26, 27] and the mechanical properties of biomaterials[28].

As XBI is a full-field imaging technique, with the entire image recorded simultaneously, the measurement of XB images is fast (exposure time of 1 s for each image shown here) leading to the potential to study dynamic processes (e.g. the propagation of domain boundaries during phase transitions).

In contrast, other techniques[29-33] for imaging materials using incident X-ray radiation (e.g. scanning X-ray microscopy and X-ray topography) generally involve scanning a focused X-ray beam across the material (leading to the construction of a spatially resolved image by analysis of the interaction of the beam with the material at each position of the beam). The time required to record a single image in XBI is clearly much faster than would be the case with a scanning probe. One consequence is that the overall radiation dose received by the sample should be significantly lower in the case of XBI, suggesting that XBI may be advantageous in studying materials that are susceptible to radiation damage.

The time to record a single image in XBI could be reduced to *ca*. 1 ms for a storage ring undulator source (rather than the bending-magnet source used here) and utilizing a faster X-ray detector than that used in the present study, and could even be reduced to less than 100 fs using a single pulse from an X-ray free-electron laser, creating a new opportunity for imaging ultra-fast molecular dynamics.

3.5 References

[1]   B. A. Palmer, B. M. Kariuki, K. D. M. Harris, S. P. Collins, *J. Phys. Chem Lett.*, **2011**, 2, 2346-2351.
[2]   B. A. Palmer et al., *J. Phys. Chem. Lett.*, **2012**, 3, 3216-3222.
[3]   B. A. Collins et al., *Nature Mater.*, **2012**, 536-543.
[4]   Y. Joly, S. P. Collins, S. Grenier, H. C. N. Tolentino, M. De Santis, *Phys. Rev. B*, **2012**, 86, 220101(R).
[5]   B. A. Palmer, G. R. Edwards-Gau, B. M. Kariuki, K. D. M. Harris, I. P. Dolbnya, S. P. Collins, *Science*, **2014**, 344, 1013-1016.
[6]   El Goresy, M. Chen, L. Dubrovinsky, P. Gillet, G. Graup, *Science*, **2001**, 293, 1467-1470.
[7]   N. H. Hartshorne, A. Stuart, *Practical Optical Crystallography*, **1969**, Edward Arnold, London**.**
[8]   W. Kaminsky, K. Claborn, B. Kahr, *Chem. Soc. Rev.*, **2004**, 33, 514-525.
[9]   L. Schmidt-Mende et al., *Science*, **2001**, 293, 1119-1122.
[10]   H. Yang, N. Coombs, G. A. Ozin, , *Nature*, **1997**, 386, 692-695.
[11]   H. E. Warriner, S. H. J. Idziak, N. L. Slack, P. Davidson, C. R. Safinya, *Science*, **1996**, 271, 969-973.
[12]   S. E. Malawista, H. Sato, K. G. Bensch, *Science*, **1968**, 160, 770-772.
[13]   K. Iverson, S. W. Tam-Chang., *J. Am. Chem. Soc.*, **1999**, 121, 5801-5802.
[14]   M. Kahn, J. L. Cook, F. Bonar, P. Harcourt, M Astrom, *Sports Med.*, **1999**, 27, 393-408.
[15]   C. Hughes, C. W. Archer, I ap Gwynn., *Eur. Cells Mater.*, **2005**, 9, 68-84.
[16]   W. Jin et al., *Proc. Natl. Acad. Sci.*, **2003**, 100, 15294-15298.
[17]   Y. Chen et al., *Appl. Phys. Lett.*, **2009**, 94, 053901.
[18]   K. Kerkam, C. Viney, D. Kapla, S. Lombardi, *Nature*, **1991**, 349, 596-598.
[19]   S. P. Collins, I. Dolbnya, B. A. Palmer, G. R. Edwards-Gau, A. Morte-Ródenas, B. M. Kariuki, G Keat Lim, K. D. M. Harris, Y. Joly, *J. Phys.: Conf. Ser.*, **2013**, 425.
[20]   K. J. S. Sawhney et al., *AIP Conf. Proc.*, **2010**, 1234, 387-390.
[21]   S. P. Collins et al., *J. Phys. Conf. Ser.*, **2013**, 13, 132015.
[22]   C. Brouder, *J. Phys.-Condens. Mat.*, **1990**, 2, 701-738.
[23]   S. P. Collins et al., *J. Phys.-Condens. Mat.*, **2002**, 14, 123-134.
[24]   M.-H. Chao, B. M. Kariuki, K. D. M. Harris, S. P. Collins, D. Laundy, *Angew. Chemie Int. Ed.*, **2003**, 42, 2982-2985.

[25]   B. A. Palmer, B. M. Kariuki, A. Morte-Ródenas, K. D. M. Harris, *Cryst. Growth Des.*, **2012**, 12, 577-582.
[26]   H. Sirringhaus et al., *Appl. Phys. Lett.*, **2000**, 77, 406-408.
[27]   H. Sirringhaus et al., *Nature*, **1999**, 401, 685-688.
[28]   J. Stasiak, A Zaffora, M. L. Constantino, A. Pandolfi, G. D. Moggridge, *Func. Mater. Lett.*, **2010**, 3, 249-252.
[29]   H. Ade, B. Hsiao, *Science*, **1993**, 262, 1427-1429.
[30]   D. Sayre, N. H. Chapman, *Acta Crystallogr.*, **1995**, A51, 237-252.
[31]   D. K. Bowen, B. K. Tanner, *High Resolution X-ray Diffractometry and Topography* **1998**, Taylor & Francis, London.
[32]   Howells, C. Jacobsen, T. Warwick, A. Van den Bos. in J. C. H. Spence P. W. Hawkes. *Science of Microscopy,* **2007**, 835-926, Springer, New York.
[33]   P. Thibault et al., *Science*, **2008**, 321, 379-382.

Chapter 4 – X-ray Birefringence Imaging of Materials with Anisotropic Molecular Dynamics

4.1 Introduction

X-ray Birefringence Imaging (XBI), reported in the previous chapter, is an effective tool for spatially resolved mapping of the local orientational properties of anisotropic materials but in order to further develop this method we must better understand the technique. We have already shown that XBI can image entire crystals and yields space-averaged information for the depth of the crystal but many questions still remain about the properties of the technique. Here we attempt to answer one of those questions by investigating what information XBI can yield about dynamic processes.

In this chapter we report a series of XBI experiments on model materials that are known to undergo well-defined reorientational dynamics, specifically urea inclusion compounds containing α,ω-dibromoalkane $[Br(CH_2)_nBr]$ guest molecules. Urea inclusion compounds[1-6] comprise a crystalline urea host tunnel structure [7-9] (diameter *ca*. 5.5Å) formed from a hydrogen-bonded hexagonal network of urea molecules. Guest molecules of appropriate dimensions (typically based on an *n*-alkane chain) are densely packed within these tunnels. Along the tunnel axis, the periodic repeat distance of the guest substructure is usually incommensurate[8-12] with the periodic repeat distance of the urea host substructure along the tunnel axis. The experiments reported here were carried out on the urea inclusion compound containing 1,8-dibromooctane (1,8-DBO) guest molecules and the urea inclusion compound containing 1,10-dibromodecane (1,10-DBD) guest molecules, as the guest molecules in these materials are known to undergo uni-axial reorientational dynamics. These materials undergo a low-temperature phase transition involving a distortion of the urea host structure[13-15] from hexagonal symmetry (high-temperature phase) to orthorhombic symmetry (low-temperature phase). The phase transition temperature is 157 K for 1,8-DBO/urea and 140 K for 1,10-DBD/urea.

A variety of experimental techniques have been used to investigate the dynamic properties of the guest molecules in these materials, including solid-state ^{1}H NMR[16] solid-state ^{2}H NMR[14] and incoherent quasielastic neutron scattering (IQNS)[17]. IQNS studies on urea inclusion compounds containing α,ω-dibromoalkane guests (with $n = 8$, 9, 10) demonstrated that, in the high-temperature phase, the guest molecules undergo rapid reorientation about the tunnel axis (timescale of motion $ca.$ $10^{-12} - 10^{-10}$ s) as well as restricted translational diffusion along this axis. In contrast, in the low-temperature phase for 1,10-DBD/urea at 120 K, no reorientational motions about the tunnel axis are effective on the IQNS timescale. The results from solid-state ^{2}H NMR lineshape analysis and solid-state ^{2}H NMR spin-lattice relaxation time measurements also concur that, in the high-temperature phase (at 240 K) for 1,10-DBD/urea, the guest molecules undergo rapid reorientation about the tunnel axis (on a timescale shorter than 10^{-8} s). However, solid-state ^{2}H NMR lineshape analysis (which can probe significantly slower dynamic processes IQNS) indicates clearly that the guest molecules still undergo uni-axial reorientational dynamics in the low-temperature phase, and the results suggest that there is no significant discontinuity in the dynamics of the guest molecules at the phase transition temperature. At 140 K, the dynamics of the guest molecules are in the "intermediate motion regime" for ^{2}H NMR (10^{-8} s $< \tau < 10^{-3}$ s; where τ denotes the timescale of the motion). At 100 K, however, the guest molecules are in the slow motion regime ($\tau > 10^{-3}$ s) with respect to the timescale probed by ^{2}H NMR lineshape analysis.

Polarized Raman spectroscopy studies of oriented single-crystal samples of α,ω-dibromoalkane/urea inclusion compounds have shown[18] that the α,ω-dibromoalkane guest molecules exist in the "all-*trans*" conformation, with a small proportion (*ca.* 7%) of *gauche* end-groups. Thus, for α,ω-dibromoalkane guest molecules with the predominant (*ca.* 93%) *trans* end-group conformation undergoing rapid reorientation about an axis parallel to the tunnel axis of the urea host structure, the C−Br bonds are distributed on a cone with semi-angle *ca.* 35.5° as seen in Fig 4.1.
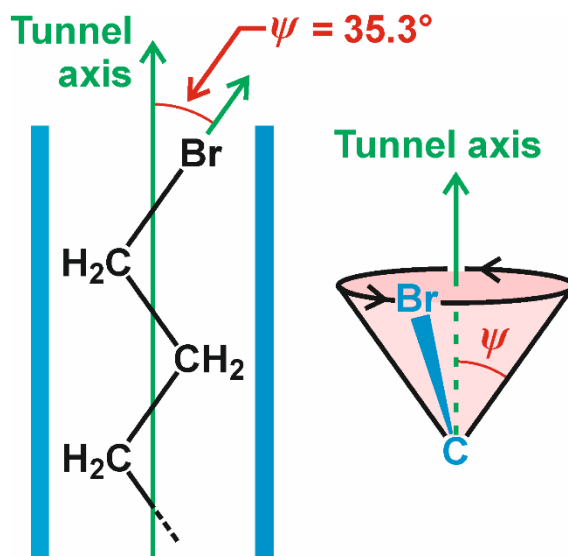
Fig. 4.1 *Figure showing the C–Br bond within the urea tunnel and precession of the C–Br bond about the tunnel axis.*

The phenomenon of optical birefringence is used extensively to study structural anisotropy of materials through the widespread use of the polarizing optical microscope in many different scientific disciplines. The phenomenon of X-ray birefringence, on the other hand, has been demonstrated only relatively recently[19-23] and has also been shown to be a sensitive probe of the orientational properties of anisotropic materials. However, while optical birefringence is depends on the overall symmetry properties of the material, X-ray birefringence (when studied using an X-ray energy corresponding to an absorption edge in the material) is sensitive to the local orientational properties of individual molecules and/or bonds in the material. By exploiting the capability of X-ray birefringence to yield insights on molecular orientations, the technique has been exploited[20] for accurate determination of bond orientations and for establishing *changes* in molecular orientational distributions as a function of temperature in materials that undergo order-disorder phase transitions[24].

The initial experimental studies of X-ray birefringence described above utilized a narrowly focused incident X-ray beam, and did not provide spatially resolved mapping of the X-ray birefringence across the entire material. Subsequently, we developed a new technique,[25] called X-ray Birefringence Imaging (XBI), which *<u>does</u>* enable

measurements of X-ray birefringence to be carried out in a spatially resolved manner, representing, in several respects, the X-ray analogue of the polarizing optical microscope. It was shown that XBI is a sensitive technique for imaging the local orientational properties of anisotropic materials, including the opportunity to identify the existence of orientationally distinct domain structures and yielding information on the size, spatial distribution, temperature dependence and orientational relationships between such domains.

As in our previous studies, we focus in the present paper on molecular materials containing brominated organic molecules, using incident linearly polarized X-rays (from a synchrotron radiation source) with energy corresponding to the Br K-edge. When studied at an X-ray energy close to an absorption edge of an element in the material, X-ray birefringence depends on the local anisotropy of the bonding environment in the vicinity of the X-ray absorbing atom. In the case of brominated organic materials, the X-ray birefringence phenomenon is dominated by the orientational distribution of the C–Br bonds relative to the incident polarized X-ray beam[19, 20, 25].

The aim of the research described here was to explore, for the first time, the phenomenon of X-ray birefringence in the case of materials in which the molecules undergo *anisotropic molecular dynamics*, and exploiting again the imaging capability of the XBI technique The results reveal that XBI can yield insights on the dynamic properties of the molecules through information on the time-averaged distribution of molecular orientations.

4.2 Experimental

Crystals of the 1,8-dibromooctane/urea and 1,10-dibromodecane/urea inclusion compounds were prepared by cooling solutions of urea and 1,8-dibromooctane or 1,10-dibromodecane (*ca*. 6:1 molar ratio of urea:guest) in methanol from 55 to 20 °C over *ca*. 29 h. The crystals were needle-shaped, with the needle axis corresponding to the tunnel axis of the urea host structure (*c*-axis). In each case, powder X-ray diffraction confirmed that the product was a monophasic sample of the urea inclusion compound.

All X-ray birefringence imaging experiments reported here were carried out on beamline B16 at the Diamond Light Source[26] employing a five-circle, vertical-scattering, Huber eulerian diffractometer. On beamline B16, the incident X-ray beam is greater than 95% linearly polarized in the horizontal plane. All measurements were carried out with an incident X-ray energy of 13.493 keV, which corresponds to the midpoint of the Br K-edge[20] (established from X-ray absorption spectra of BrCH/thiourea recorded in the high-temperature phase, for which the Br K-edge X-ray absorption spectrum is essentially independent of crystal orientation as a consequence of the isotropic orientational disorder of the BrCH guest molecules in the high-temperature phase). For temperature control, a liquid nitrogen helium gas-jet cooler was used.

The XBI experiments reported in this chapter largely follow the same experimental set up as described in Chapter 3 but with the key difference of using a Ge(555) analyser crystal rather than a Si(555) analyser as we were experimenting with different analysers to see if we could improve upon the silicon. In the experimental set-up for XBI a wide-area [dimensions 0.8 mm (vertical) by 4.0 mm (horizontal)] linearly-polarized incident X-ray beam is used and the intensity of the wide X-ray beam emerging from the polarization analyzer is recorded using an area detector, allowing the X-ray birefringence of the whole material to be measured in a spatially resolved manner.

The incident X-ray beam propagates along the z-axis and is linearly polarized along the x-axis. The tunnel axis of the urea host structure (c-axis; long-needle axis of crystal morphology) was maintained in the plane (xy-plane) perpendicular to the direction of propagation of the incident X-ray beam (z-axis). The crystal orientation was altered by variation of angles χ and φ, where χ refers to rotation of the c-axis of the crystal around the laboratory z-axis and φ refers to rotation of the crystal around its c-axis. For $\chi = 0°$, the crystal c-axis is horizontal (xz-plane), parallel to the linearly polarized incident X-ray beam.

With the experimental set-up used in the present work, the spatial resolution is of the order of 10 μm (the spatial resolution of the XB images in the vertical direction (*ca.* 13 μm) is limited by the resolution of the CCD-based detector and the spatial resolution

in the horizontal direction (*ca*. 11 μm) is limited by the penetration of the beam into the polarization analyzer [Ge(555) reflection]). The time to record each XB image was 4 s.

The work in the previous chapter utilized a Si(555) analyser but for this work we employed a Ge(555) analyser as it provides a diffraction angle closer to 90°. Si(555) gives diffraction angle of 94.2° which leads to spatial resolution of ~28 μm (based on the dynamical diffraction extinction depth), whilst Ge(555) gives a diffraction angle of 89.4° which leads to spatial resolution of ~11 μm (based on the dynamical diffraction extinction depth). Therefore the Ge(555) analyser reduces the background signal and improves the resolution of the technique, but it also results in non-uniform background intensities across the beam. In Fig. 4.2 we can see a bright area in the top left corner of the beam, a dark band stretching from the bottom left of the beam to the top right of the beam and another bright area in the bottom right of the beam. The crystal is the brightest region in the middle of the dark band of the beam (Fig. 4.3).
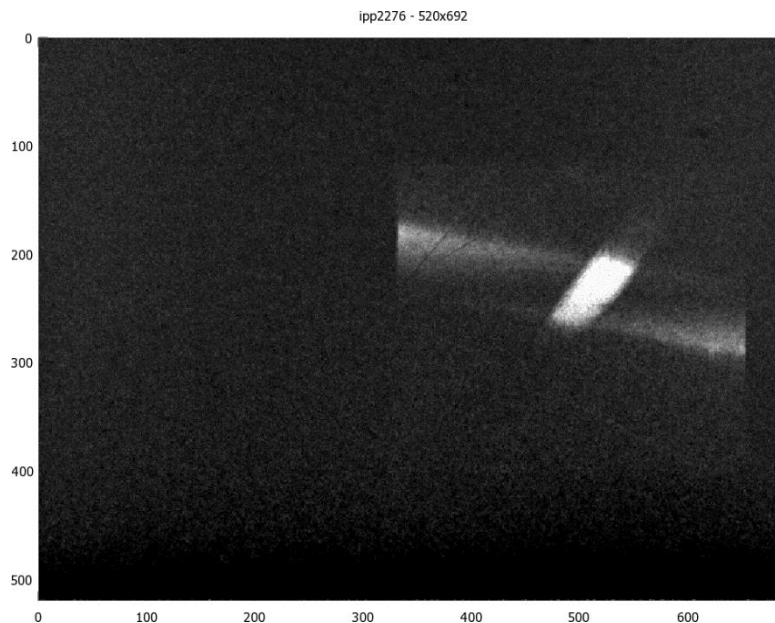
Fig. 4.2 *Raw imaging data (520 pixels by 692 pixels) of a single crystal of* DBO*/urea at χ = 45°, φ = 0°, T = 100 K with an intensity range of 3000 - 7000.*
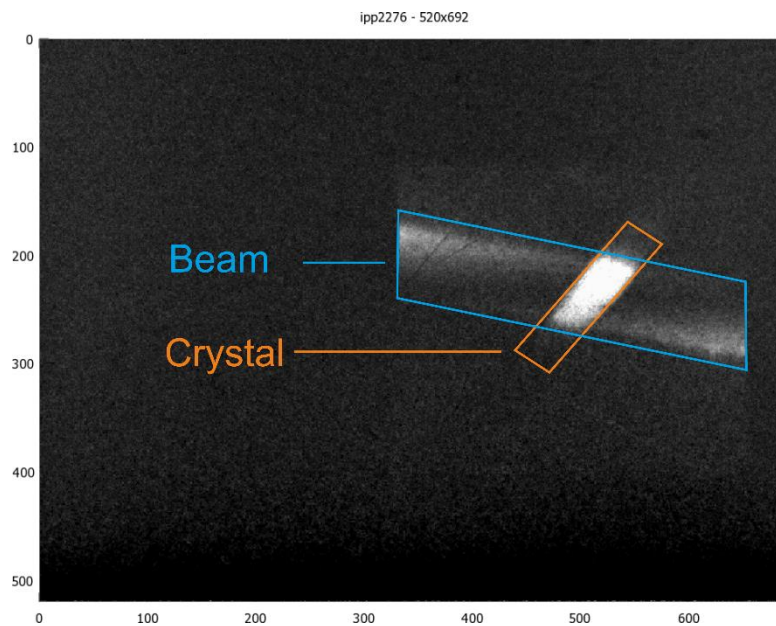
Fig. 4.3 *Annotated imaging data (520 pixels by 692 pixels) of a single crystal of DBO/urea at χ = 45°, φ = 0°, T = 100 K with an intensity range of 3000 - 7000.*

Fig. 4.4 *Raw imaging data (520 pixels by 692 pixels) of a single crystal of DBO/urea at χ = -5°, φ = 0°, T = 100 K with an intensity range of 3000 – 7000.*

This non-uniform background makes visual interpretation of the images more difficult, particularly in orientations where the crystal shows little birefringence (Fig. 4.4), but actually indicates superior polarization on the analyzer. In the experiment with the Si(555) analyzer horizontal polarization dominates the final image, in the experiment with the Ge(555) analyzer vertical polarization dominates the final image.[27]

4.3 Results

Fig. 4.5 shows the XBI data recorded in the high-temperature phase (270 K) for single crystals of 1,8-DBO/urea (Fig. 4.5a) and 1,10-DBD/urea (Fig. 4.5b) as a function of χ (with φ fixed). Each image shows the transmitted X-ray intensity (brightness scales proportionally with intensity) for a specific orientation of the crystal. For both 1,8-DBO/urea and 1,10-DBD/urea, the intensity varies significantly as a function of χ, with maximum brightness at $\chi \approx 45^{\circ}$ and minimum brightness at $\chi \approx 0^{\circ}$ and $\chi \approx 90^{\circ}$. Furthermore, the variation of transmitted X-ray intensity as a function of χ shows a sinusoidal dependence. It is clear from the XB images that, for each crystal orientation, the transmitted X-ray intensity is uniform across the entire crystal, indicating that the orientational properties of the C–Br bonds are the same across the whole crystal (i.e. the crystal comprises a single orientational domain).
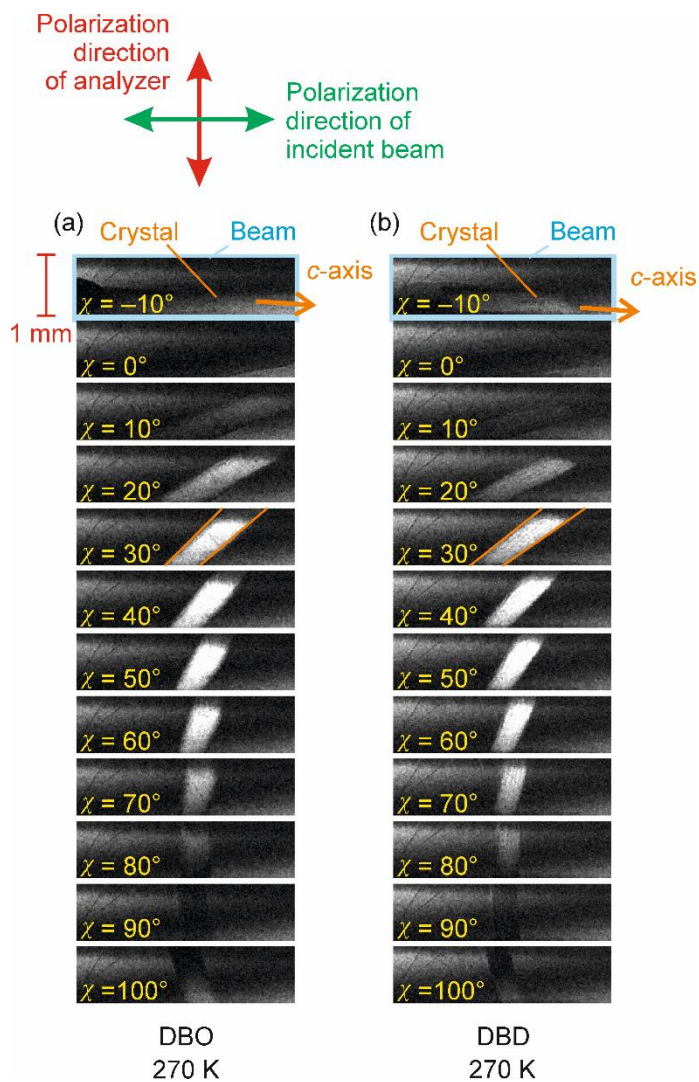
Fig. 4.5 *XBI data recorded at 270 K for a single crystal of a) 1,8-dibromooctane/urea and b) 1,10-dibromodecane/urea as a function of χ with φ fixed at 0°.*

Fig. 4.6 shows the XB images recorded in the high-temperature phase (270 K) for single crystals of 1,8-DBO/urea and 1,10-DBD/urea as a function of φ (with χ fixed at 45°, corresponding to maximum transmitted intensity in Fig. 2). No significant change in transmitted X-ray intensity is observed as a function of φ, suggesting that the orientational distribution of the C–Br bonds is not altered by rotation around the c-axis.
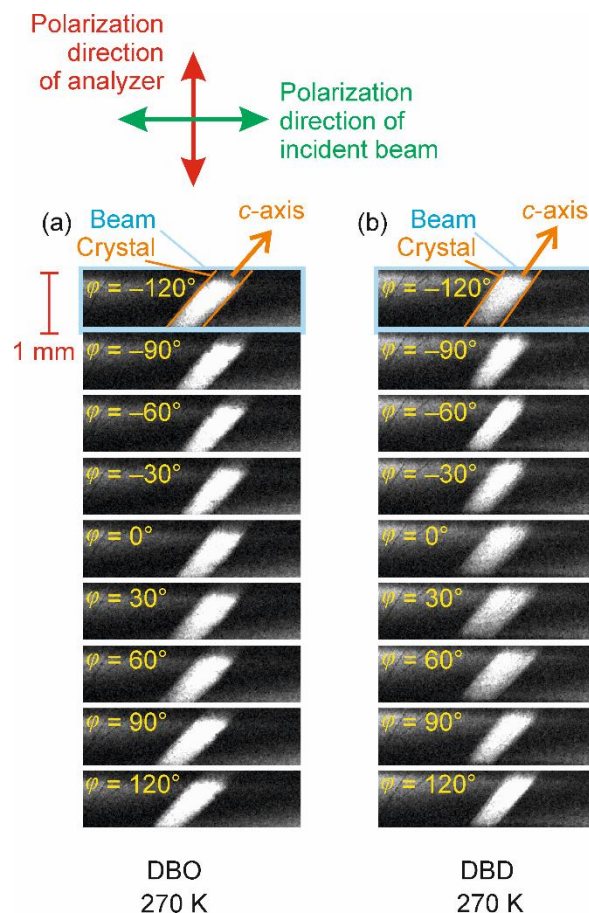
Fig. 4.6 *XBI data recorded at 270 K for a single crystal of a) 1,8-dibromooctane/urea and b) 1,10-dibromodecane/urea as a function of φ with χ fixed at 45°.*

The classical sinusoidal variation in transmitted X-ray intensity as a function of χ (Fig. 4.5) and the fact that the transmitted X-ray intensity is essentially independent of φ (Fig. 4.6) strongly resemble the behaviour of a uni-axial crystal in the polarizing optical microscope. As discussed above, in the case of X-ray birefringence studies at the bromine K-edge, the "X-ray optic axis" is dictated by the orientational properties of the C–Br bonds in the material. Indeed, the dependence of transmitted X-ray intensity on the crystal orientation angles χ and φ observed here is directly analogous to that reported previously[19] for a model material (the 1-bromoadamantane/thiourea inclusion

compound) in which all C–Br bonds are aligned parallel to each other, and with all C–Br bonds parallel to the crystal *c*-axis. By following this analogy, the X-ray birefringence behaviour observed for the 1,8-DBO/urea and 1,10-DBD/urea inclusion compounds may be interpreted in terms of a single "effective" C–Br bond orientation parallel to the tunnel axis (*c*-axis) of the urea host structure. As shown in Fig. 4.1, the spatial constraints imposed by the urea host tunnel are such that, for an α,ω-dibromoalkane guest molecule in the *all*-trans conformation and with the *trans* end-group conformation, the C–Br bond forms an angle of *ca*. 35.3° with respect to the tunnel axis. Clearly, the fact that the "X-ray optic axis" (i.e. the resultant C–Br bond vector) lies parallel to the tunnel axis for 1,8-DBO/urea and 1,10-DBD/urea in the high-temperature phase is a consequence of the reorientational dynamics of the guest molecules around the tunnel axis leading to a *time-averaged* projection of the C–Br bond vector along the tunnel axis.

More specifically, due to the rapid reorientation of the 1,8-DBO and 1,10-DBD guest molecules (and hence the C–Br bonds) about the tunnel axis in the high-temperature phase, the orientational distribution of each C–Br bond is described by a cone, with the cone axis parallel to the tunnel axis and with semi-angle of the cone equal to *ca*. 35.3°. The relative populations of the different orientations on the cone are not necessarily equal. However, at a given site on the tunnel axis, the local site symmetry experienced by the guest molecule due to its interaction with the host structure is described by a potential with approximately 6-fold rotational symmetry, and hence the distribution of populations of the orientations of the C–Br vectors on the cone must exhibit approximate 6-fold symmetry. For this orientational distribution, the resultant C−Br bond vector is directed parallel to the tunnel axis, representing the effective (time-averaged) C–Br bond orientation that defines the "X-ray optic axis" for the X-ray birefringence phenomenon. As a consequence, both 1,8-DBO/urea and 1,10-DBD/urea exhibit classical uni-axial behaviour, with sinusoidal dependence of transmitted X-ray intensity on crystal

orientation angle χ and essentially zero dependence of transmitted X-ray intensity on crystal orientation angle φ.

Across the phase transitions we see no obvious changes in XBI behaviour (Fig. 4.7) and plots of extracted intensity only also show little difference above and below the phase transition temperature. In long experiments and repeated scans we do see a slight diminishment of signal but we attribute that to sample degradation.
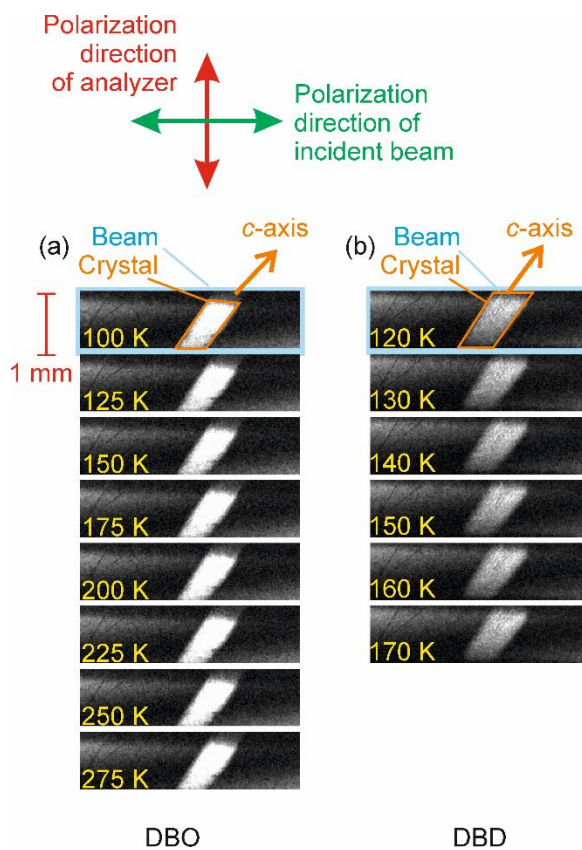
Fig. 4.7 *XBI data recorded at for a single crystal of a) 1,8-dibromooctane/urea and b) 1,10-dibromodecane/urea as a function of temperature with χ fixed at 45° and φ fixed at 0°. The phase transition temperatures are 157 K for 1,8-DBO/urea and 140 K for 1,10-DBD/urea.*

We now consider the orientational properties in the low-temperature phase. Fig. 4.8 and Fig 4.9 show XB images recorded at 100 K for single crystals of 1,8-DBO/urea and 1,10-DBD/urea as a function of χ (with φ fixed at 0°) and as a function of φ (with χ

fixed at 45°). For both materials, the X-ray birefringence behaviour in the low-temperature phase is essentially identical to that for the high-temperature phase, with the transmitted X-ray intensity varying in a sinusoidal manner as a function of crystal orientation angle χ and exhibiting essentially zero dependence on crystal orientation angle φ. Thus, in spite of the significant change in the overall symmetry of the urea host structure at the phase transition, the effective (time-averaged) C–Br bond orientation defining the "X-ray optic axis" for X-ray birefringence remains parallel to the tunnel axis. Furthermore, as the transmitted X-ray intensity remains uniform across the entire crystal for all orientations of the crystal, we may deduce that the orientational properties of the C–Br bonds are spatially uniform in the low-temperature phase, consistent with the existence of a single orientational domain across the entire crystal as in the high-temperature phase.
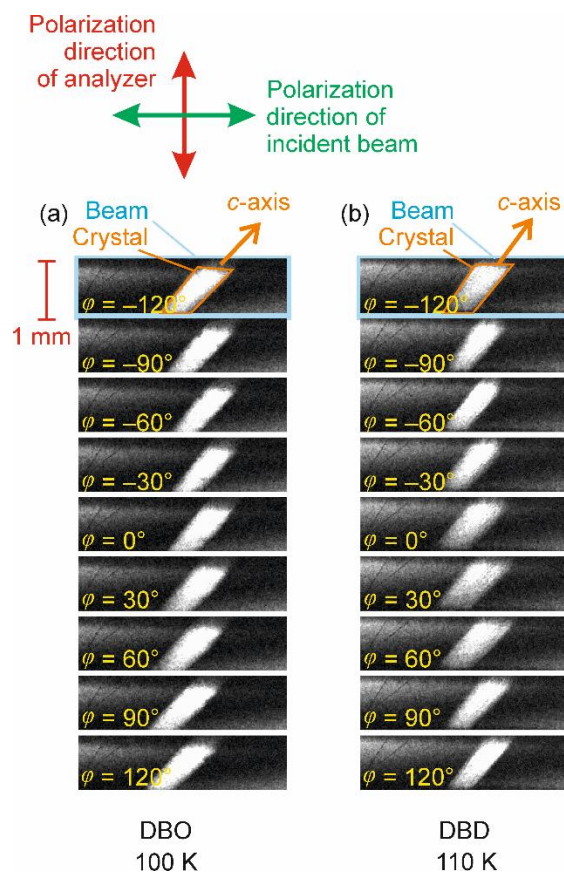
Fig. 4.8 *XBI data recorded at ~100 K for a single crystal of a) 1,8-dibromooctane/urea and b) 1,10-dibromodecane/urea as a function of χ with φ fixed at 0°.*
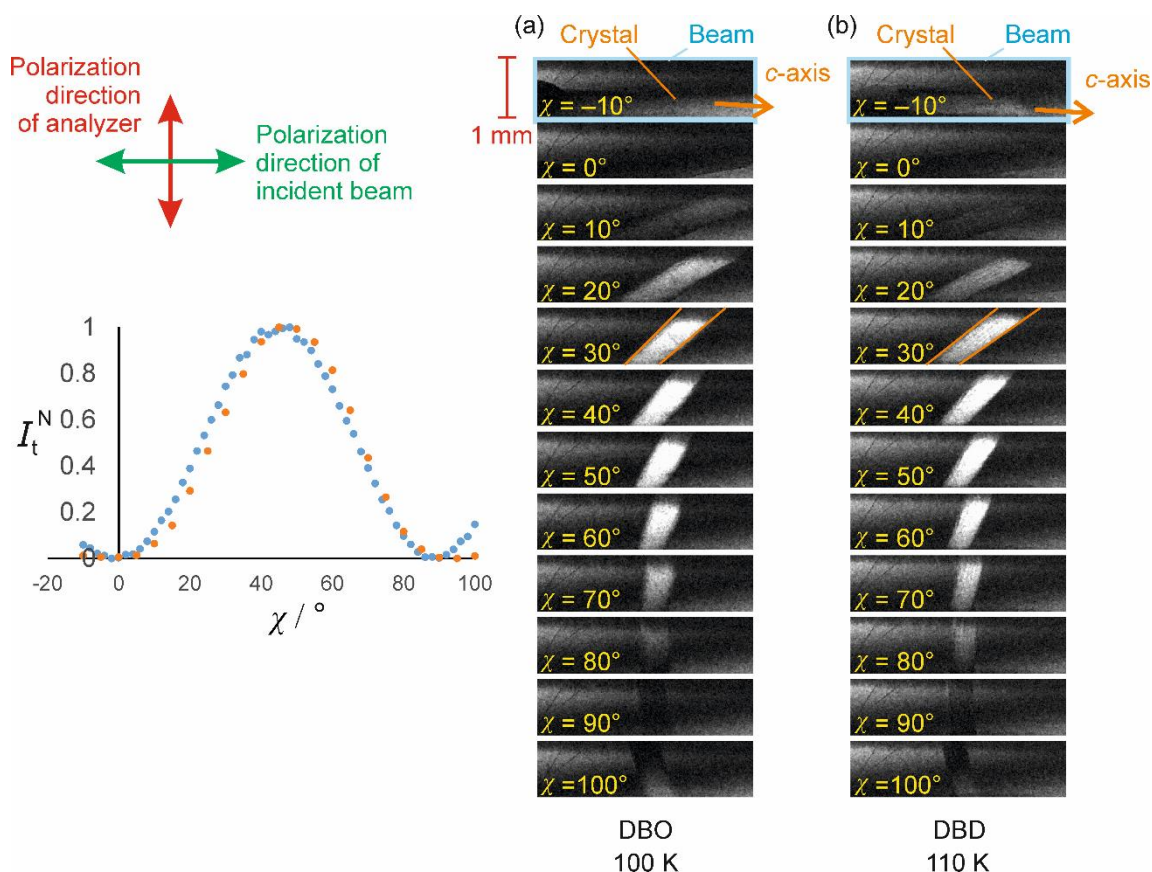
Fig. 4.9 *XBI data and extracted intensities recorded at ~100 K for a single crystal of a) 1,8-dibromooctane/urea and b) 1,10-dibromodecane/urea as a function of φ with χ fixed at 45°. Extracted intensities are also shown. For the normalized transmitted intensity plot DBO is blue and DBD is orange*

As discussed in the introduction, results from solid-state ^{2}H NMR lineshape analysis[14] suggest that no significant abrupt change in the dynamics of the guest molecules occurs on entering the low-temperature phase, and the guest molecules in the low-temperature phase still undergo uni-axial molecular reorientation. Thus, the "effective" (motionally averaged) C–Br bond orientation in the low-temperature phase is identical to that in the high-temperature phase, consistent with the results observed in the XBI data. Results from solid-state ^{2}H NMR lineshape analysis[14] indicate that the guest molecules in 1,10-DBD/urea still undergo reorientational dynamics on a timescale shorter

than 10^{-3} s at 140 K, and do not rule out the possibility that the 1,10-DBD guest molecules may still be dynamic at 110 K (but with timescale of motion longer than 10^{-3} s). Under these circumstances, the (slow) dynamics of the guest molecules at the temperature (110 K) of the XBI experiments would be such that, within the timescale of the XBI measurement, the resultant direction of the ensemble of C–Br bond vectors is projected along the tunnel axis, as in the high-temperature phase.

However, if the reorientational dynamics of the guest molecules about the tunnel axis have actually become "frozen-out" by 110 K, the observed X-ray birefringence behaviour may be explained by a situation of static disorder of the guest molecules, such that the resultant X-ray birefringence from the static orientational distribution still results in an effective C–Br bond oriented along the tunnel direction, representing the resultant of the *space-average* of the C−Br bond orientations averaged over all regions of the crystal.[28]

4.4 Conclusion

The XBI results for the 1,8-DBO/urea and 1,10-DBD/urea inclusion compounds in the high-temperature phase indicate clearly that, for a dynamic system, the effective "X-ray optic axis" for the X-ray birefringence phenomenon is the *time-averaged* resultant of the orientational distribution of the C–Br bonds. The observed XBI behaviour on entering the low-temperature phase is fully consistent with the conclusion from previous solid-state ^{2}H NMR studies that there is no significant discontinuity in the dynamic properties of the guest molecules on entering the low-temperature phase, as the XBI data are again explained by an effective "X-ray optic axis" aligned parallel to the tunnel axis. However, the possibility that this resultant C–Br bond vector represents the space-average of a static orientational distribution (as opposed to the time-average of a dynamic orientational distribution) cannot be ruled out, as the rate of motion (if it occurs) is known to be slower than the slowest rate that can be detected by the ^{2}H NMR technique.

4.5 References

[1]   K. D. M. Harris, *J. Solid State Chem.,* **1993**, 106, 83-98.
[2]   K. D. M. Harris, *J. Mol. Struct.,* **1996**, 374, 241-250.
[3]   K. D. M. Harris, *Chem. Soc. Rev.,* **1997**, 26, 279-289.
[4]   F. Guillaume, *J. Chim. Phys. (Paris),* **1999**, 96, 1295-1315(h).
[5]   M. D. Hollingsworth, *Science,* **2002**, 295, 2410-2413.
[6]   K. D. M. Harris, *Supramol. Chem.,* **2007**, 19, 47-53.
[7]   A. E. Smith, *Acta Crystallogr*., **1952**, 5, 224.
[8]   K. D. M. Harris, J. M. Thomas, *J. Chem. Soc. Faraday Trans.,* **1990**, 86, 2985.
[9]   A. R. George, K. D. M. Harris, *J. Mol. Graphics,* **1995**, 13, 138.
[10]   A. J. O. Rennie, K. D. M. Harris, *Proc. R. Soc., London Ser. A,* **1990**, 430, 615.
[11]   D. Schmicker, S. van Smaalen, J. L. de Boer, C. Haas, K. D. M. Harris, *Phys. Rev. Lett.,* **1995**, 74, 734.
[12]   R. Lefort, J. Etrillard, B. Toudic, F. Guillaume, T. Breczewski, *Europhys. Lett.,* **1998**, 43, 546.
[13]   K. D. M. Harris, S. P. Smart, M. D. Hollingsworth, *J. Chem. Soc. Faraday Trans.,* **1991**, 87, 3423-3429.
[14]   A. E. Aliev, S. P. Smart, I. J. Shannon, K. D. M. Harris, *J. Chem. Soc. Faraday Trans.,* **1996**, 92, 2179-2185.
[15]   L. Yeo, K. D. M. Harris, *Acta Crystallogr.,* **1997**, B53, 822-830.
[16]   J. D. Bell, R. E. Richards, *Trans. Faraday Soc*., **1969**, 65, 2529-2536.
[17]   F. Guillaume, S. P. Smart, K. D. M. Harris, A. J. Dianoux, *J. Phys.-Condens. Mat.,* **1994**, 6, 2169-2184.
[18]   S. P. Smart, A. El Baghdadi, F. Guillaume, K. D. M. Harris, *J. Chem. Soc. Faraday Trans.,* **1994**, 90, 1313-1322.
[19]   B. A. Palmer, A. Morte-Ródenas, B. M. Kariuki, K. D. M. Harris, S. P. Collins, *J. Phys. Chem. Lett*., **2011**, 2, 2346-2351.
[20]   B. A. Palmer, G. R. Edwards-Gau, A. Morte-Ródenas, B. M. Kariuki, G. K. Lim, K. D. M. Harris, I. P. Dolbnya, S. P. Collins, *J. Phys. Chem. Lett*., **2012**, 3, 3216-3222.
[21]   B. A. Collins et al., *Nature Mater.,* **2012**, 11, 536-543.
[22]   Y. Joly, S. P. Collins, S. Grenier, H. C. N. Tolentino, M. De Santis, *Phys. Rev. B*, **2012**, 86, 220101(R).
[23]   S. P. Collins, I. Dolbnya, B. A. Palmer, G. R. Edwards-Gau, A. Morte-Ródenas, B. M. Kariuki, G. K. Lim, K. D. M. Harris, Y. Joly, *J. Phys.: Conf. Ser.,* **2013**, 425, 132015.

[24]   B. A. Palmer, B. M. Kariuki, A. Morte-Ródenas, K. D. M. Harris, *Cryst. Growth Des.,* **2012**, 12, 577-582.

[25]   B. A. Palmer, G. R. Edwards-Gau, B. M. Kariuki, K. D. M. Harris, I. P. Dolbnya, S. P. Collins, *Science,* **2014**, 344, 1013-1016

[26]   K. J. S. Sawhney et al., *AIP Conference Proceedings*, **2010**, 1234, 387-390.

[27]   J. P. Sutter, I. P. Dolbnya, S. P. Collins, K. D. M. Harris, G. R. Edwards-Gau, B. A. Palmer, *J. Appl. Phys.*, **2015**, 117, 164902

[28]   B. A. Palmer, G. R. Edwards-Gau, B. M. Kariuki, K. D. M. Harris, I. P. Dolbnya, S. P. Collins, J. P. Sutter, *J. Phys. Chem. Lett.*, **2015**, 6, 561-567

Chapter 5 – *In-Situ* NMR Crystallization of Urea Inclusion Compounds

5.1 Introduction

Urea inclusion compounds are known to preferentially include different guests, based largely on the length of the guest molecule, but the exact process is poorly understood. Is it a kinetic process, where certain guests are included earlier in the crystallisation process or is it a thermodynamic process where energetically unfavourable guests are gradually replaced by favourable guests? Guest exchange processes have been observed post-crystallization[1] but it is still not entirely clear what is happening during crystallization.

To investigate the crystallization of UICs, we decided to employ an *in-situ* NMR technique[2-4]. By watching the decrease of solution signal and the increase of solid signal as crystallization occurred, we hoped to better understand the process and, in turn, better understand the materials themselves. In these experiments, we decided to use a combination of guests with significantly different NMR signals, so we could easily see whether a particular guest was being included earlier or more substantially.

After considering the possible guest molecules we decided to employ combinations of alkanes and α,ω-dibromoalkanes as both guests are relatively easy to dissolve and solid-state NMR of mixed guest α,ω-dibromoalkane/alkane UICs has shown that a methyl next to a bromoalkane neighbour gives a different chemical shift than a methyl next to an alkane neighbour (Fig. 5.1). This sensitivity to the neighbouring molecule allows us to judge the ordering within the crystal, i.e., in a 50:50 α,ω-dibromoalkane/alkane mixed-guest crystal a high proportion of $-CH_3\cdots CH_3-$ signals tells us that we have large regions of just the alkane guests but a high proportion of $-CH_3\cdots BrCH_2-$ signals indicates an alternating pattern of guest molecules. α,ω-Dichloroalkane guests were considered but these show little splitting by neighbour environment so it was thought the α,ω-dibromoalkane/alkane combination would yield

more information. α,ω-diiodoalkane guests were considered as the α,ω-diidodoalkane/Alkane combination gives superior end-group neighbour splitting in SS NMR but the poor solubility of iodoalkanes made them an unfavourable choice for the first experiments. Note that we are primarily interested in peaks at the ends of the chain because the peaks in the middle of the chain possess very similar chemical shifts and are less distinctive.
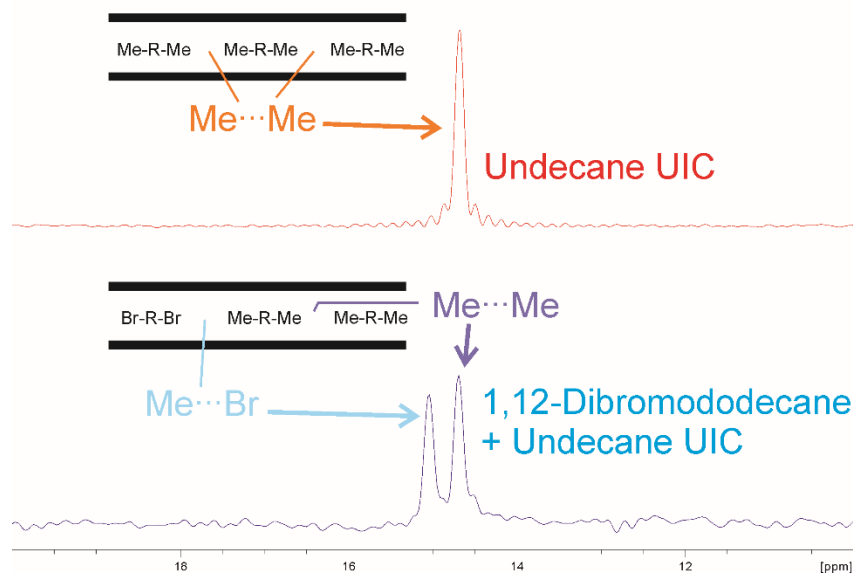
Fig. 5.1 Demonstration of chemical shift being influenced by the neighbouring guest molecule within the UIC tunnel. The methyl group at the end of a molecule of undecane gives a single peak in a single guest undecane/urea IC, but gives a split double peak in a mixed guest 1,12-dibromododecane + undecane /urea inclusion compound. The peak located in both samples is identified as the Me···Me signal and the additional peak which only occurs in the mixed guest UIC is identified as the Me···Br signal.

Fig 5.2 shows the end of chain carbon peak positions and splitting observations for urea inclusion compounds of alkanes, α,ω-dihaloalkanes and haloundecanes for chain lengths of 12 carbon equivalents (i.e., dodecane, 1,10-dihalodecanes and haloundecanes). This chart shows: 1) that carbon adjacent to iodine is frequently split by neighbour environment (-CH_2I···I gives a different chemical shift than -CH_2I···Cl, -CH_2I···Br and -CH_2I···CH_3), 2) that the methyl carbon is split by bromine and iodine neighbours (-CH_3···CH_3 gives a different chemical shift than -CH_3···Br, -CH_3···I), 3) that the carbon

adjacent to iodine can be split by methyl neighbours (-$\underline{C}H_2Cl\cdots Cl$ gives a different chemical shift than -$\underline{C}H_2Cl\cdots CH_3$)
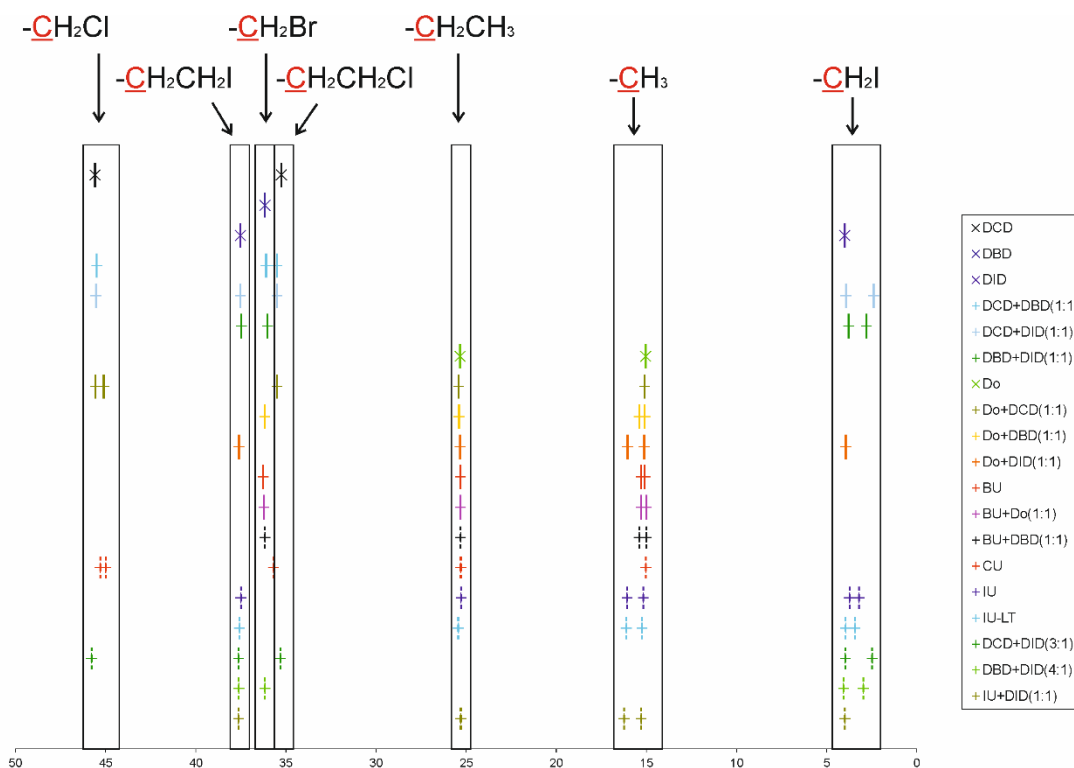
Fig. 5.2 *^{13}C SSNMR peak positions for the diagnostic guest peaks (the position at the end of the chain and the position adjacent to it) of 1,10-Dichlorodecane (DCD), 1,10-Dibromodecane (DBD), 1,10-Diiododecane (DID), Dodecane (Do), 1-Chloroundecane (CU), 1-Iodoundecane (IU) and combinations thereof. Data acquired on the 300 MHz at Cardiff University with MAS at 6 KHz and CP signal enhancement, and referenced to the urea peak at 164ppm. In some cases multiple peaks are assigned to a single carbon atom due to peak splitting from different neighbour environments (e.g. -$CH_2I\cdots ICH_2$- gives a different chemical shift than -$CH_2I\cdots CH_3$-.) The remaining carbon positions in each guest chain give chemical shifts in 30-35ppm range and in mixed guest UICs it was difficult and impractical to unambiguously assign a peak to one guest.*

For our *in-situ* NMR experiments, we elected to use different chain lengths so that we could create combinations with different guest preferences but still our decane SS NMR experiments informed us of which combinations gave rise to splitting effects. Ultimately we decided to use combinations of 1,8-dibromooctane,

1,12-dibromododecane, undecane and tetradecane, and the physical properties of these guest molecules are listed in table 1.

	Melting point / °C	Density / g/mL at 25 °C	Molecular weight
1,8-Dibromooctane	12-16	1.477	272.02
1,12-Dibromododecane	38-42		328.13
Undecane	−26	0.74	156.31
Tetradecane	5.5	0.762	198.39
Methanol	−98	0.791	32.04

Table 1 *Table showing the physical properties of the selected guest molecules and the solvent.*

5.2 Experimental

Our *in-situ* NMR experiments at the UK 850 MHz facility at the university of Warwick have looked at the crystallization of three mixed guest urea inclusion compounds (UIC).

- Mixture 1) 1,8-Dibromooctane (DBO) + Undecane (UD) UIC. This gives us a combination where both guest molecules have similar lengths.

- Mixture 2) 1,8-Dibromooctane (DBO) + Tetradecane (TD) UIC. This gives us a combination where the alkane guest molecule is significantly longer than the bromoalkane.

- Mixture 3) 1,12-Dibromododecane (DBDD) + Undecane (UD) UIC. This gives us a combination where the bromoalkane guest molecule is significantly longer than the alkane.

In each case, an NMR sample of known guest composition was produced by dissolving premade UICs where the guest proportions had been determined by solution-state NMR. In each case, approximately 10 mg of UIC was dissolved in approximately 30 mg of methanol, in order to get as much sample as possible whilst still minimizing the

risks of leaks. Dissolving a known UIC material means we already know the relative quantities of each guest in the sample and new NMR samples can be produced quickly and easily. Conversely, producing UICs directly by weighing out the starting materials proved difficult due to the small scale (as little as 1 mg for certain components) and the need to balance the ratios of four different components. Stock solutions were also considered but would only be effective if maintained at high temperature.

The three mixtures were chosen to give a combination where both guests have similar lengths (Mixture 1), a combination where the alkane is significantly longer (Mixture 2) and a combination where the α,ω-dihaloalkane is significantly longer (Mixture 3). By using these different chain lengths we sought to alter the relative preference for each type of guest and see what effect that had on the crystallization process. Relatively short guests were chosen to give a higher proportion of end-chain carbons.

Initial preparation of these UIC materials was carried out by dissolving urea (0.3 g, 5 mmol) and the two guests (0.46 mmol of each) in methanol (4 ml) at 55°C. The resulting solution was incubated at 55°C for 1hr, cooled to 25°C at a rate of 0.03°C/min and then left to stand for 24 hours. This process yielded small colourless needle-shaped crystals which were harvested and washed with 2,2,4-trimethylpentane. Production of a UIC was confirmed using PXRD as a fingerprinting technique and the guest composition within the crystals was determined using solution state NMR (the 50:50 ratio of starting guest did not give a 50:50 ratio inside the harvested crystal). PXRD was also performed on material recovered from the sample rotors and no differences were observed.

Methanol was chosen as the NMR solvent because it is the standard solvent used in UIC preparation. The typical process for crystallizing a α,ω-dihaloalkane/urea inclusion compound also uses a small amount of 2-methyl-2-butanol as a co-solvent to help dissolve the guest, but we decided to use pure methanol because we thought the complications of adding a co-solvent outweighed the advantage of better solvation. As it transpired we did observe some undissolved guest as a separate liquid phase (i.e. we exceeded the solubility limit of the solvent), but trying to eliminate this liquid phase resulted in much weaker

solution and solid signals so disrupted our data quality. Therefore despite our attempts to create a two-phase system much of the data in this chapter has a solid phase (guest inside a solid urea inclusion compound), a solution phase (guest dissolved in methanol) and a liquid phase (pure liquid guest).

Samples on the 850 MHz spectrometer were spun at 12 KHz MAS using the HX probe and using the calibration curve to attain the correct temperature at that spinning speed. Some experiments were also performed at 8 KHz and 4 KHz to gauge whether the spinning was having any effect on the crystallisation process, but no changes were observed. Alanine was used for referencing, with the carboxylate set to 178 ppm.

Samples were held at high temperature for 1 hr prior to cooling and each mixed guest combination was subject to a slow cool experiment (cooling from 50 °C to 20 °C over 7 hours or 11 hours) and a fast cool experiment (cooling from 50 °C to 20 °C over approximately 5 minutes). Data acquisition continued for a long time after reaching 20 °C with the aim of investigating possible changes post-crystallization (e.g. guest exchange processes could alter the guest composition of the solid even after crystallization had finished).

In most cases, the slow and fast crystallizations were performed on the same sample (i.e., a sample was heated and cooled quickly then reheated and cooled slowly) but in the case of DBO/UD mixture a separate sample was made using the same prepared materials. Details of the rotor sample are as follows.

- For mixture 1 the fast and slow crystallization experiments were performed on NMR samples made from the same UIC crystals. The slow cool sample consisted of 9.2 mg UIC (55% DBO, 45% UD) in 29.8 mg methanol. The fast cool sample consisted of 9.2 mg UIC (55% DBO, 45% UD) in 29.4 mg methanol.

- For mixture 2 the fast and slow crystallization experiments were performed on the same NMR sample. This sample consisted of 9.8 mg UIC (34% DBO, 66% TD) in 29.8 mg methanol.

- For mixture 3 the fast and slow crystallization experiments were performed on the same NMR sample. This sample consisted of 9.1 mg UIC (57% DBDD, 43% UD) in 30.1 mg methanol.

Our preliminary work alternated between (High-power Proton DECoupled) HPDEC and Cross-Polarization (CP) experiments[5-8] to get solution and solid-state information, but we attained satisfactory solid signal on the HPDEC experiment, so for the time-resolved experiments reported, we utilized HPDEC exclusively. By using HPDEC for both solid and solution information we were able to achieve much better time resolution than alternating between two experiments. CP was still employed on occasion, largely to clarify which signals were arising from the solid and which signals were arising from solution. Solid UIC samples were also run before the crystallization experiments

For each crystallization experiment, the HX probe was tuned when the sample was at low temperature and left that way for the course of the crystallization. This means we have sub-optimal tuning whilst at high temperature but it is the only way to perform the experiment - continually retuning the probe every couple of minutes for 17 hours is simply not practical. During the data analysis baseline corrections were performed by identifying the background slope in the absence of any peaks then subtracting this from the data. Our longer crystallization experiments show a drift in peak position (Fig. 5.3 and Fig. 5.4) which we attribute to the gradual cooling of the shimming magnets. During signal integration, this peak drift has been accommodated by shifting the integration zone based on the moving position of the peak.
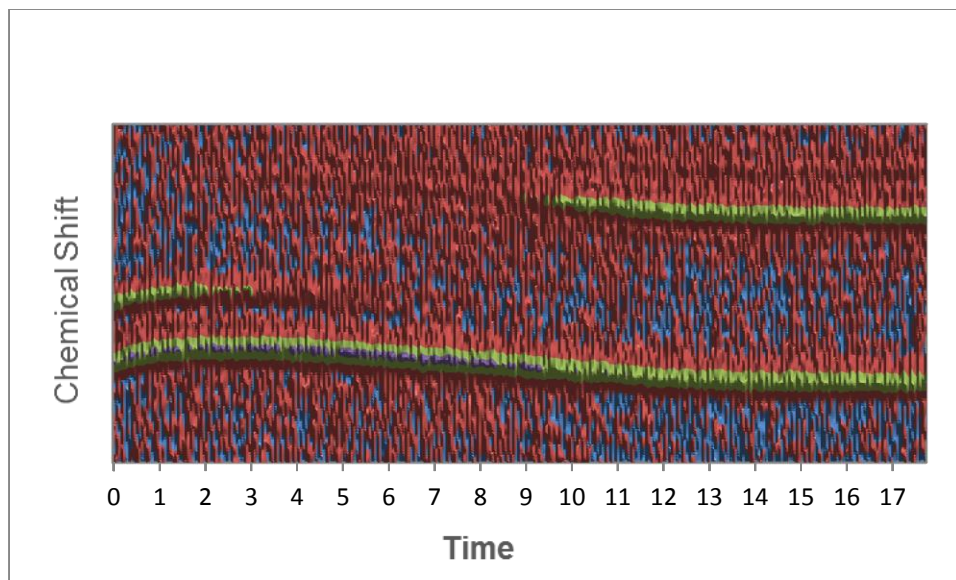
Fig. 5.3 *Schematic showing the drift in position of the methyl peaks in the DBO+UD/urea slow crystallization.*
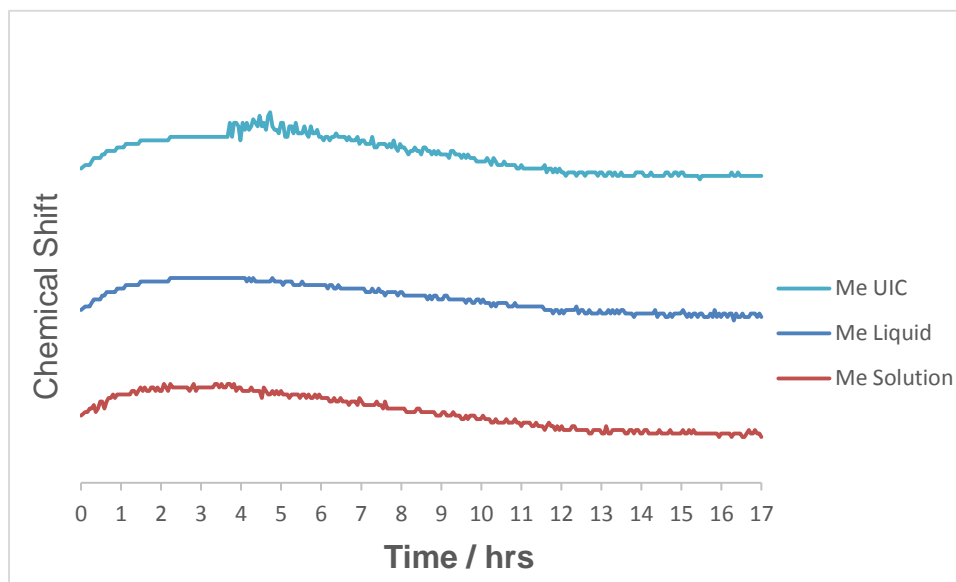
Fig. 5.4 *Schematic showing the drift in position of the methyl peaks in the DBO+UD/urea slow crystallization. This graph shows the anchor point that the integration zone was based on.*

5.3 Solid-State NMR of Solid Urea Inclusion Compounds

Patterns are shown for solid UICs on the 850 MHz NMR spectrometer. Figures 5.5-5.9 show single guest urea inclusion compounds with undecane, tetradecane, 1,8-dibromooctane and 1,12-dibromododecane. Fig. 5.10 shows a mixed guest UIC with 1,8-dibromooctane+undecane. Fig. 5.11 shows a mixed guest UIC with 1,8-dibromooctane+tetradecane. Fig. 5.12 shows a mixed guest UIC with 1,12-dibromododecane+undecane.
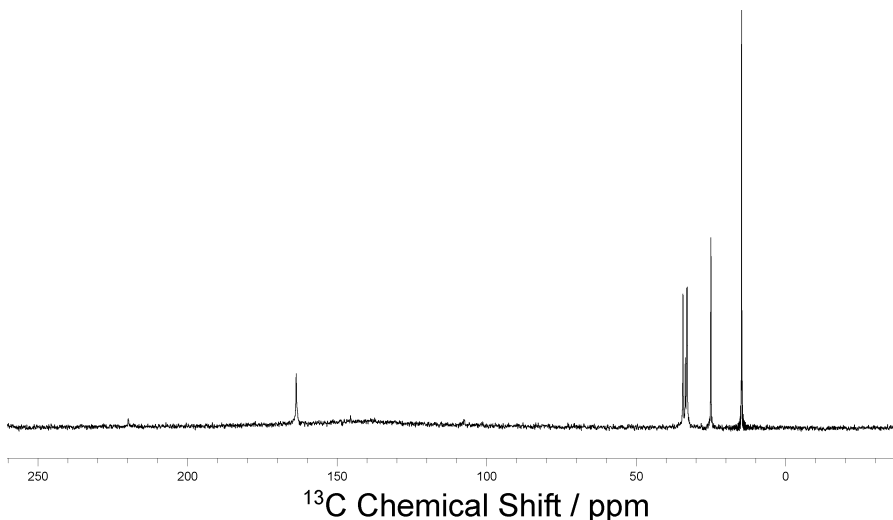
Fig. 5.5 *HPDEC ^{13}C spectrum from 260ppm to -39ppm of solid undecane/urea. The peak at 163.7ppm is urea in the UIC and the peaks in the 40-10ppm range arise due to the guest. For subsequent spectra we will be focussing on this 40-10ppm region. Note that CP offers little benefit for the guest peaks but a considerable benefit for the urea peak.*
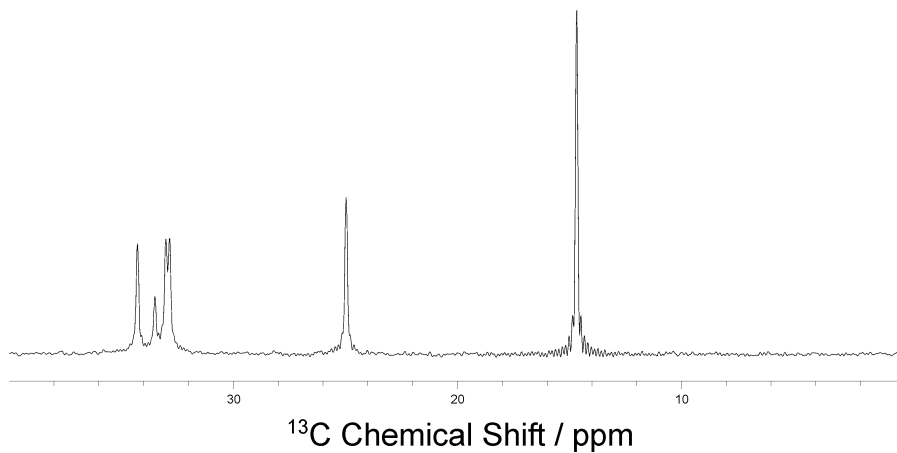
Fig. 5.6 *HPDEC ^{13}C spectrum from 40ppm to 10ppm of solid undecane/urea. The methyl carbon gives a signal at 15ppm, the second carbon in the chain gives a peak at 25 ppm and the carbons further towards the middle of the chain give peaks in the 35-30ppm range.*
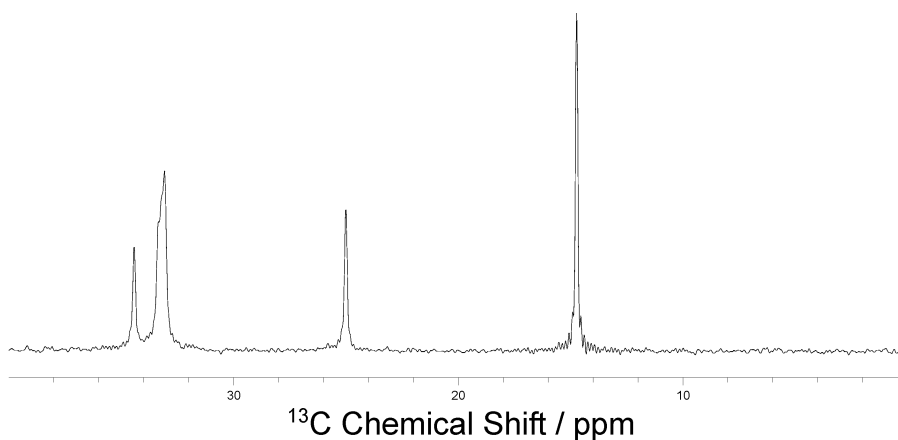
Fig. 5.7 *HPDEC ^{13}C spectrum from 40ppm to 10ppm of solid tetradecane/urea. The methyl carbon gives a signal at 15ppm, the second carbon in the chain gives a peak at 25 ppm and the carbons further towards the middle of the chain give peaks in the 35-30ppm range.*

13C Chemical Shift / ppm
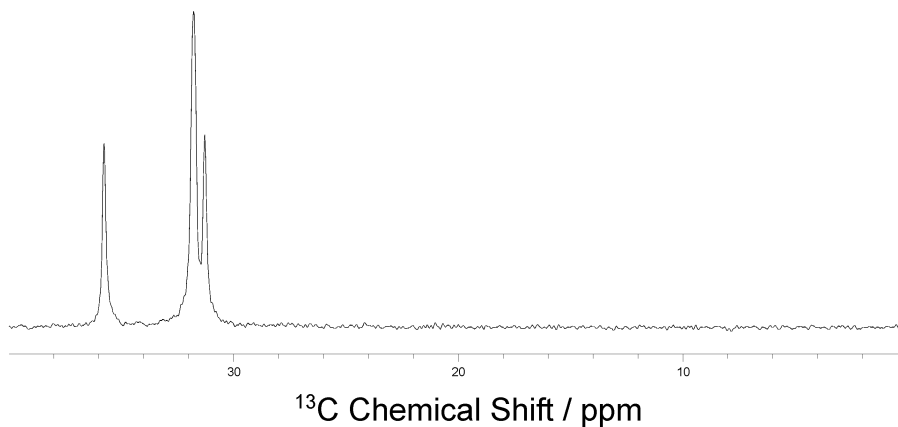
Fig. 5.8 HPDEC ^{13}C *spectrum from 40ppm to 10ppm of solid 1,8-dibromooctane/urea. The carbon bonded to bromine give a peak at 36ppm and the carbons further towards the middle of the chain give peaks in the 35-30ppm range.*

13C Chemical Shift / ppm
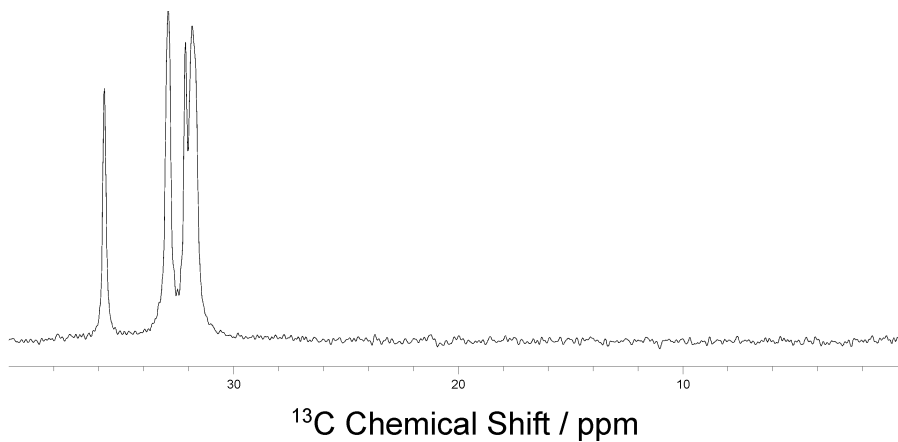
Fig. 5.9 HPDEC ^{13}C *spectrum from 40ppm to 10ppm of solid 1,12-dibromododecane/urea. The carbon bonded to bromine gives a peak at 36ppm and the carbons further towards the middle of the chain give peaks in the 35-30ppm range*

13C Chemical Shift / ppm
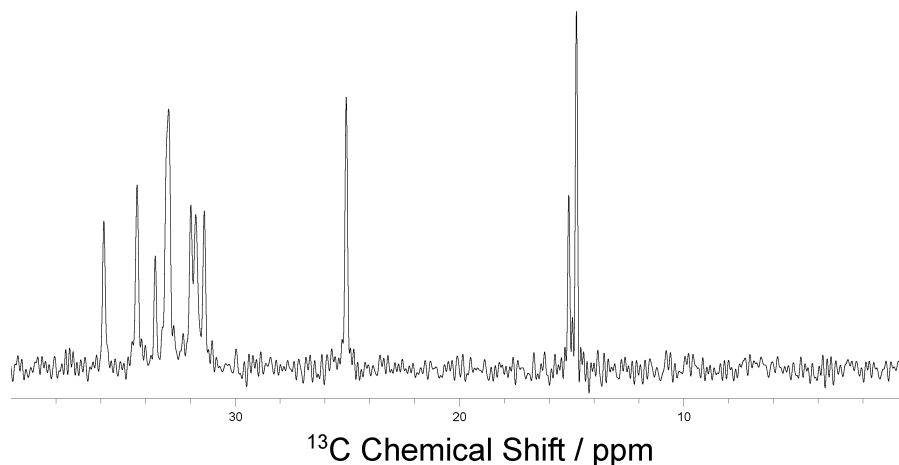
Fig. 5.10 *HPDEC ^{13}C spectrum from 40ppm to 10ppm of the solid mixed guest inclusion compound 1,8-dibromooctane+undecane/urea (55% DBO, 45% UD). The DBO carbon bonded to bromine gives a peak at 36ppm, the UD methyl carbon gives a signal at 15ppm (split in two), the second carbon in the UD chain gives a peak at 25 ppm and the carbons further towards the middle of both chains give peaks in the 35-30ppm range.*

13C Chemical Shift / ppm
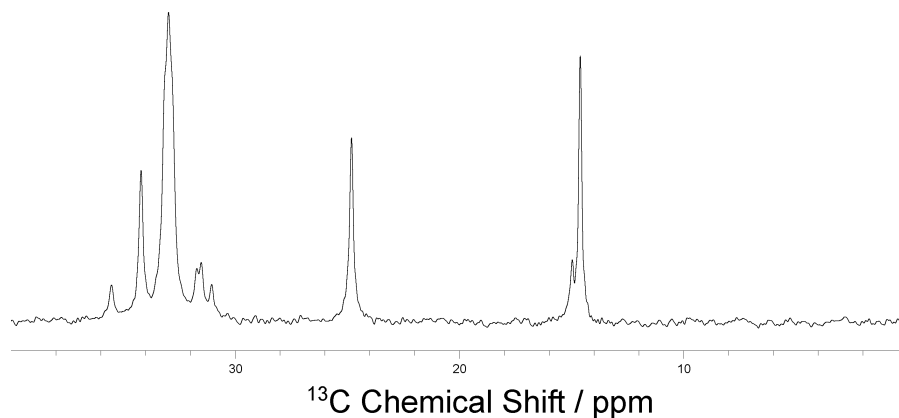
Fig. 5.11 *HPDEC ^{13}C spectrum from 40ppm to 10ppm of the solid mixed guest inclusion compound 1,8-dibromooctane+tetradecane/urea (34% DBO, 66% TD). The DBO carbon bonded to bromine gives a peak at 36ppm, the TD methyl carbon gives a signal at 15ppm (split in two), the second carbon in the TD chain gives a peak at 25 ppm and the carbons further towards the middle of both chains give peaks in the 35-30ppm range.*

^{13}C Chemical Shift / ppm
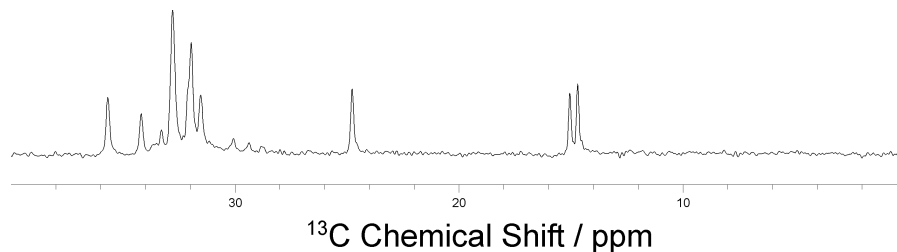
Fig. 5.12 *HPDEC ^{13}C spectrum from 40ppm to 10ppm of the solid mixed guest inclusion compound 1,12-dibromododecane+undecane/urea (57% DBDD, 43% UD). The DBDD carbon bonded to bromine gives a peak at 36ppm, the UD methyl carbon gives a signal at 15ppm (split in two), the second carbon in the UD chain gives a peak at 25 ppm and the carbons further towards the middle of both chains give peaks in the 35-30ppm range.*

5.4. *In-Situ* NMR of Urea Inclusion Compound Crystallization

Mixed-guest UICs were prepared then dissolved as defined in section 5.2. The guest molecules show high mobility inside the UIC structure so better solid signal is achieved with HPDEC experiments than with CP experiments. CP experiments were performed to confirm which signals were arising from the solid.

The full spectrum shows a peak at 164 ppm corresponding to urea, a peak at 50 ppm corresponding to methanol and a large number of peaks in the 40-10 ppm region corresponding to the guest molecules. As we are chiefly interested in the guest molecules we have focused on this region.

5.4.1 Slow crystallization of DBO (55%) & UD (45%) / Urea in Methanol

Over the course of our slow cooling experiment (Fig. 5.13) we see the disappearance of the liquid UD signal followed by the appearance of solid signal from UD in the UIC. We are unable to see signal from DBO in the solid, but the minor splitting of the UD methyl peak shows that some DBO must be present inside the UIC and we also see strong signal from DBO in solution (Fig 5.13). Note an unknown peak occurs at 26 ppm.
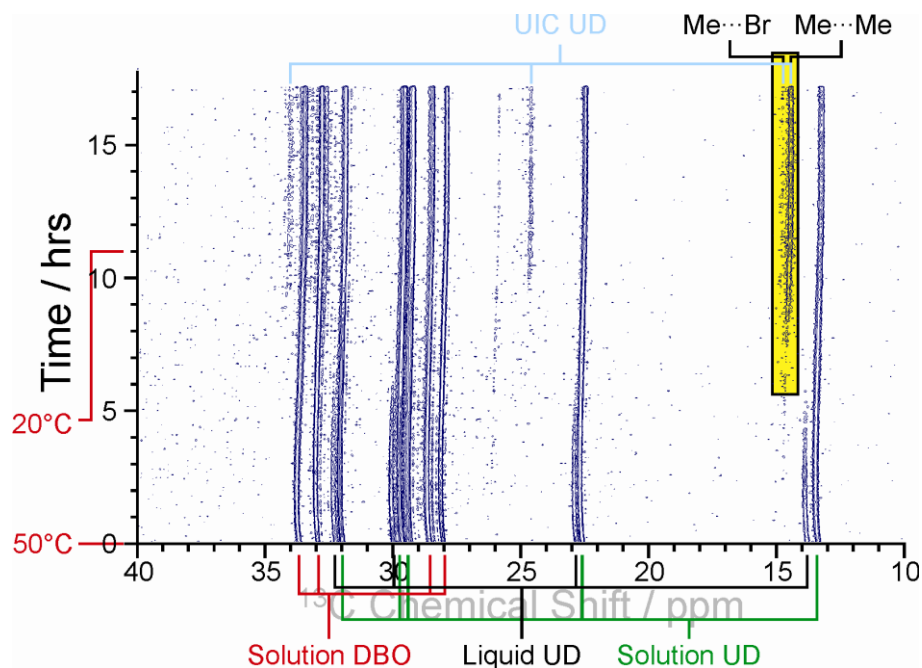
Fig. 5.13 *Time resolved HPDEC ^{13}C spectrum from 40ppm to 10ppm of the slow crystallization of 1,8-dibromooctane+undecane/urea (55% DBO, 45% UD) in methanol. Only positive intensity is shown. Chemical shift (ppm) occupies the horizontal axis, time (hrs) occupies the vertical axis and the cooling period has been denoted on this axis. Liquid and solution peaks are labelled at the bottom of the spectrum, solid peaks are labelled at the top of the spectrum. The splitting of the methyl peak by neighbour environment is highlighted in yellow.*

Summing many scans together after crystallization has finished allows us to assess the end point of the process (Fig. 5.14) whilst taking cross sections of the NMR spectra at different time intervals allows us to see how the NMR spectrum changes with time (Fig. 5.15 and Fig. 5.16). These cross sections clearly show the decay of the liquid UD methyl peak at 14 ppm followed by the emergence of the solid UD methyl peak at 15 ppm.
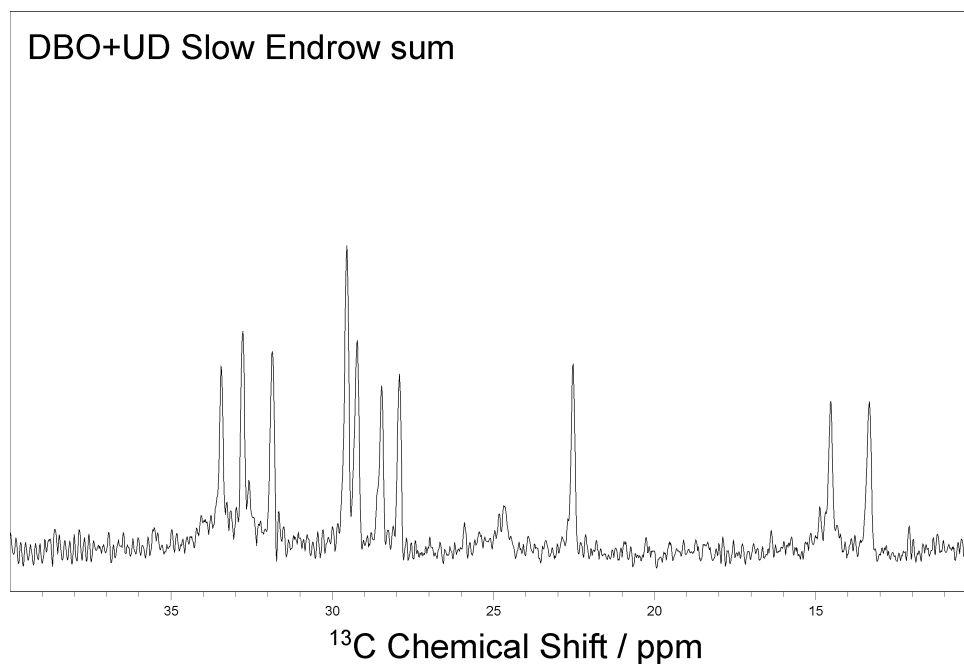
Fig. 5.14 *Sum of the last 100 rows of the of 40ppm to 10ppm range of the time resolved HPDEC ^{13}C spectrum from of the slow crystallization of 1,8-dibromooctane + undecane/urea (55% DBO, 45% UD) in methanol. This represents the end-point of the crystallization process.*
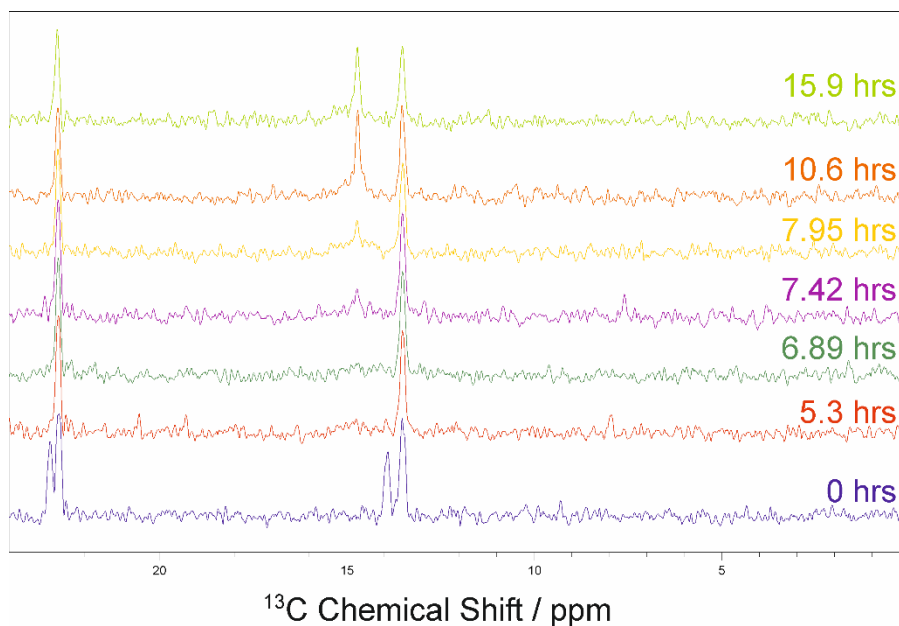
Fig. 5.15 *Intermittent cross sections of the time resolved HPDEC ^{13}C spectrum from 24ppm to 0ppm of the slow crystallization of 1,8-dibromooctane+undecane/urea (55% DBO, 45% UD) in methanol. Note the decay of the liquid undecane peaks and the emergence of the solid undecane peaks. Ten time points have been binned together for each cross section.*
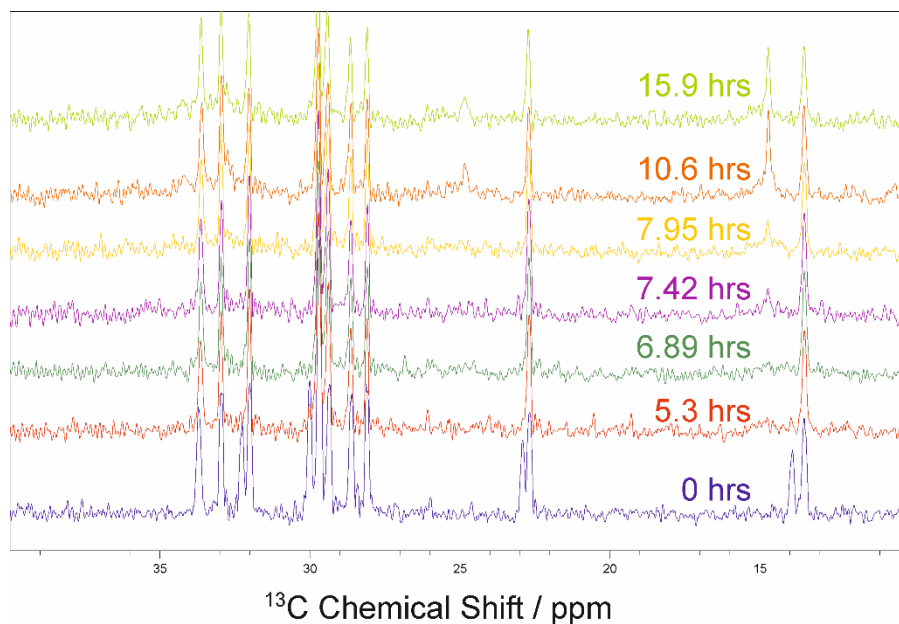
Fig. 5.16 *Intermittent cross sections of the time resolved HPDEC ^{13}C spectrum from 40ppm to 10ppm of the slow crystallization of 1,8-dibromooctane+undecane/urea (55% DBO, 45% UD) in methanol. Note the decay of the liquid undecane peaks and the emergence of the solid undecane peaks. Ten time points have been binned together for each cross section.*

By focussing on this methyl peak we can assess the neighbour environment of undecane guest molecules as different neighbour guests give rise to slightly different chemical shifts. This splitting effect is observable on NMR but this instance we see very few Me⋯Br interactions (Fig. 5.17 and Fig. 5.18) so the effect is not very clear and merely looks like a shoulder on our cross section scans.
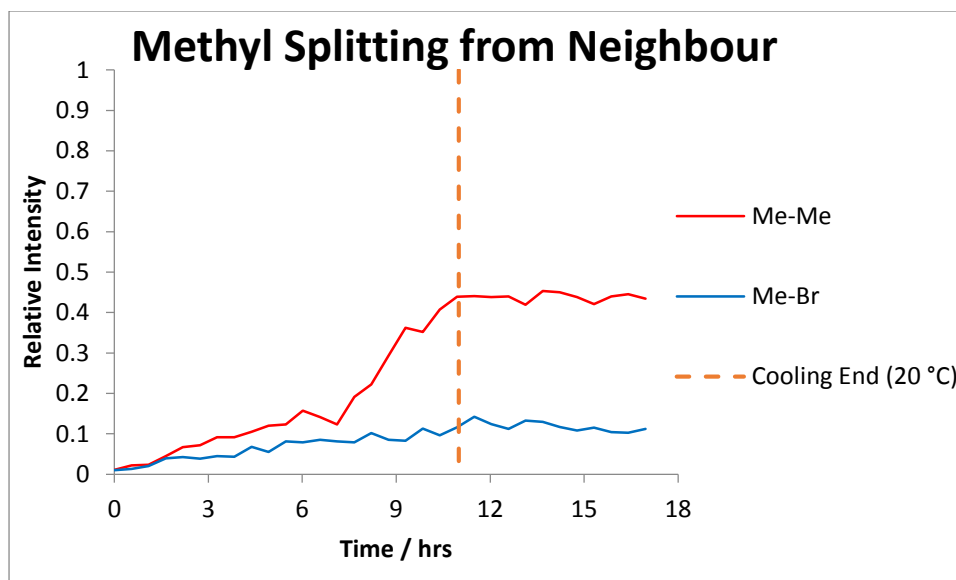
Fig. 5.17 *Evolution of the solid methyl peak (as Me-Me or Me-Br) with time during the DBO+UD/urea slow crystallization experiment. Intensity scale is normalized relative to the total methyl signal (i.e. solution methyl signal + solid methyl signal + liquid methyl signal). The cooling end point has been indicated. Ten time points have been binned together for this plot.*
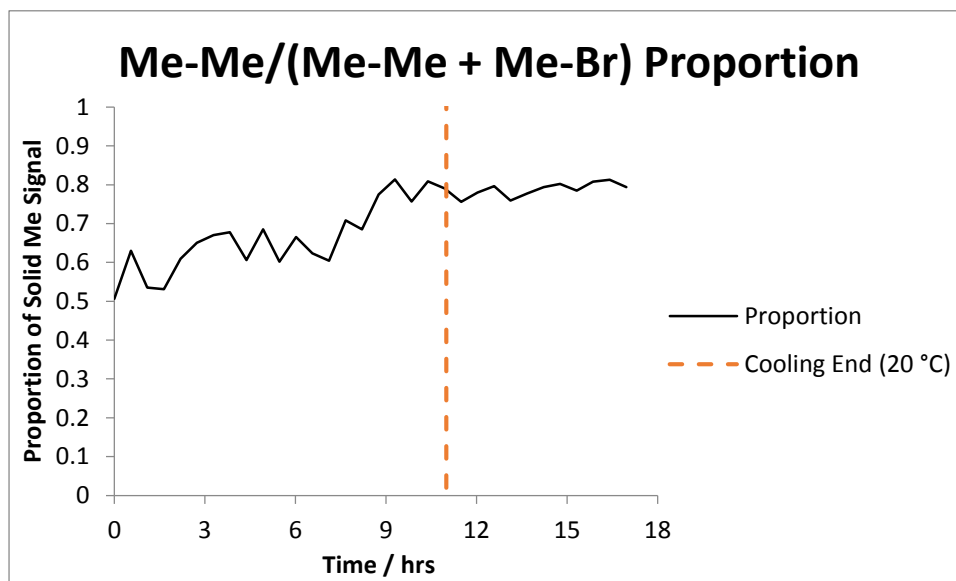
Fig. 5.18 *Proportion of the Me-Me in the total solid methyl peak (Me-Me + Me-Br) with time during the DBO+UD/urea slow crystallization experiment. The cooling end point has been indicated. Ten time points have been binned together for this plot.*

Comparisons of the time evolution of the methyl carbon ($\underline{C}H_3$) and the position adjacent to the methyl carbon ($\underline{C}H_2CH_3$) show the end group giving much stronger signal (Fig. 5.19) even though the population of the two sites must be equal.
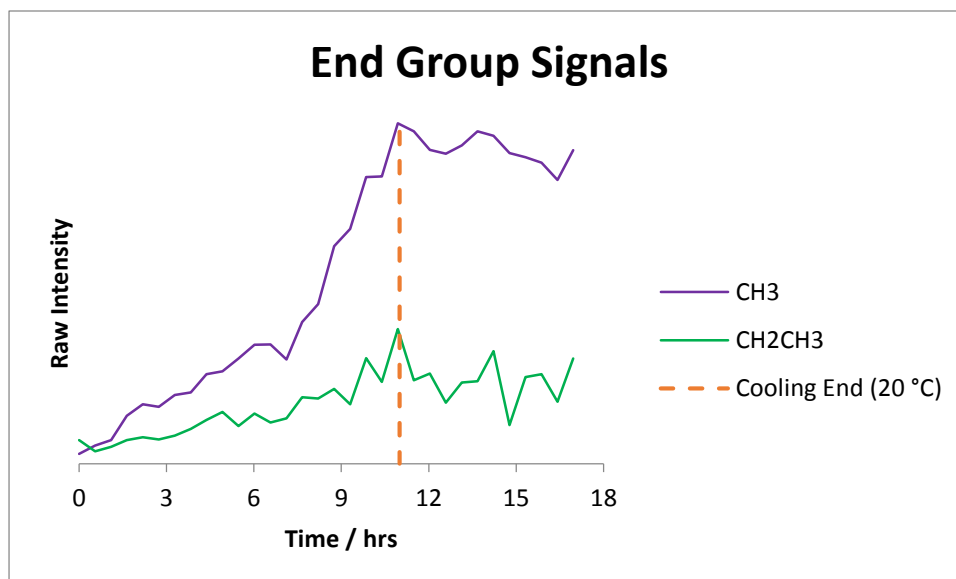
Fig. 5.19 *Time evolution of the signal from the CH₃ and CH₂CH₃ of undecane during the DBO+UD/urea slow crystallization experiment. The cooling end point has been indicated. Ten time points have been binned together for this plot.*

By comparing the methyl signal in the solution, liquid and solid phase we can assess the progress of crystallization (Fig. 5.20 and Fig. 5.21). Over the course of the crystallization process, we see a consistent decrease of the liquid methyl signal alongside a consistent increase of the solid signal whilst the solution methyl signal remains constant. It is only after the liquid phase has been fully depleted that the solution signal starts decreasing. Fig 5.20 shows the raw data and includes the total methyl signal in this plot to confirm that total methyl signal is not changing significantly, Fig 5.21 shows normalized data as a proportion of this total amount.
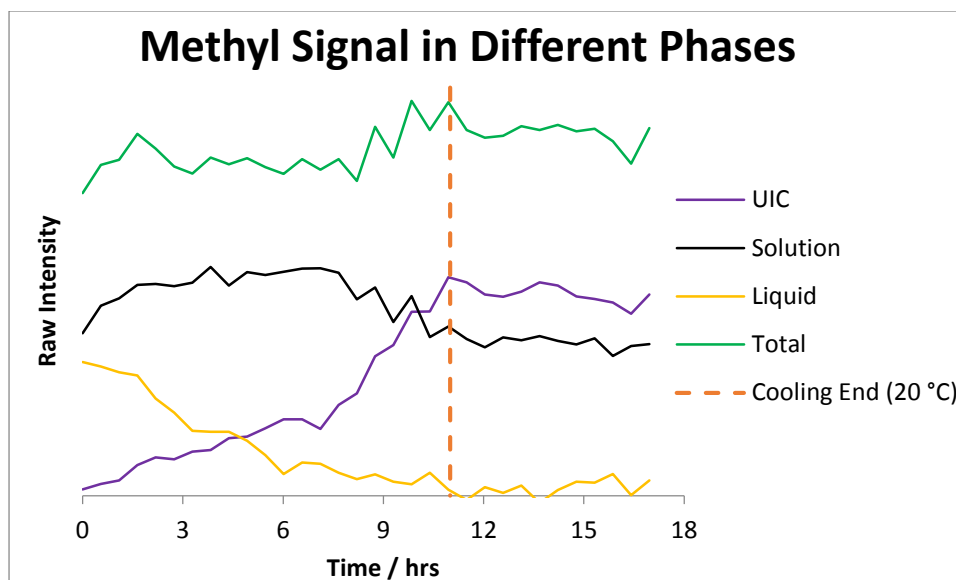
Fig. 5.20 *Evolution of the methyl peak (in solution, liquid and solid phases) with time during the DBO+UD/urea slow crystallization experiment. Total methyl signal is included for comparison and the cooling end point has been indicated. Ten time points have been binned together for this plot.*
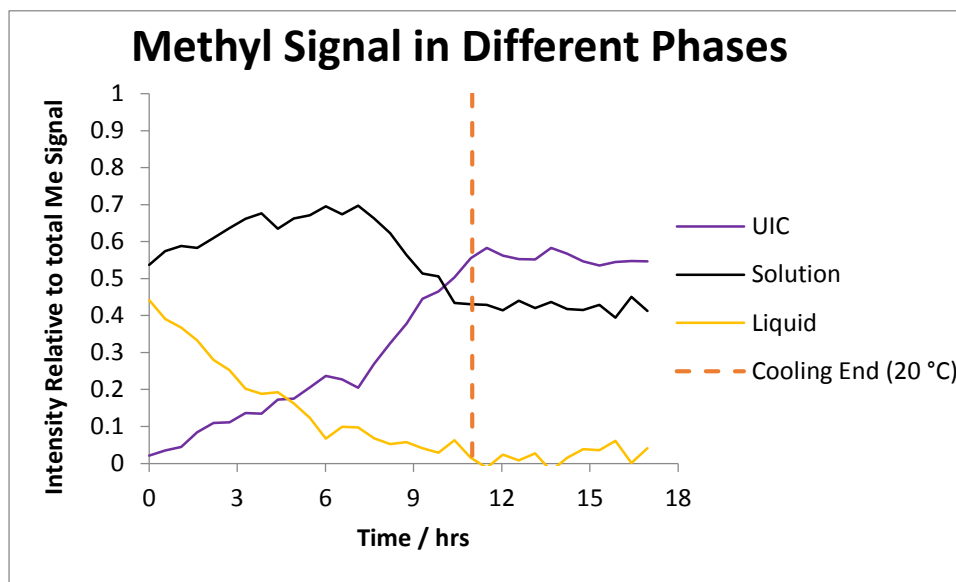
Fig. 5.21 *Evolution of the methyl peak (in solution, liquid and solid phases) with time during the DBO+UD/urea slow crystallization experiment. Intensity scale is normalized relative to the total methyl signal (i.e. solution methyl signal + solid methyl signal + liquid methyl signal). The cooling end point has been indicated. Ten time points have been binned together for this plot.*

5.4.2 Fast crystallization of DBO (55%) & UD (45%) / Urea in Methanol

Over the course of our fast cooling experiment (Fig. 5.22) we see the disappearance of the liquid UD signal followed by the appearance of solid signal from UD in the UIC and the appearance of solid signal for DBO in the UIC. Interestingly there is little change in the splitting of the UD methyl peak. DBO and UD solid signals arise at approximately the same time as each other.
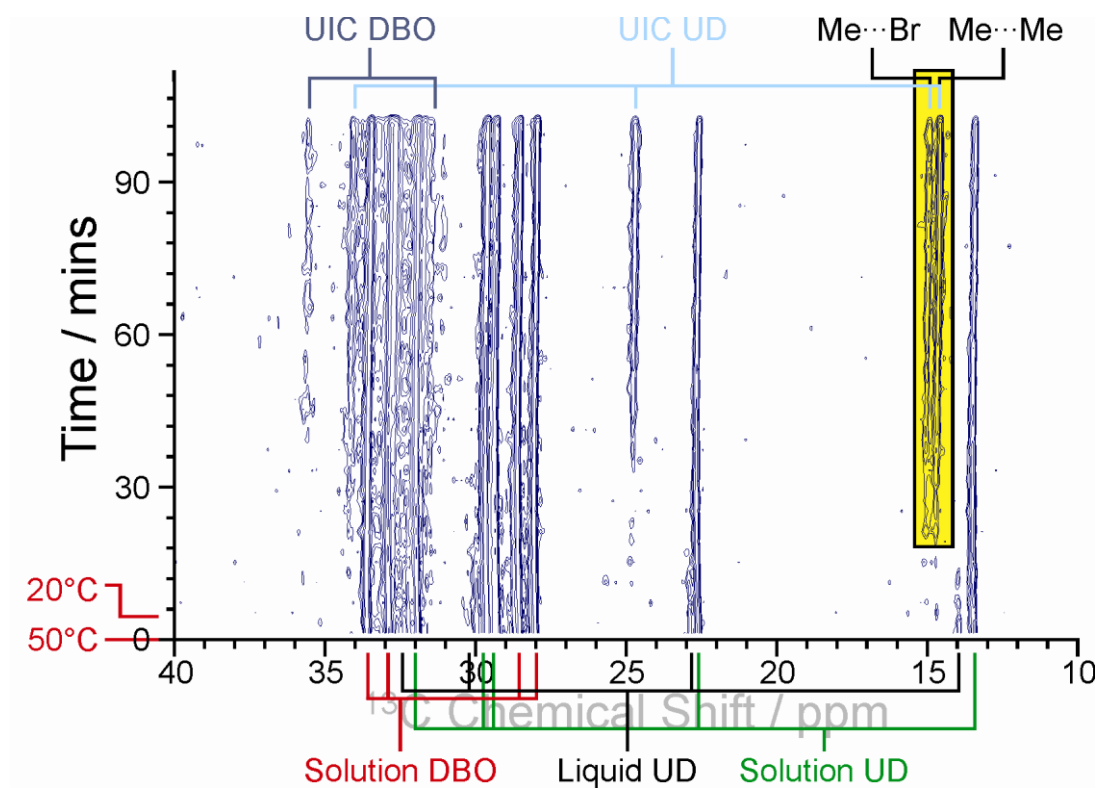
Fig. 5.22 *Time resolved HPDEC ^{13}C spectrum from 40ppm to 10ppm of the fast crystallization of 1,8-dibromooctane+undecane/urea (55% DBO, 45% UD) in methanol. Only positive intensity is shown. Chemical shift (ppm) occupies the horizontal axis, time (mins) occupies the vertical axis and the cooling period has been denoted on this axis. Liquid and solution peaks are labelled at the bottom of the spectrum, solid peaks are labelled at the top of the spectrum. The splitting of the methyl peak by neighbour environment is highlighted in yellow.*

Summing many scans together after crystallization has finished allows us to assess the end point of the process (Fig. 5.23) whilst taking cross sections of the NMR spectra at different time intervals allows us to see how the NMR spectrum changes with time (Fig. 5.24). These cross sections clearly show the decay of the liquid UD methyl peak at 14 ppm followed by the emergence of the solid UD methyl peak at 15 ppm and the UD $\underline{C}H_2CH_3$ peak at 24 ppm.
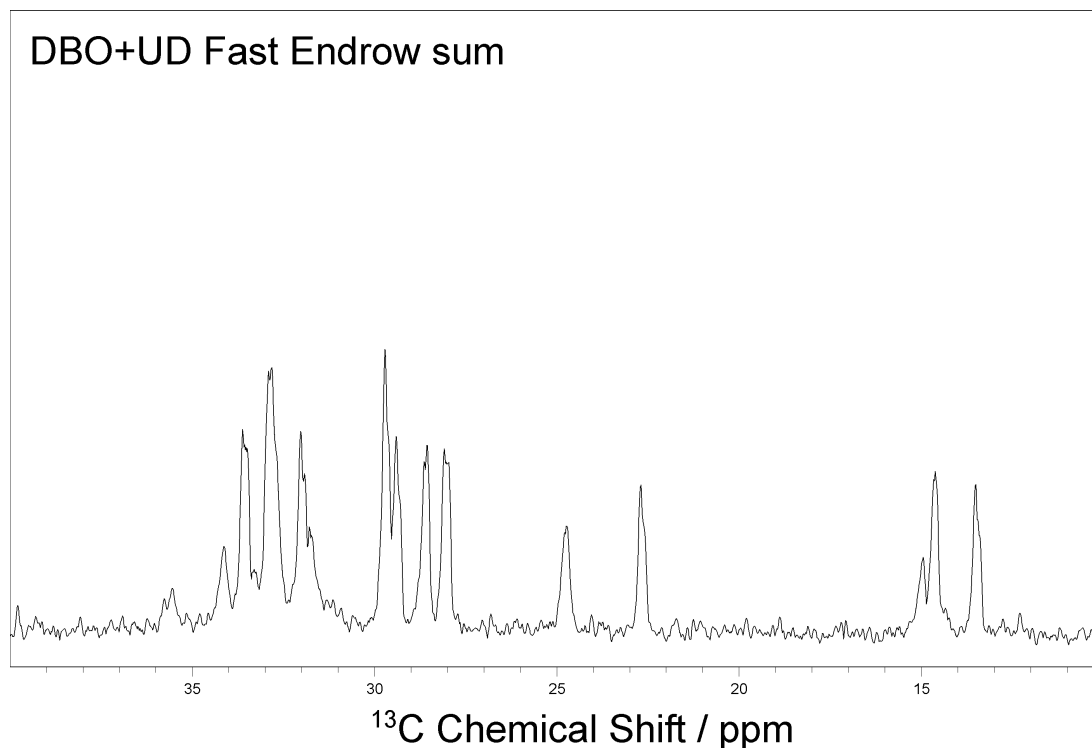
Fig. 5.23 Sum of the last 50 rows of the 40ppm to 10ppm range of the time resolved HPDEC ^{13}C spectrum from of the fast crystallization of 1,8-dibromooctane+undecane/urea (55% DBO, 45% UD) in methanol. This represents the end-point of the crystallization process.
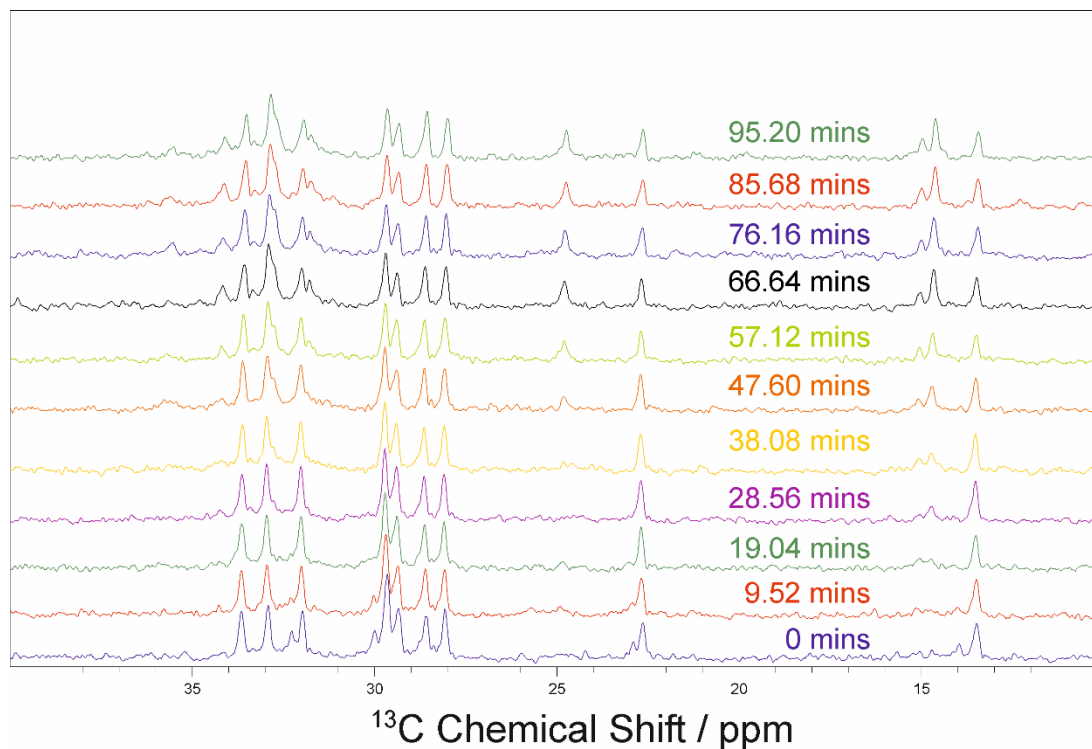
Fig. 5.24 *Intermittent cross sections of the time resolved HPDEC ^{13}C spectrum from 40ppm to 10ppm of the fast crystallization of 1,8-dibromooctane+undecane/urea (55% DBO, 45% UD) in methanol. Note the decay of the liquid undecane peaks and the emergence of the solid undecane and DBO peaks. Four time points have been binned together for each cross section.*

By focussing on this methyl peak we can assess the neighbour environment of undecane guest molecules as different neighbour guests give rise to slightly different chemical shifts. We see a clear splitting of the methyl peak with the Me⋯Br peak being distinct from the Me⋯Me peak. This splitting effect is observable on NMR but this instance we see very few Me⋯Br interactions (Fig. 5.25 and Fig. 5.26) so the effect is not very clear.
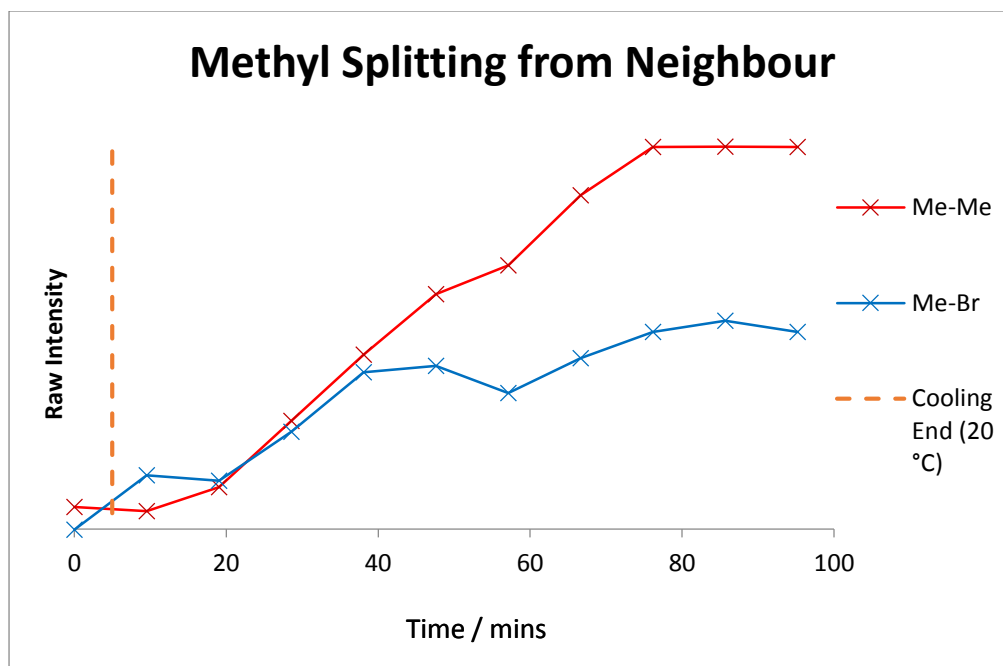
Fig. 5.25 *Evolution of the solid methyl peak (as Me-Me or Me-Br) with time during the DBO+UD/urea fast crystallization experiment. The cooling end point has been indicated. Four time points have been binned together for this plot.*
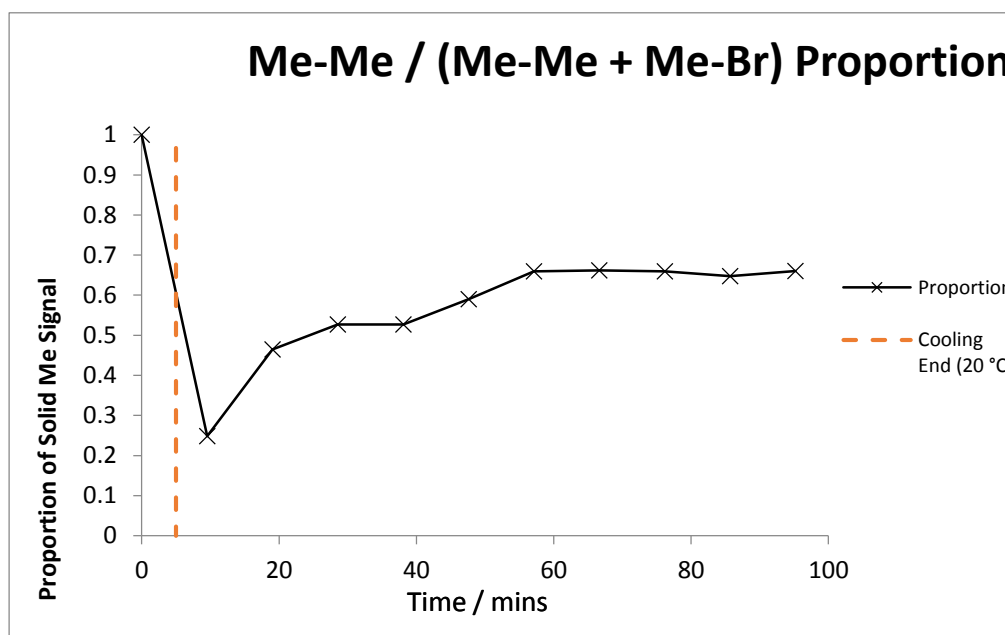
Fig. 5.26 *Proportion of the Me-Me in the total solid methyl peak (Me-Me + Me-Br) with time during the DBO+UD/urea fast crystallization experiment. The cooling end point has been indicated. Four time points have been binned together for this plot.*

By comparing the signals from the different end-groups we see weaker signal from the carbon adjacent to the bromine than the carbons in the undecane (Fig. 5.27). Additionally comparisons of the time evolution of the methyl carbon ($\underline{C}H_3$) and the position adjacent to the methyl carbon ($\underline{C}H_2CH_3$) show the end group giving much stronger signal even though the population of the two sites must be equal. Figs 5.28 and 5.29 show direct comparisons between $\underline{C}H_2Br$ signal and $\underline{C}H_3$ and $\underline{C}H_2CH_3$ signal.
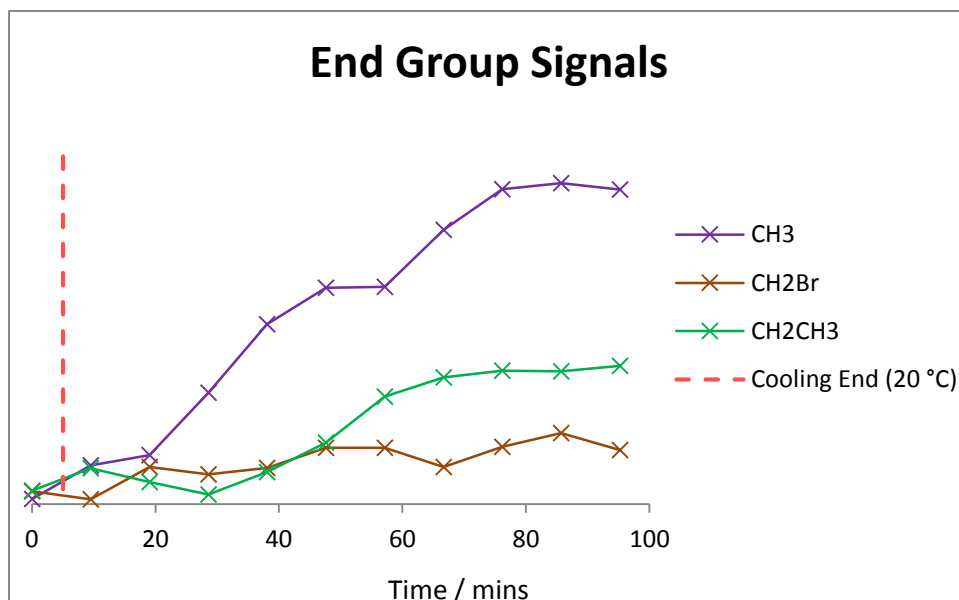
Fig. 5.27 *Time evolution of the signal from the CH_3 and CH_2CH_3 of undecane, and the CH_2Br of 1,8-dibromooctane during the DBO+UD/urea fast crystallization experiment. The cooling end point has been indicated. Four time points have been binned together for this plot.*
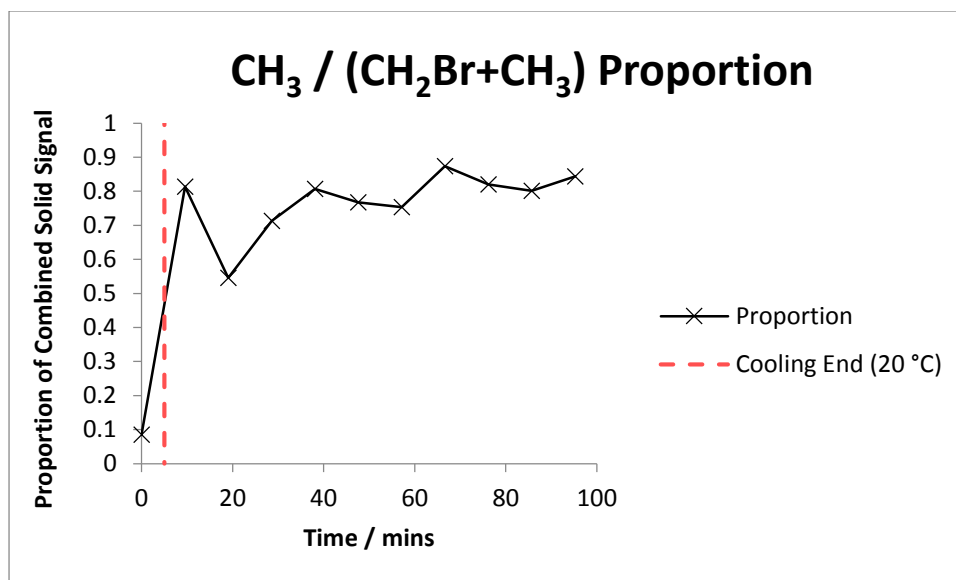
Fig. 5.28 *A comparison of the UD end-group signal with the DBO end-group signal by taking the proportion of the CH₃ signal compared to the total from CH₃ and CH₂Br with time during the DBO+UD/urea fast crystallization experiment. The cooling end point has been indicated. Four time points have been binned together for this plot.*
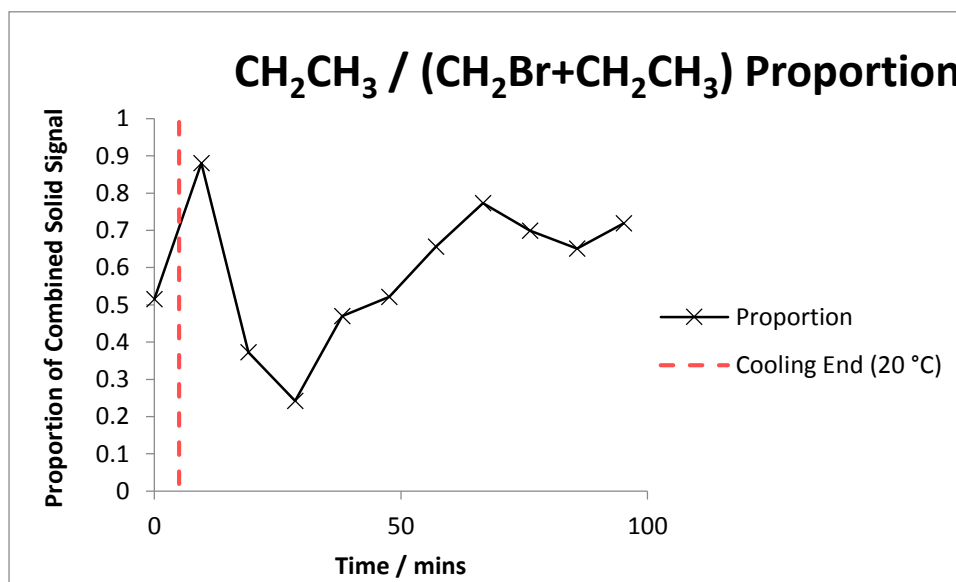
Fig. 5.29 *A comparison of the UD signal from the carbon adjacent to end-group with the DBO end-group signal by taking the proportion of the CH₂CH₃ signal compared to the total from CH₂CH₃ and CH₂Br with time during the DBO+UD/urea fast crystallization experiment. The cooling end point has been indicated. Four time points have been binned together for this plot.*

By comparing the methyl signal in the solution, liquid and solid phase we can assess the progress of crystallization (Fig. 5.30 and Fig 5.31). Over the course of the crystallization process we see a decrease of the liquid methyl signal and a slight decrease of the solution methyl signal alongside a consistent increase of the solid signal. Fig 5.30 shows the raw data and includes the total methyl signal in this plot which shows a significant increase in total methyl signal, Fig 5.31 shows normalized data as a proportion of this total amount. The increase in total signal is understandable as NMR only probes a small part of the sample near the bottom of the rotor so in a non-homogenous rotor we can observe an increase in signal if material moves from the top of the rotor (unsampled region) to the bottom of the rotor (sampled region). The pure liquid undecane is slightly less dense than the solution whilst the solid is more dense than the solution so over the course of crystallization undecane moves from the unsampled liquid to the sampled solid.
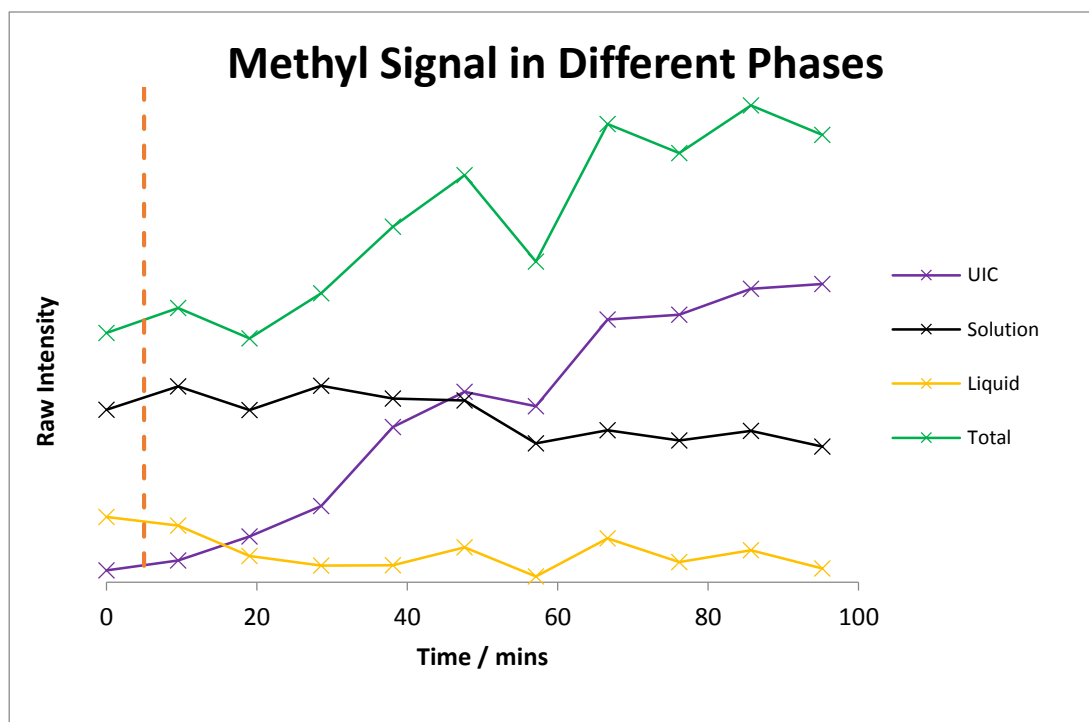
Fig. 5.31 *Evolution of the methyl peak (in solution, liquid and solid phases) with time during the DBO+UD/urea fast crystallization experiment. Total methyl signal is included for comparison and the cooling end point has been indicated. Four time points have been binned together for this plot.*
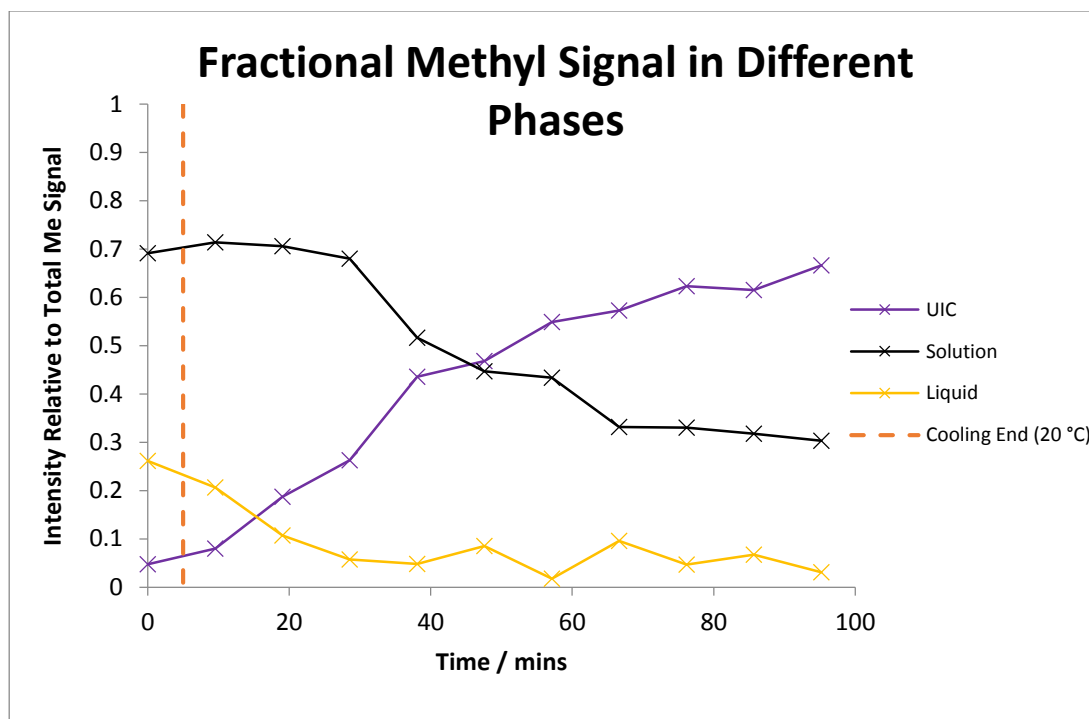
Fig. 5.31 *Evolution of the methyl peak (in solution, liquid and solid phases) with time during the DBO+UD/urea fast crystallization experiment. Intensity scale is normalized relative to the total methyl signal (i.e. solution methyl signal + solid methyl signal + liquid methyl signal). The cooling end point has been indicated. Four time points have been binned together for this plot.*

5.4.3 Slow crystallization of DBO (34%) & TD (66%) / Urea in Methanol

Over the course of our slow cooling experiment (Fig. 5.32) we see the weakening of TD liquid signals followed by the appearance of solid signal from TD in the UIC. We do not observe DBO signals in the UIC nor do we see splitting of the TD methyl peak but we clearly see DBO in solution showing that it was present in the crystal. Crystallization occurs at approximately the 3 hour mark. The TD CH_2CH_3 peak appears much weaker than the TD CH_3 peak.
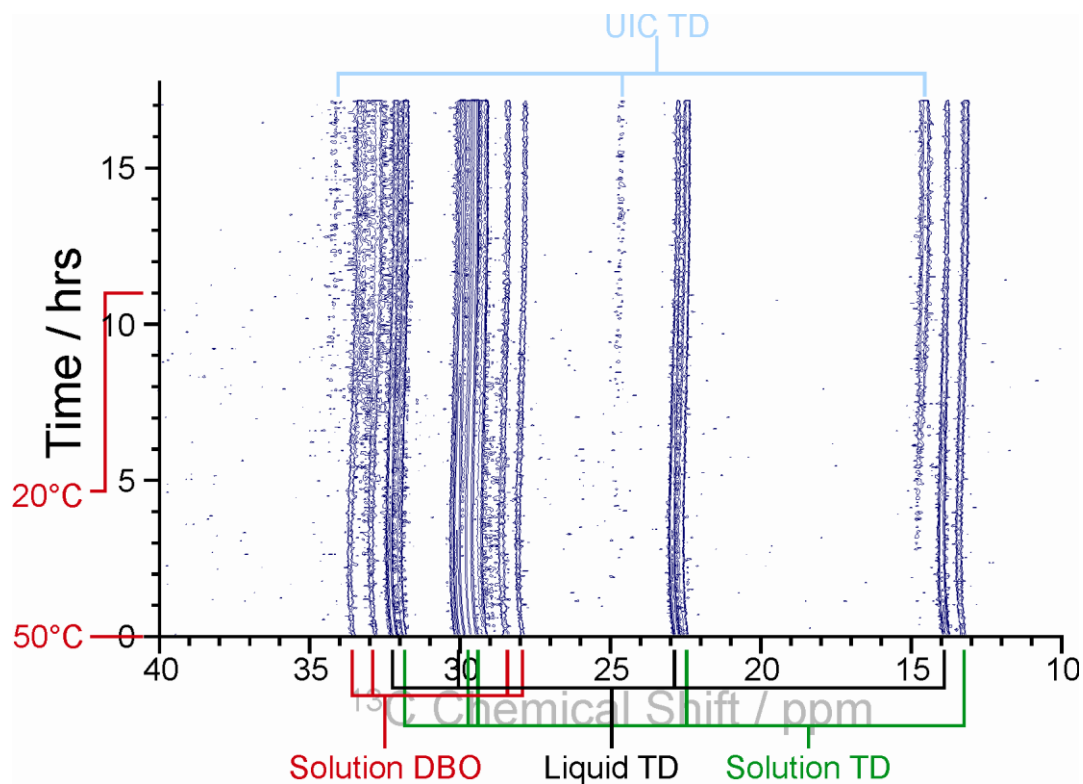
Fig. 5.32 *Time resolved HPDEC ^{13}C spectrum from 40ppm to 10ppm of the slow crystallization of 1,8-dibromooctane+tetradecane/urea (34% DBO, 66% UD) in methanol. Only positive intensity is shown. Chemical shift (ppm) occupies the horizontal axis, time (hrs) occupies the vertical axis and the cooling period has been denoted on this axis. Liquid and solution peaks are labelled at the bottom of the spectrum, solid peaks are labelled at the top of the spectrum.*

Taking cross sections of the NMR spectra at different time intervals allows us to see how the NMR spectrum changes with time (Fig. 5.33). These cross sections clearly show the decay of the liquid TD methyl peak at 14 ppm followed by the emergence of the solid TD methyl peak at 15 ppm.
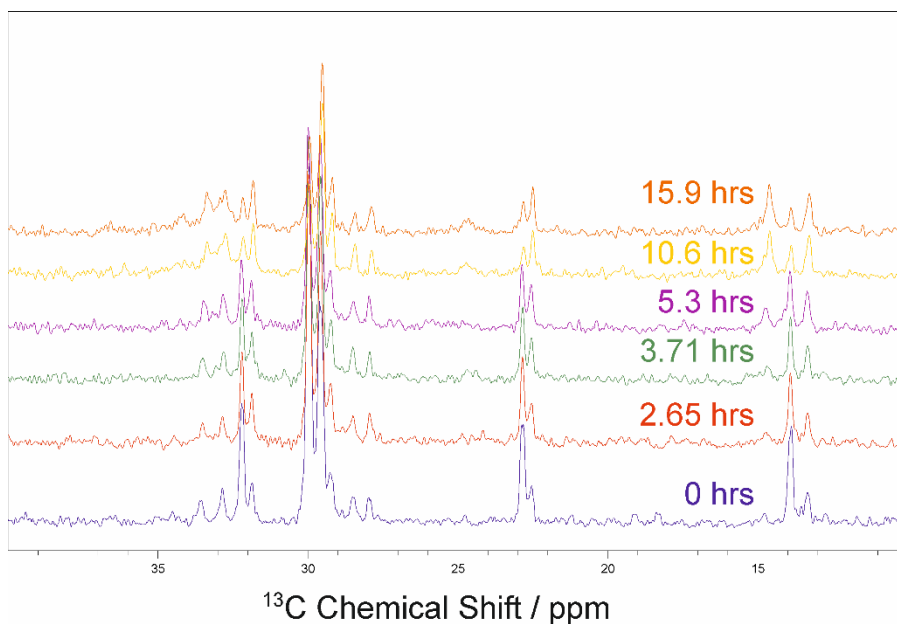
Fig. 5.33 *Intermittent cross sections of the time resolved HPDEC ^{13}C spectrum from 40ppm to 10ppm of the slow crystallization of 1,8-dibromooctane+tetradecane/urea (34% DBO, 66% TD) in methanol. Note the weakening of the liquid tetradecane peaks and the emergence of the solid undecane peaks. Ten time points have been binned together for each cross section.*

Comparisons of the time evolution of the methyl carbon (CH$_3$) and the position adjacent to the methyl carbon (CH$_2$CH$_3$) show the end group giving much stronger signal (Fig. 5.34) even though the population of the two sites must be equal.
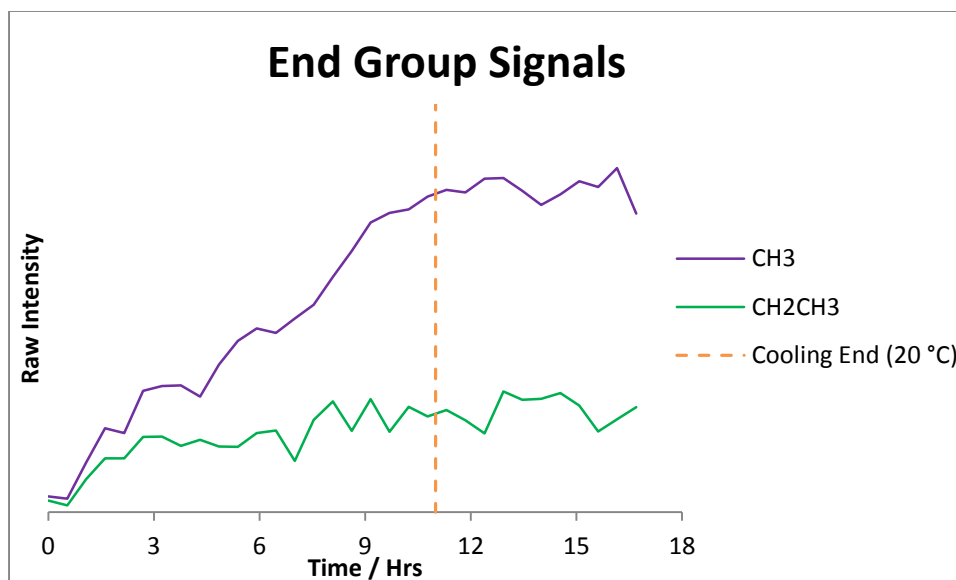
Fig. 5.34 *Time evolution of the signal from the CH₃ and CH₂CH₃ of tetradecane during the DBO+TD/urea slow crystallization experiment. The cooling end point has been indicated. Ten time points have been binned together for this plot*

By comparing the methyl signal in the solution, liquid and solid phase we can assess the progress of crystallization (Fig. 5.35 and Fig. 5.36). Over the course of the crystallization process we see a consistent decrease of the liquid methyl signal alongside a consistent increase of the solid signal whilst the solution methyl signal remains relatively constant. Fig 5.35 shows the raw data and includes the total methyl signal in this plot to confirm that total methyl signal is not changing significantly, Fig 5.36 shows normalized data as a proportion of this total amount.
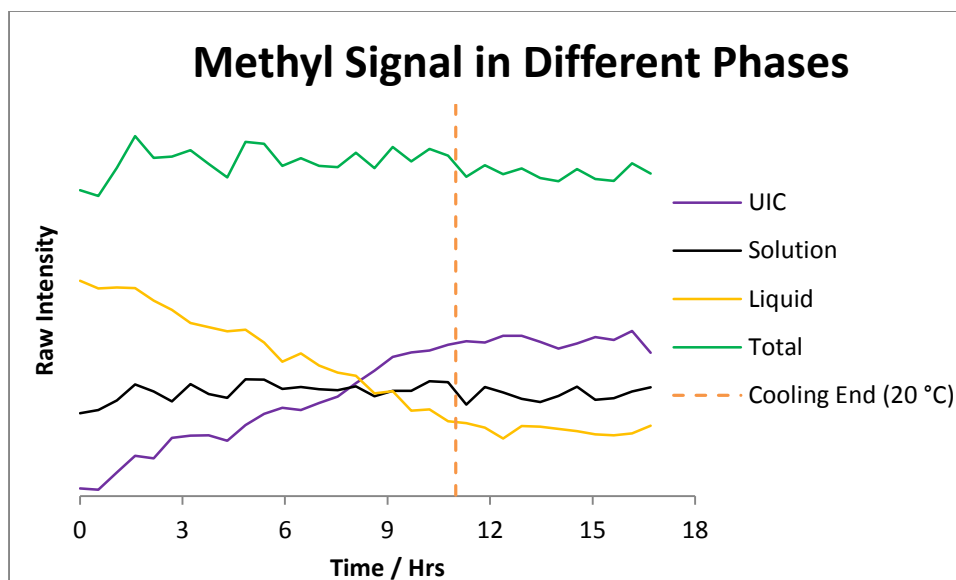
Fig. 5.35 *Evolution of the methyl peak (in solution, liquid and solid phases) with time during the DBO+UD/urea slow crystallization experiment. Total methyl signal is included for comparison and the cooling end point has been indicated. Ten time points have been binned together for this plot.*
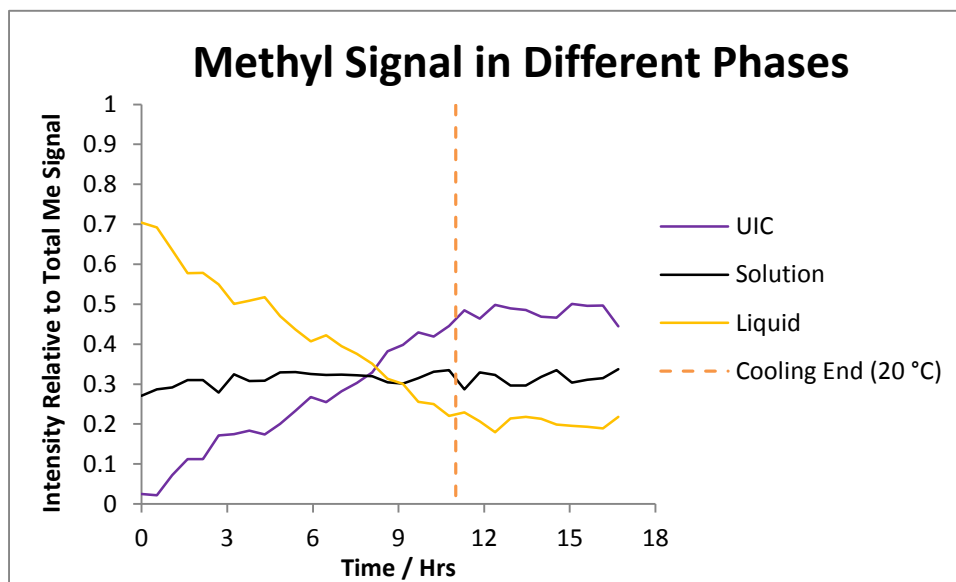
Fig. 5.36 *Evolution of the methyl peak (in solution, liquid and solid phases) with time during the DBO+TD/urea slow crystallization experiment. Intensity scale is normalized relative to the total methyl signal (i.e. solution methyl signal + solid methyl signal + liquid methyl signal). The cooling end point has been indicated. Ten time points have been binned together for this plot*

5.4.4 Fast crystallization of DBO (34%) & TD (66%) / Urea in Methanol

Over the course of our fast cooling experiment (Fig. 5.37) we see the weakening of TD liquid signals followed by the appearance of solid signal from TD in the UIC. We do not observe DBO signals in the UIC nor do we see splitting of the TD methyl peak, but we clearly see DBO in solution showing that it was present in the crystal. Crystallization occurs almost immediately. The TD CH_2CH_3 peak appears much weaker than the TD CH_3 peak.
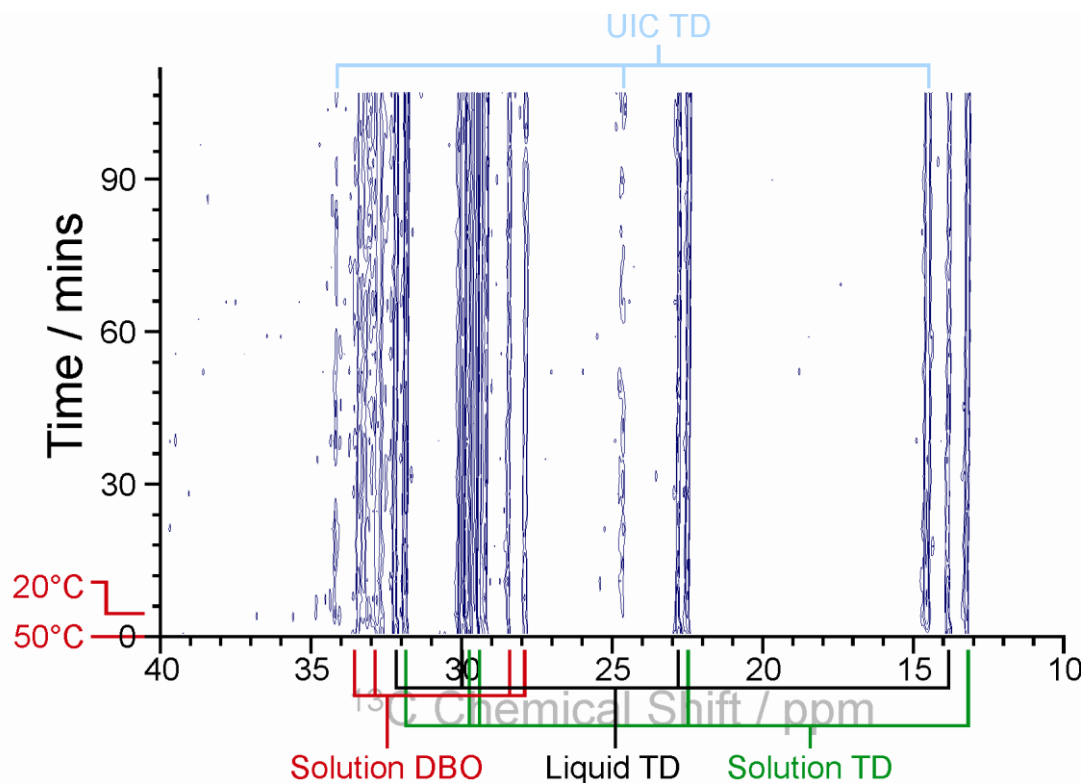
Fig. 5.37 *Time resolved HPDEC ^{13}C spectrum from 40ppm to 10ppm of the fast crystallization of 1,8-dibromooctane+tetradecane/urea (34% DBO, 66% UD) in methanol. Only positive intensity is shown. Chemical shift (ppm) occupies the horizontal axis, time (mins) occupies the vertical axis and the cooling period has been denoted on this axis. Liquid and solution peaks are labelled at the bottom of the spectrum, solid peaks are labelled at the top of the spectrum.*

Fig. 5.38 shows the time evolution of the two tetradecane carbons towards the end of the chain whilst Fig. 5.39 and Fig.5.40 show the time evolution of the methyl peak in

solid liquid and solution phases. Fig 5.39 shows the raw data and includes the total methyl signal in this plot to confirm that total methyl signal is not changing significantly, Fig 5.40 shows normalized data as a proportion of this total amount. Little change is seen on these plots as crystallization finishes early in the experiment.
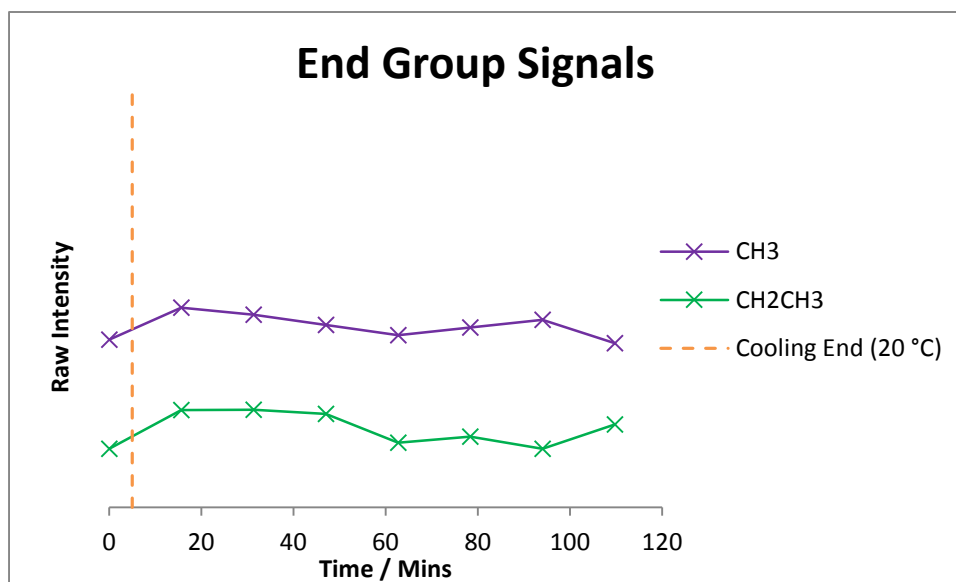
Fig. 5.38 *Time evolution of the signal from the CH$_3$ and CH$_2$CH$_3$ of tetradecane during the DBO+TD/urea fast crystallization experiment. The cooling end point has been indicated. Four time points have been binned together for this plot.*
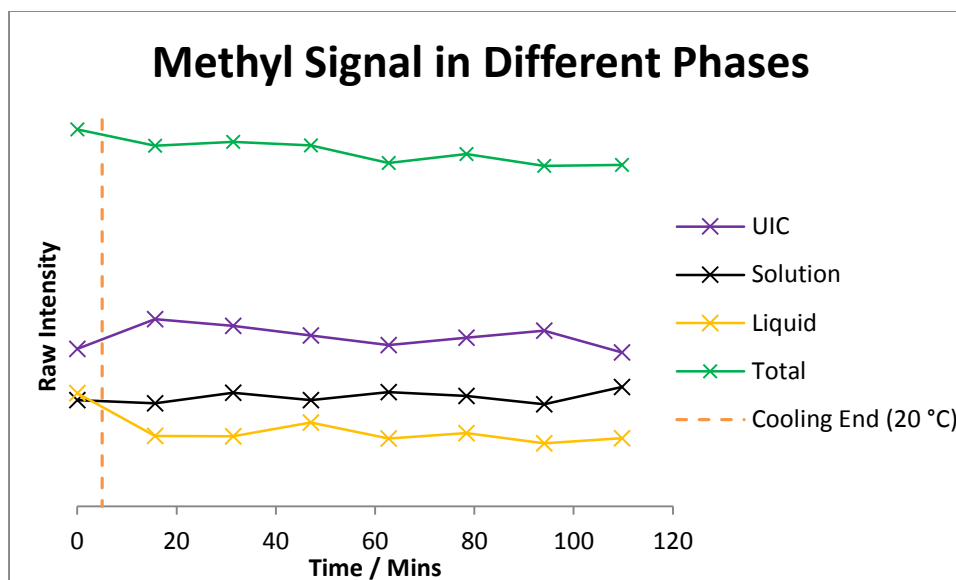
Fig. 5.39 Evolution of the methyl peak (in solution, liquid and solid phases) with time during the DBO+TD/urea fast crystallization experiment. Total methyl signal is included for comparison and the cooling end point has been indicated. Four time points have been binned together for this plot
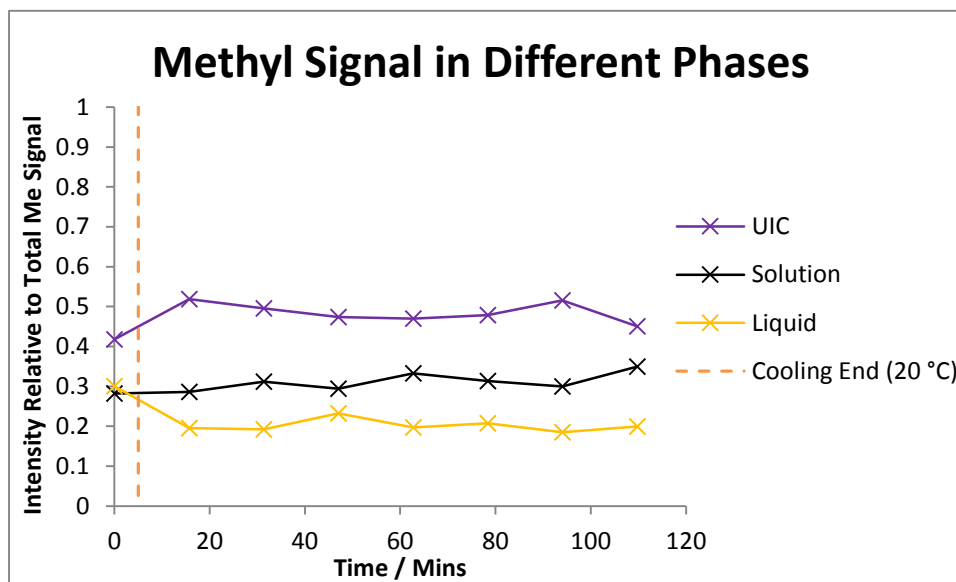
Fig. 5.40 Evolution of the methyl peak (in solution, liquid and solid phases) with time during the DBO+TD/urea fast crystallization experiment. Intensity scale is normalized relative to the total methyl signal (i.e. solution methyl signal + solid methyl signal + liquid methyl signal). The cooling end point has been indicated. Four time points have been binned together for this plot.

5.4.5 Slow crystallization of DBDD (57%) & UD (43%) / Urea in Methanol

Over the course of our slow cooling experiment (Fig. 5.41) we see the disappearance of the liquid UD and liquid DBDD signals followed by the appearance of solid signal from UD in the UIC and solid signal from DBDD in the UIC. DBDD and UD solid signals arise at the same time.
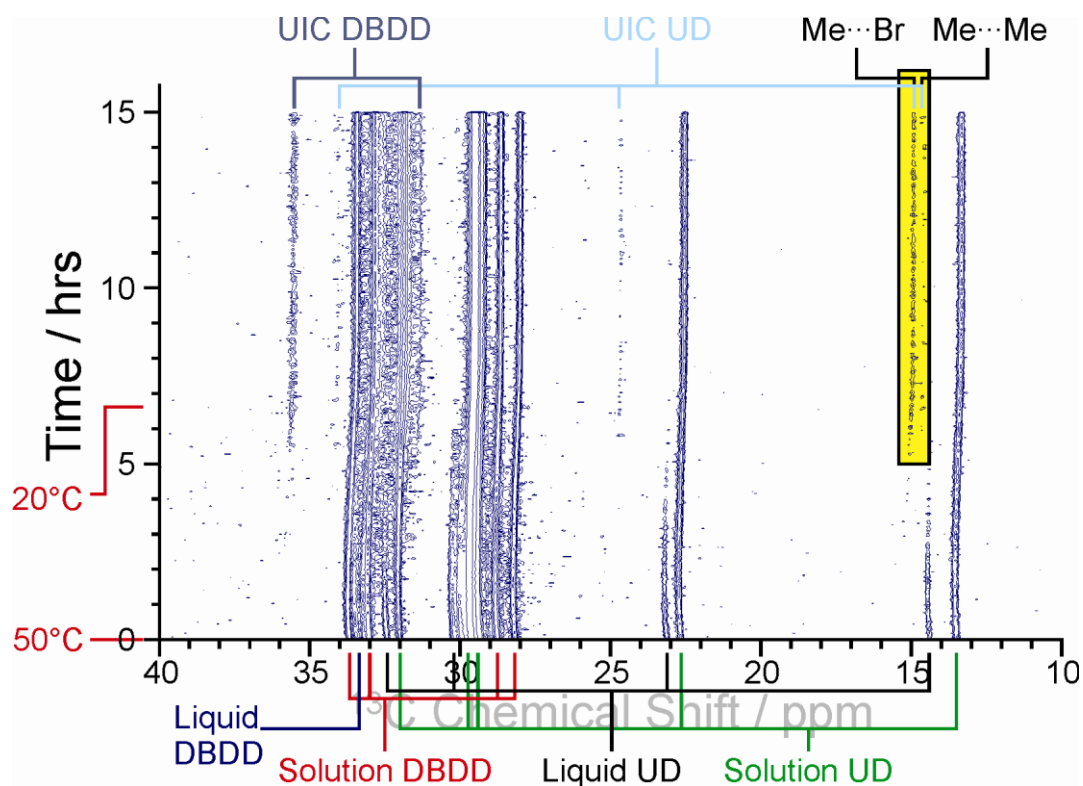
Fig. 5.41 *Time resolved HPDEC ^{13}C spectrum from 40ppm to 10ppm of the slow crystallization of 1,12-dibromododecane+undecane/urea (57% DBDD, 43% UD) in methanol. Only positive intensity is shown. Chemical shift (ppm) occupies the horizontal axis, time (hrs) occupies the vertical axis and the cooling period has been denoted on this axis. Liquid and solution peaks are labelled at the bottom of the spectrum, solid peaks are labelled at the top of the spectrum. The splitting of the methyl peak by neighbour environment is highlighted in yellow.*

Taking cross sections of the NMR spectra at different time intervals allows us to see how the NMR spectrum changes with time (Fig. 5.42). These cross sections clearly

show the decay of the liquid UD methyl peak at 14 ppm followed by the emergence of the solid UD methyl peak at 15 ppm and the solid DBO at 36 ppm.
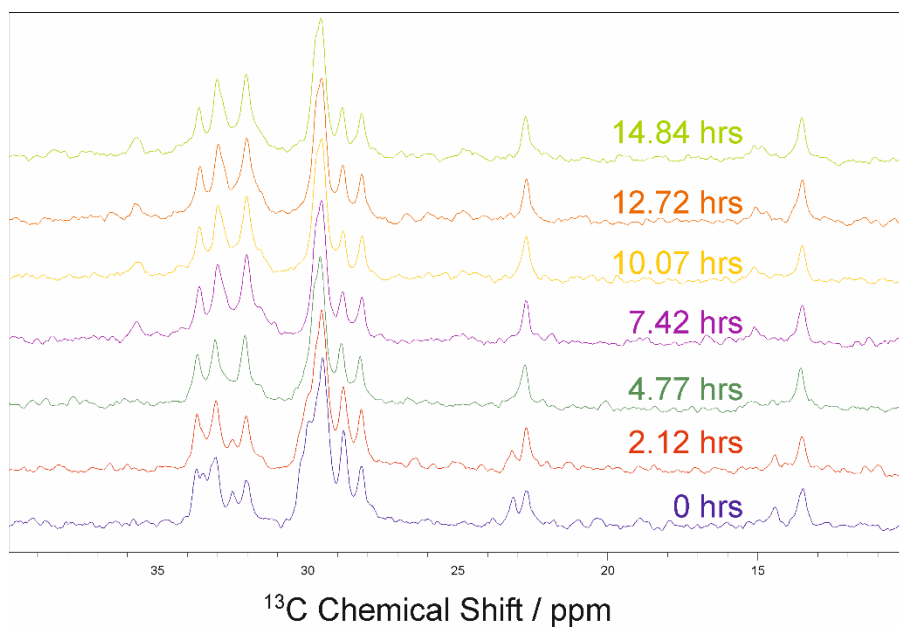
Fig. 5.42 *Intermittent cross sections of the time resolved HPDEC ^{13}C spectrum from 40ppm to 10ppm of the slow crystallization of 1,12-dibromodecane+undecane/urea (57% DBDD, 43% UD) in methanol. Note the decay of the liquid undecane peaks and the emergence of the solid undecane peaks. Ten time points have been binned together for each cross section.*

By focussing on the UD methyl peak, we can assess the neighbour environment of undecane guest molecules as different neighbour guests give rise to slightly different chemical shifts. In this instance, the splitting of the methyl peak suggests that the number of Me⋯Br interactions is slightly higher than the number of Me⋯Me interactions (Fig 5.43 and Fig 5.44).
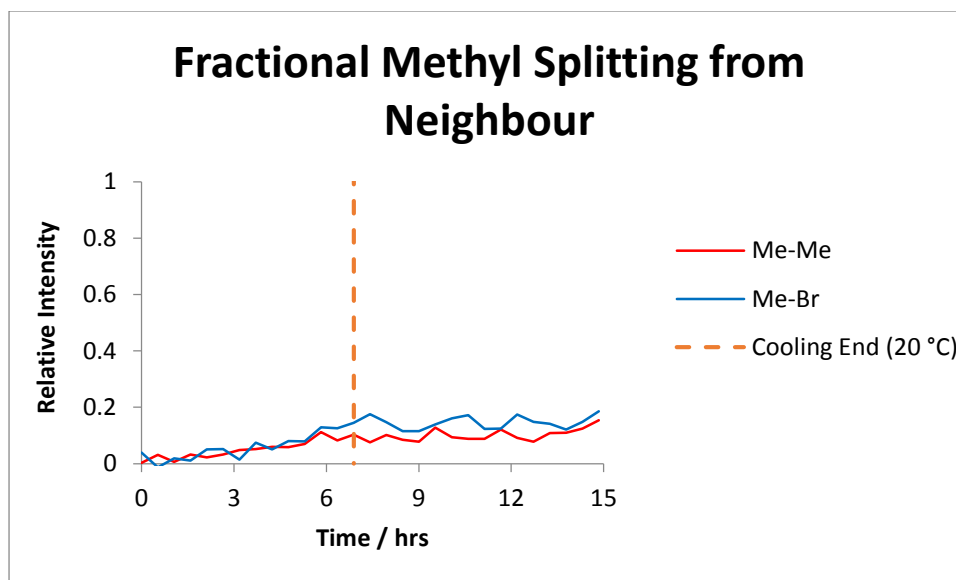
Fig. 5.43 *Evolution of the solid methyl peak (as Me-Me or Me-Br) with time during the DBDD+UD/urea slow crystallization experiment. Intensity scale is normalized relative to the total methyl signal (i.e. solution methyl signal + solid methyl signal + liquid methyl signal). The cooling end point has been indicated. Ten time points have been binned together for this plot.*
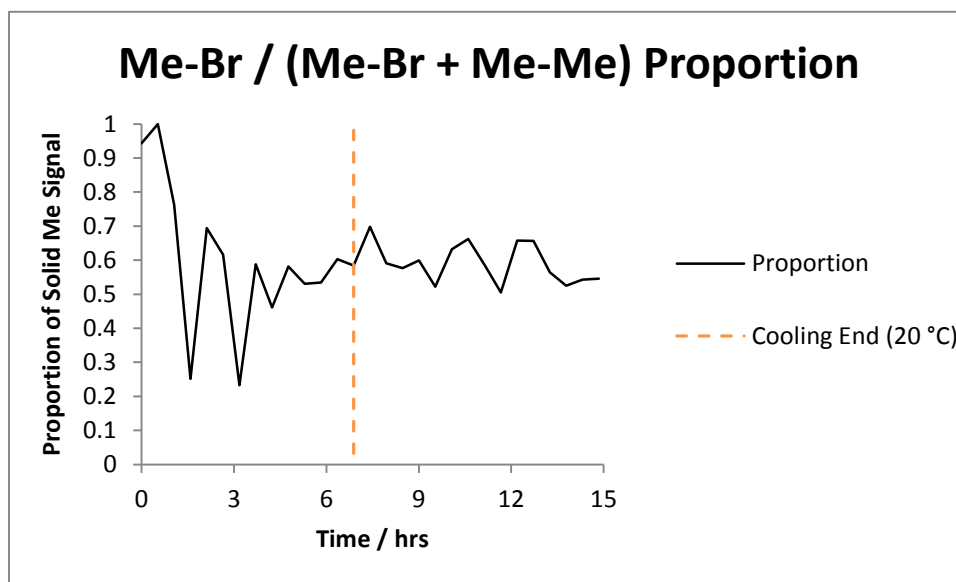
Fig. 5.44 *Proportion of the Me-Me in the total solid methyl peak (Me-Me + Me-Br) with time during the DBDD+UD/urea slow crystallization experiment. The cooling end point has been indicated. Ten time points have been binned together for this plot.*

By comparing the signals from the different end-groups, we see stronger signal from the carbon adjacent to the bromine than from the carbons in the undecane (Fig. 5.45). Additionally, comparisons of the time evolution of the methyl carbon ($\underline{C}H_3$) and the position adjacent to the methyl carbon ($\underline{C}H_2CH_3$) show the end group giving stronger signal even though the population of the two sites must be equal. Figs 5.46 and 5.47 show direct comparisons between $\underline{C}H_2Br$ signal and $\underline{C}H_3$ and $\underline{C}H_2CH_3$ signal.
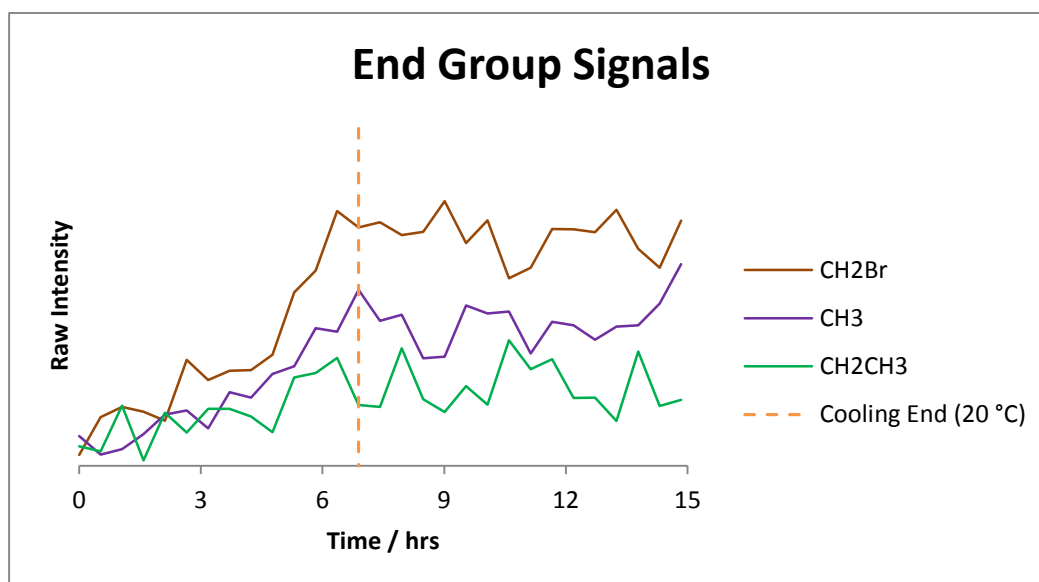
Fig. 5.45 *Time evolution of the signal from the CH₃ and CH₂CH₃ of undecane and the CH₂Br of 1,12-dibromododecane during the DBDD+UD/urea slow crystallization experiment. The cooling end point has been indicated. Ten time points have been binned together for this plot.*
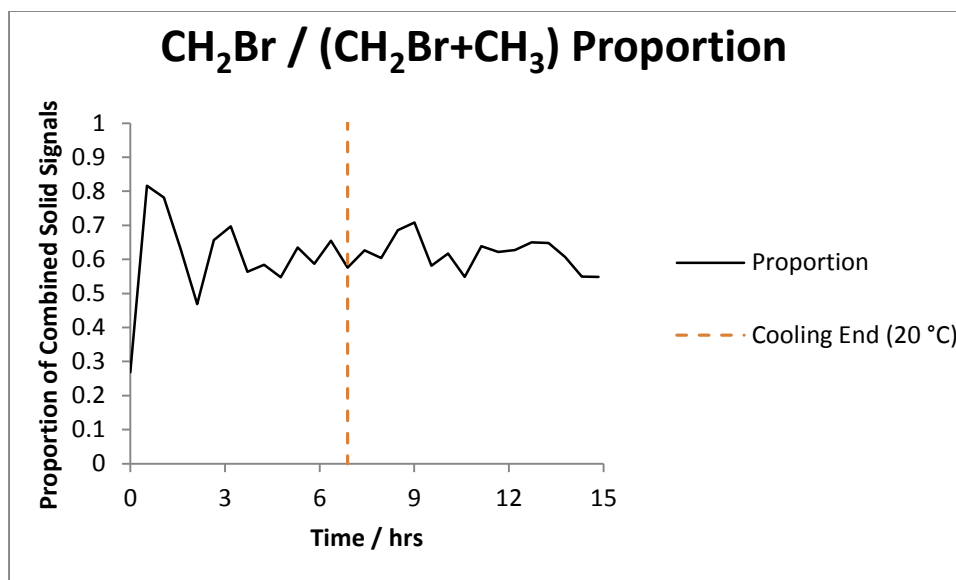
Fig. 5.46 *A comparison of the UD end-group signal with the DBDD end-group signal by taking the proportion of the CH$_2$Br signal compared to the total from CH$_3$ and CH$_2$Br with time during the DBDD+UD/urea slow crystallization experiment. The cooling end point has been indicated. Ten time points have been binned together for this plot.*
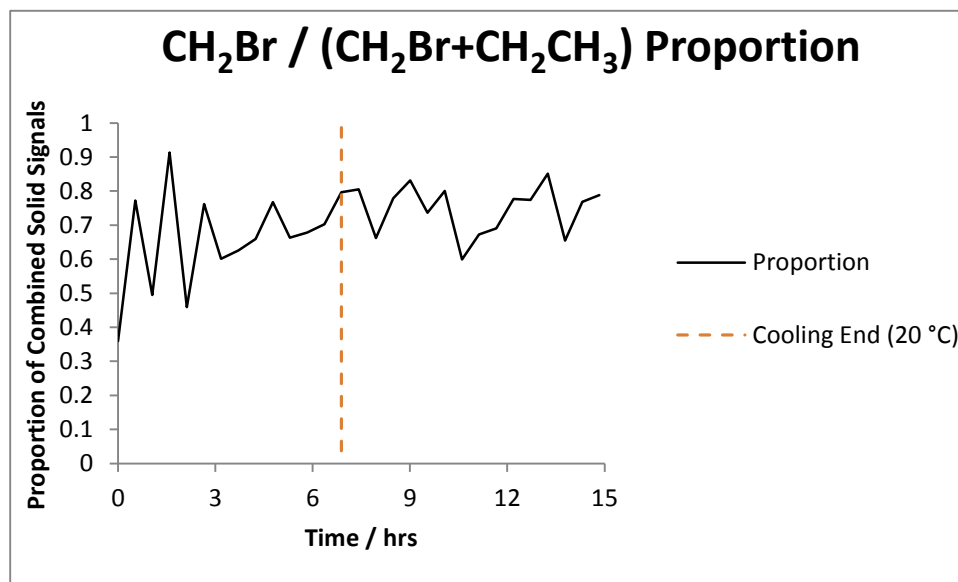
Fig. 5.47 *A comparison of the signal of the carbon adjacent to the end-group with the DBDD end-group signal by taking the proportion of the CH$_2$Br signal compared to the total from CH$_2$CH$_3$ and CH$_2$Br with time during the DBDD+UD/urea slow crystallization experiment. The cooling end point has been indicated. Ten time points have been binned together for this plot*

By comparing the methyl signal in the solution, liquid and solid phase we can assess the progress of crystallization (Fig. 5.48 and Fig. 5.49). Over the course of the crystallization process we see a consistent decrease of the liquid methyl signal alongside a consistent increase of the solid signal whilst the solution methyl signal remains constant. Crystallization finishes when the liquid signal is depleted but before the solution signal starts decreasing. Fig 5.48 shows the raw data and includes the total methyl signal in this plot to confirm that total methyl signal is not changing significantly, Fig 5.49 shows normalized data as a proportion of this total amount.
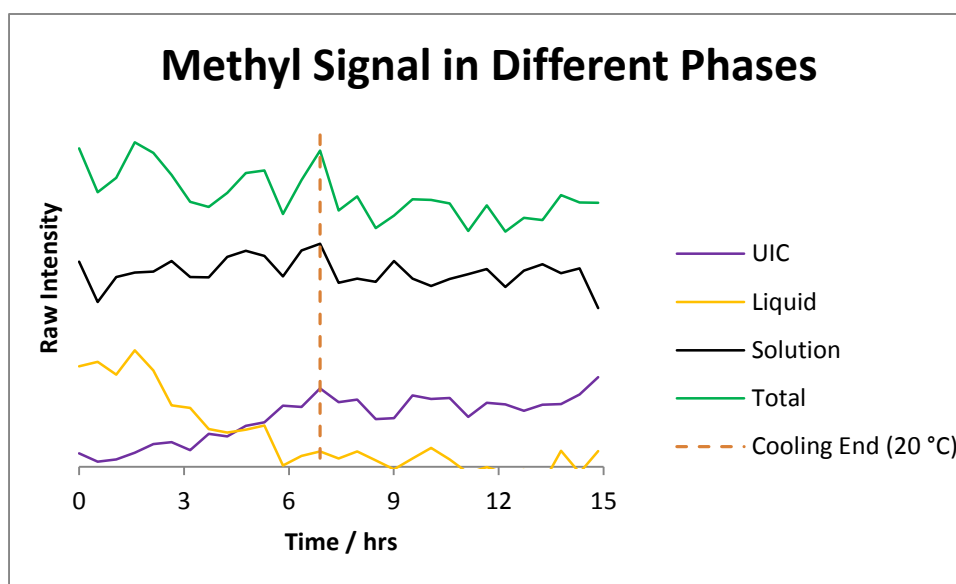
Fig. 5.48 *Evolution of the methyl peak (in solution, liquid and solid phases) with time during the DBO+UD/urea slow crystallization experiment. Total methyl signal is included for comparison and the cooling end point has been indicated. Ten time points have been binned together for this plot.*
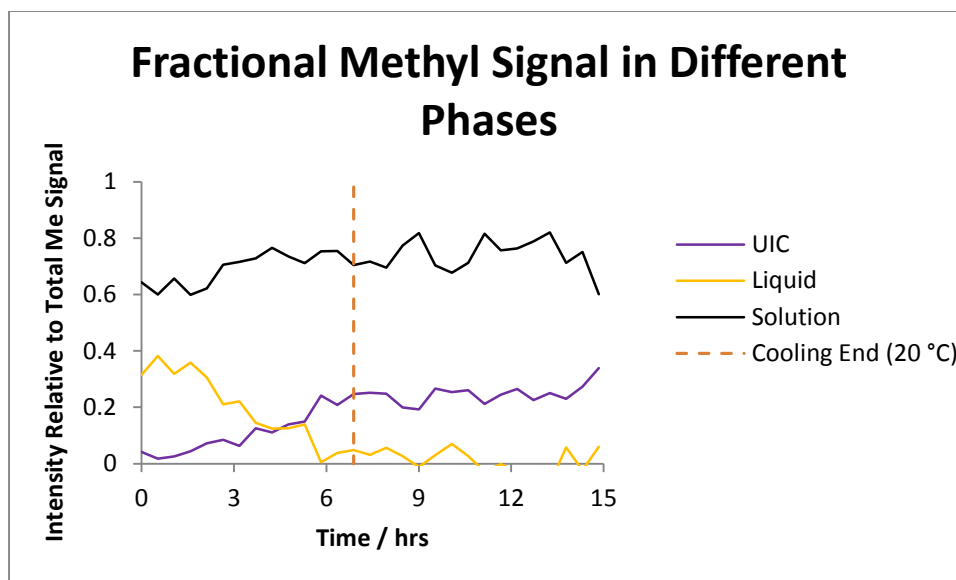
Fig. 5.49 *Evolution of the methyl peak (in solution, liquid and solid phases) with time during the DBDD+UD/urea slow crystallization experiment. Intensity scale is normalized relative to the total methyl signal (i.e. solution methyl signal + solid methyl signal + liquid methyl signal). The cooling end point has been indicated. Ten time points have been binned together for this plot.*

5.4.6 Fast crystallization of DBDD (57%) & UD (43%) / Urea in Methanol

Over the course of our fast cooling experiment (Fig 5.50) we see the disappearance of the liquid UD and liquid DBDD signals followed by the appearance of solid signal from UD in the UIC and solid signal from DBDD in the UIC. However the solid signal shows different splitting of the UD methyl peak, suggesting more DBDD-UD neighbours than UD-UD neighbours.
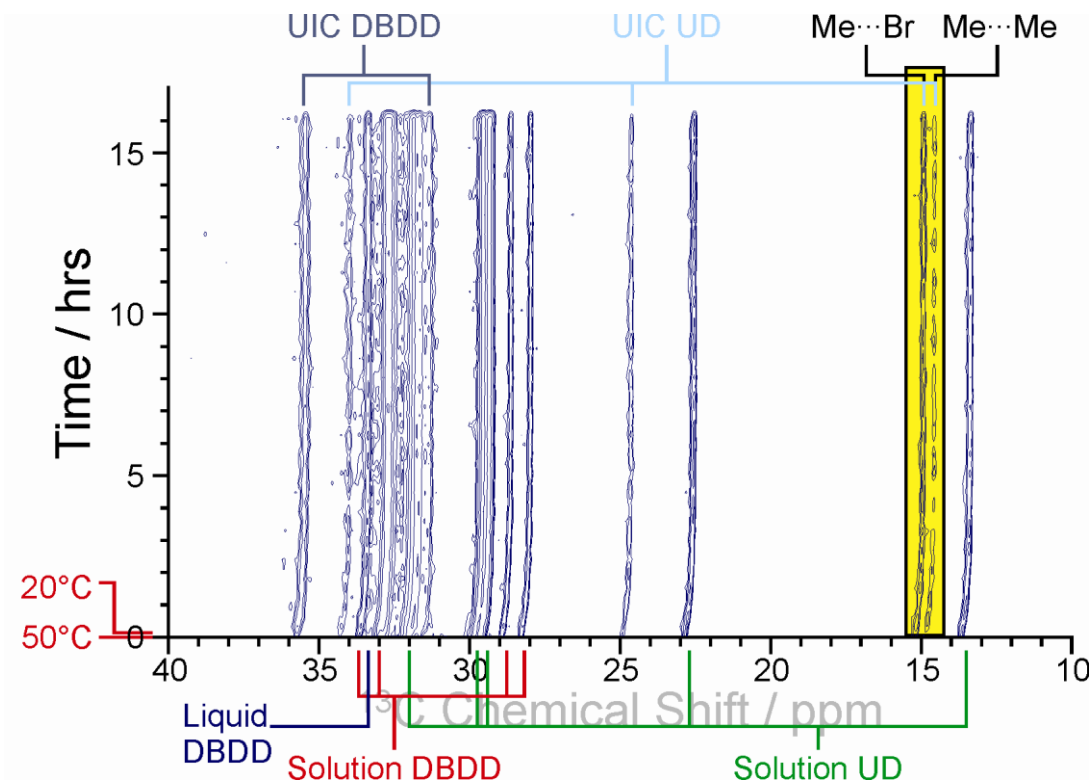
Fig. 5.50 *Time resolved HPDEC ^{13}C spectrum from 40ppm to 10ppm of the fast crystallization of 1,12-dibromododecane+undecane/urea (57% DBDD, 43% UD) in methanol. Only positive intensity is shown. Chemical shift (ppm) occupies the horizontal axis, time (hrs) occupies the vertical axis and the cooling period has been denoted on this axis. Liquid and solution peaks are labelled at the bottom of the spectrum, solid peaks are labelled at the top of the spectrum. The splitting of the methyl peak by neighbour environment is highlighted in yellow.*

Much like the fast crystallization of DBO + TD crystallization completes almost immediately and time evolution plots show few changes. Accordingly these plots have been omitted.

5.5 Conclusions

With our *in-situ* NMR technique we can:
- Determine when crystallization occurs.

- Distinguish between guests within the solid tunnel.

- Observe peak-splitting by the neighbour environment.

We can monitor signal in different phases to determine when crystallization occurs – as our urea inclusion compounds crystallize almost immediately in some of our fast cool experiments this suggests that there are no delays or lag times prior to crystallization. We can also gain insight on the differences between fast crystallization and slow crystallization. We can determine which guests are included inside the crystal and in what proportions, we can also observe splitting by neighbour environment and in principle we can use this to determine guest ordering within the crystal. We have not seen any evidence for guest exchange even though earlier experiments using Confocal Raman Microspectrometry have demonstrated the significance of these processes[1], showing that a DBO UIC can be replaced by pentadecane. Knowing that these processes occur we need to hypothesize why we are unable to observe them using our *in-situ* NMR setup and a couple of possibilities immediately come to mind – 1) Guest exchange occurs on a slower timescale than the experiments we were running, but we can eliminate this possibility as our longest NMR experiments were performed over an ~18 hour period (~6 hours post crystallization) and our 21 hour *in-situ* Raman experiments showed significant differences over the course of 3 hours, 2) Guest exchange occurs but our NMR setup is not sufficiently sensitive to detect these changes, however this seems unlikely as our Raman experiments show big differences that should have been detectable (in an *in-situ* exchange experiment a position on a starting crystal of 100% DBO UIC underwent exchange to become a 10% DBO / 90% pentadecane crystal), 3) Guest exchange occurs but doesn't result in any net change in crystal composition and this seems like the most likely explanation. Previously our Raman exchange experiments added a reservoir of guest to a pre-made crystal so there were was an injection of an abundant new guest, in these NMR experiments the molecules available for guest exchange are the same ones that were available during crystal growth. This suggests that the thermodynamically favoured guests are also kinetically favoured and are included more easily as the crystal is growing.

Experiments on the DBO+UD mixture fast crystallization were performed at 12 KHz, 8KHz and 4 KHz with no differences observed on the different spinning speeds. This suggests that the spinning is not having an effect on the crystallization process so our *in-situ* experiment is a valid representation of what occurs in the lab.

The fast and slow crystallizations of the same mixtures show slightly different guest compositions within the crystal. The slow crystallization of DBO+UD shows negligible DBO within the crystal but strong solution signals from DBO. The fast crystallization shows noticeable DBO within the crystal for solution signals of a similar strength. This suggests the uptake of DBO is greater in the fast crystallization than in the slow crystallization.

The $\underline{C}H_3$ signal is stronger than the $\underline{C}H_2CH_3$ in each of the alkanes, despite the fact that the populations must be equal. This shows us that the second carbon in the chain is less efficient for generating signal, suggesting that its relaxation processes are slower possibly because it has less rotational freedom. This may also apply to the $\underline{C}H_2Br$ carbon if we consider the Br as a carbon equivalent for chain length purposes.

The DBO+UD mixture shows little splitting of the methyl peak (Me-Me is much stronger than Me-Br) whilst the DBDD+UD mixture shows strong splitting of the methyl peak (Me-Me and Me-Br are roughly equal). This suggests ordered regions of guest within the DBO+UD mixed-guest UIC (Fig. 5.51) and an alternating pattern within the DBDD+UD mixed-guest (Fig. 5.52), but the ordering of the guests within the UIC is limited by the guest composition and in the DBO+UD we have little DBO. A random alternating pattern is entropically favoured so if an ordered region of guest occurs than that suggests an enthalpic driving force is overcoming entropy.
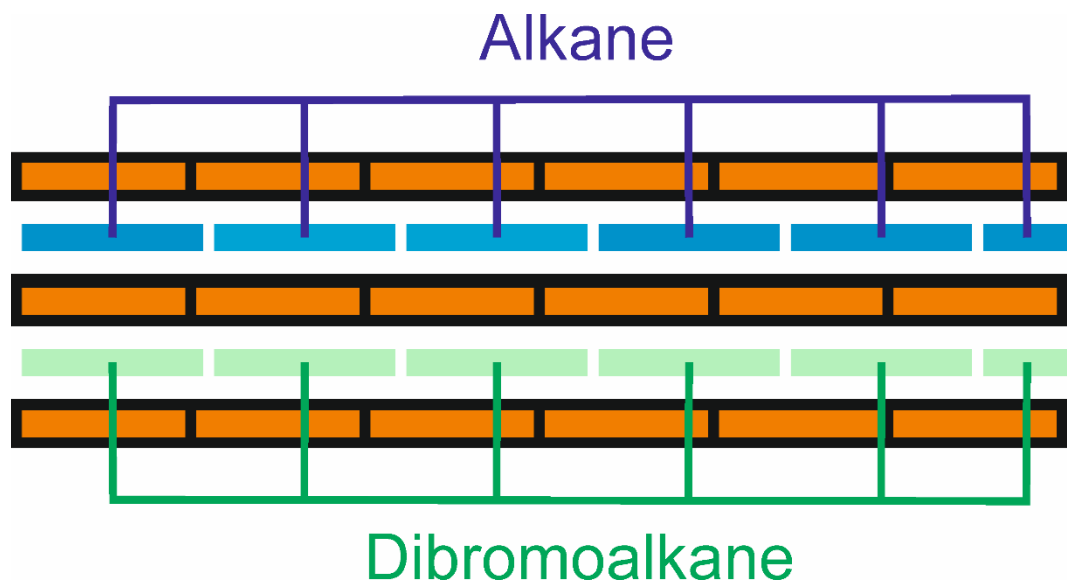
Fig. 5.51 *Schematic of a mixed guest UIC with ordered regions of guest. Interactions between the two different guest molecules are rare regardless of guest proportion because they only occur at the boundary between regions and not in the bulk.*
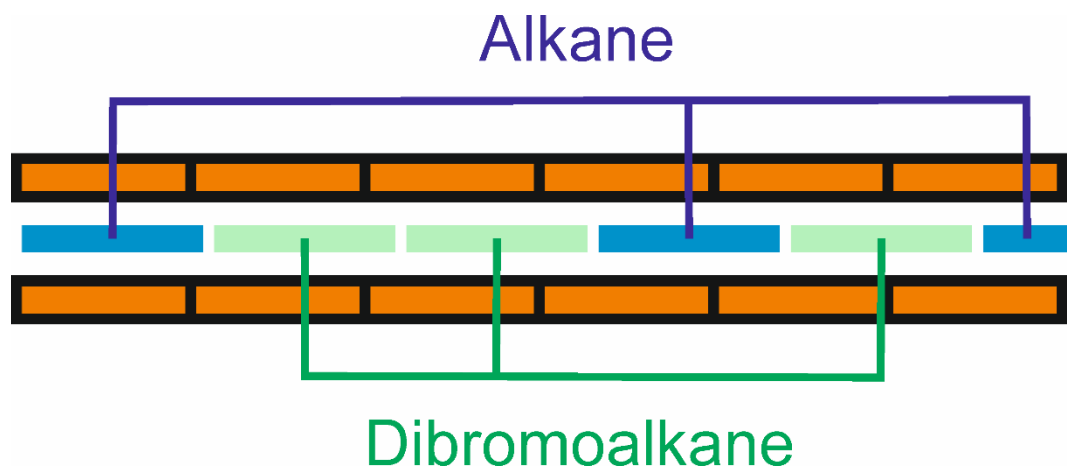
Fig. 5.52 *Schematic of a mixed guest UIC with a random arrangement of guests. Interactions between the two different guest molecules are common provided that both guests make up a similar proportion of the solid.*

It is also worth noting that urea inclusion compounds can be formed using a guest as a solvent rather than using methanol to dissolve everything. This is not the typical method to produce urea inclusion compounds so we decided against trying it for our initial

experiments, but without methanol in the system we might be able to have higher guest concentrations so it is an avenue worth exploring when trying to optimize future experiments.

5.6 References

[1]   J. Marti-Rujas, A. Desmedt, K. D. M. Harris, F. Guillaume, *J. Phys. Chem. C*, **2009**, 113(2), 736-743.

[2]   C. E. Hughes, K. D. M. Harris , *J. Phys. Chem. A* **2008**, 112(30), 6808-6810

[3]   C. E. Hughes, K. D. M. Harris , *J. Phys. Chem. Lett.* **2012**, 3(21), 3176-3181

[4]   C. E. Hughes, P. A. Williams, K. D. M. Harris , *Angew Chemie Int Ed.* **2014**, 53(34), 8939-43.

[5]   D. L. Bryce, G. M Bernard, M. Gee, M. D. Lumsden, K Eichele, R. E. Wasylishen, *Can. J. Anal. Sci. Spect.* **2001**, 46, 46-82.

[6]   W. Kolodziejski, A. Corma, K Wozniak, J. Klinowski, *J. Phys. Chem.* **1996**, 100, 7345-7351.

[7]   R. K. Harris, *Analyst*, **2006**,131, 351-373.

[8]   M. J. Duer, *Introduction to Solid-State NMR Spectroscopy*, **2004**, Blackwell Publishing Ltd., Oxford.

Chapter 6 - New Co-Crystals Obtained by Reactions of α,ω-Diiodoalkanes and Thiourea

6.1 Introduction

Thiourea is known to form inclusion compounds with bulky alkane derivatives but crystallizing thiourea with α,ω-diiodoalkanes was found to produce a reaction co-crystal rather than the standard inclusion compound. This chapter reports the reactions of: 1,4-diiodobutane + thiourea; 1,5-diiodopentane + thiourea; 1,6-diiodohexane + thiourea; 1,8-diiodooctane + thiourea; 1,10-diiododecane + thiourea to give co-crystals in the series $(H_2N)_2CS^+(CH_2)_nS^+C(NH_2)_2 + (H_2N)_2CS + I^-$.

The aim of these experiments was to prepare thiourea inclusion compounds with iodoalkane guests. Thiourea typically does not form inclusion compounds with straight chain alkanes but we decided to investigate whether the iodine end group was sufficiently bulky that it would allow a thiourea inclusion compound to form. Additionally, experiments crystallizing α,ω-diiodoalkanes alongside urea produced some urea inclusion compounds with a commensurate host-guest relationship. However, crystallizing α,ω-diiodoalkanes alongside thiourea did not give rise to an inclusion compound and instead the solid obtained was the product of a chemical reaction. Reactions where sulphur replaces iodine are uncommon, but they are not unknown and they have occasionally been reported in the literature[1-3]. However reactions with these particular starting materials and conditions had not been previously observed and the co-crystals structures are new. A general reaction scheme is shown in Fig. 6.1.
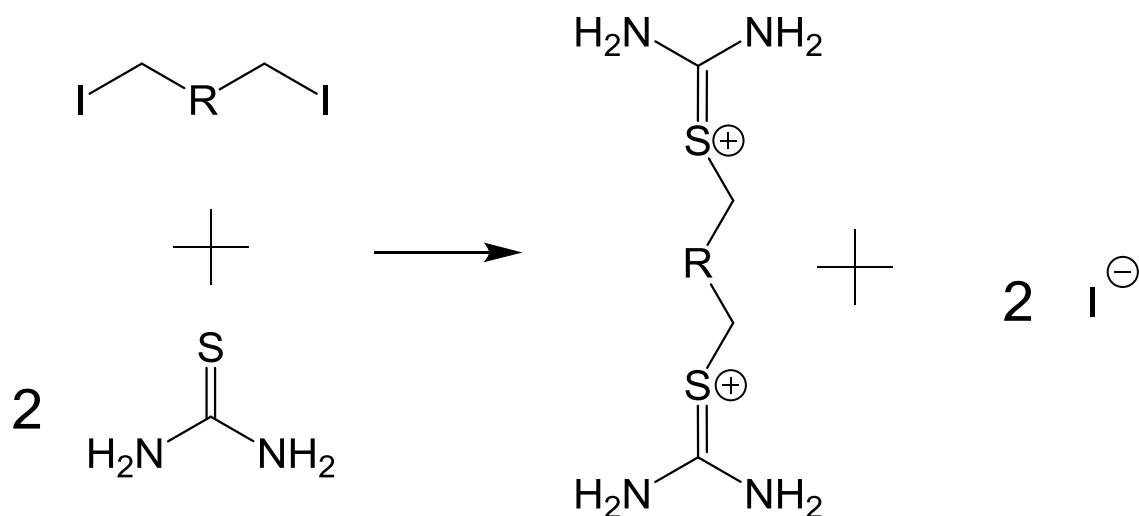
Fig. 6.1 *General scheme for the reaction that occurs during the production of these co-crystals.*

6.2 Experimental

The 1,4-diiodobutane + thiourea reaction co-crystal, 1,5-diiodopentane + thiourea reaction co-crystal, 1,8-diiodooctane + thiourea reaction co-crystal and 1,10-diiododecane + thiourea reaction co-crystal were prepared by dissolving thiourea (5 mmol) and the α,ω-diiodoalkane guest (1.5 mmol) in a mixture of methanol (4 ml) and 2-methyl-2-butanol (1 ml) at 55°C. The resulting solution was incubated at 55°C for 1hr, cooled to 25°C at a rate of 0.03°C/min and then left to slowly evaporate at room temperature over the course of a week. Colourless crystals were produced and investigated by single crystal XRD.

The 1,6-diiodohexane + thiourea reaction co-crystal was prepared by dissolving thiourea (0.5 mmol) and the 1,6-diiodoalkane (0.15 mmol) in a mixture of ethanol (2 ml) and 2-methyl-2-butanol (1.2 ml) at 55°C. The resulting solution was crash cooled to 10°C for 10 minutes, allowed to equilibrate back to 25°C and then left to slowly evaporate at room temperature over the course of a week. Colourless crystals were produced and investigated by single crystal XRD. Dissolving 1,6-diiodohexane + thiourea in methanol gave the same chemical product but with extremely small crystallites that were not suitable for routine single crystal XRD.

For structure determination single crystal XRD data were collected on a Nonius Kappa CCD diffractometer using graphite monochromated Mo Kα radiation ($\lambda = 0.71073$ Å) and equipped with an Oxford Cryosystems cooling apparatus. Data were recorded at 296 K for the materials prepared for the shorter α,ω-diiodoalkanes $(H_2N)_2CS^+(CH_2)_nS^+C(NH_2)_2$ n = 4, 5, 6 and at 150K for $n = 8$ and 10. The structures were solved using direct methods and refined with SHELX-97[4]. Non-hydrogen atoms were refined anisotropically and hydrogen atoms were inserted in idealised positions and a riding model used with U_{iso} set at 1.2 times the U_{eq} of the parent atom.

6.3 Results

The co-crystals created from the product of the reaction of the α,ω-diiodoalkane and thiourea are all made up of similar molecules but their crystal structures show notable differences. In each case the α,ω–diiodoalkane reacts to give carbon chains capped with $SC(NH_2)_2$ groups at both ends of the alkyl chains (ie, to form $(H_2N)_2CS^+(CH_2)_nS^+C(NH_2)_2$), along with unreacted thiourea and the liberated iodide ions. In the cases with n = 6, 8 and 10 the alkane molecules are stacked parallel to each other, but in the material with n = 4 adjacent alkanes are oriented opposite each other to give anti-parallel stacks. In the materials with n = 4, 8 and 10 there is one iodide site in the unit cell but in the material with n = 6 there are two similar-but-distinct iodide sites. This section contains tabulated data for the four different products, followed by the structures themselves. In the tables the length of the alkane chain in the $(H_2N)_2CS^+(CH_2)_nS^+C(NH_2)_2$ unit is used to identify the material i.e., the reaction co-crystal of 1,4-diiodobutane and thiourea gives $(H_2N)_2CS^+(CH_2)_4S^+C(NH_2)_2$ and is referred to as n = 4.

6.3.1 Structures of Even Chain Length Co-Crystals

The co-crystals with short alkane chains with an even number of carbons have long and thin unit cells but this gets less pronounced as chain length increases and the longest chain length alkane has similar lengths for all sides of the unit cell. The space group also changes across the series of materials, the n = 4 product gives an orthorhombic space group (*Pbca*), the n = 6 product gives monoclinic space group (*P2₁/n*) and the n = 8 and n = 10 and decane products give triclinic space groups ($P\bar{1}$). These unit cell parameters are summarized in Table 1. More complete data is included in 6.3.3 Structure Data Tables and the CIF files are available in the digital data. Crystal structures for the four materials are shown in Figs 6.2-6.5.

Unit Cell Parameters				
	n=4	**n=6**	**n=8**	**n=10**
Space group	*Pbca*	$P12_1/n1$ ($P2_1/c$)	$P\bar{1}$	$P\bar{1}$
a/Å	11.3617(6)	5.9789(1)	6.0463(2)	8.7877(3)
b/Å	8.4283(4)	15.2850(6)	8.4495(3)	9.4753(3)
c/Å	23.0579(11)	22.0067(8)	12.7157(6)	9.6865(5)
α/°	90	90	87.970(2)	105.673(2)
β/°	90	91.459(2)	80.012(2)	112.177(2)
γ/°	90	90	85.108(2)	100.130(2)
V/Å³	2208.02(19)	2010.48(11)	637.31(4)	683.31(5)
Z	4	4	1	2

Table 1 Unit cell parameters for the four materials produced.
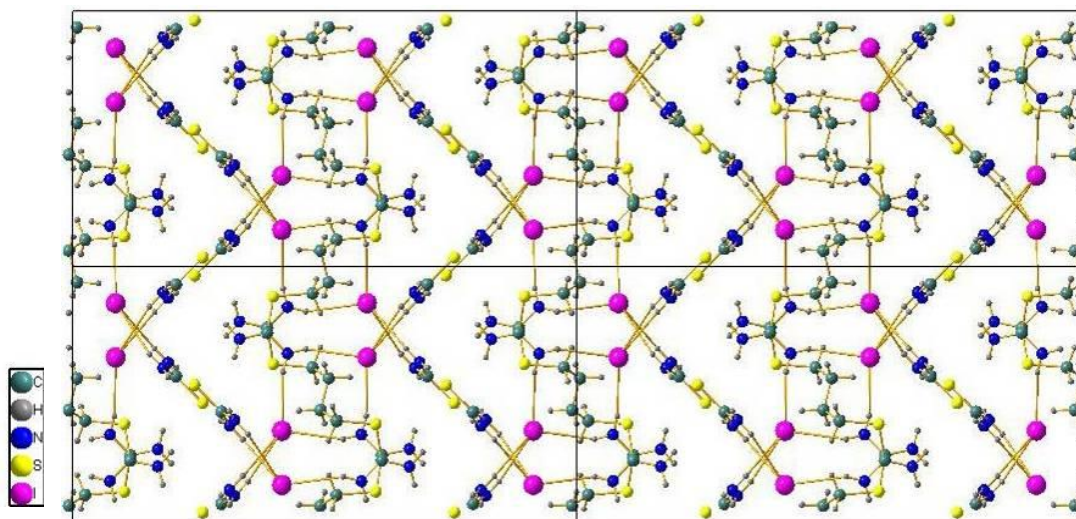
Fig. 6.2 Structure of the n = 4 material viewed along the b axis with the a axis vertical and the c axis horizontal.
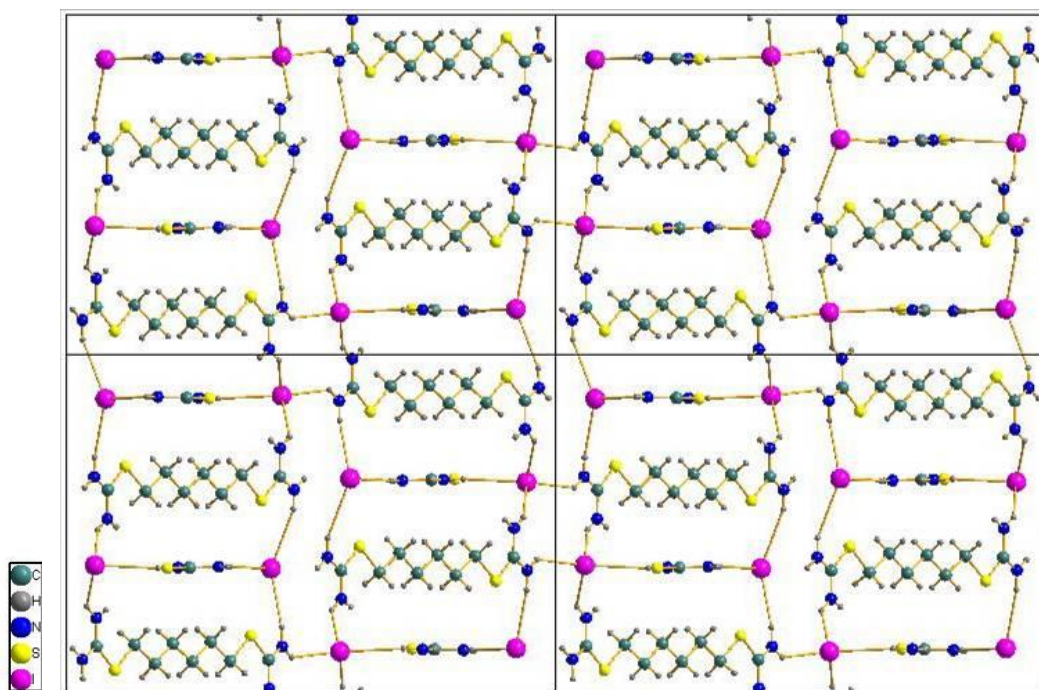
Fig. 6.3 *Structure of the n = 6 material, viewed along the a axis with the b axis vertical and the c axis horizontal.*
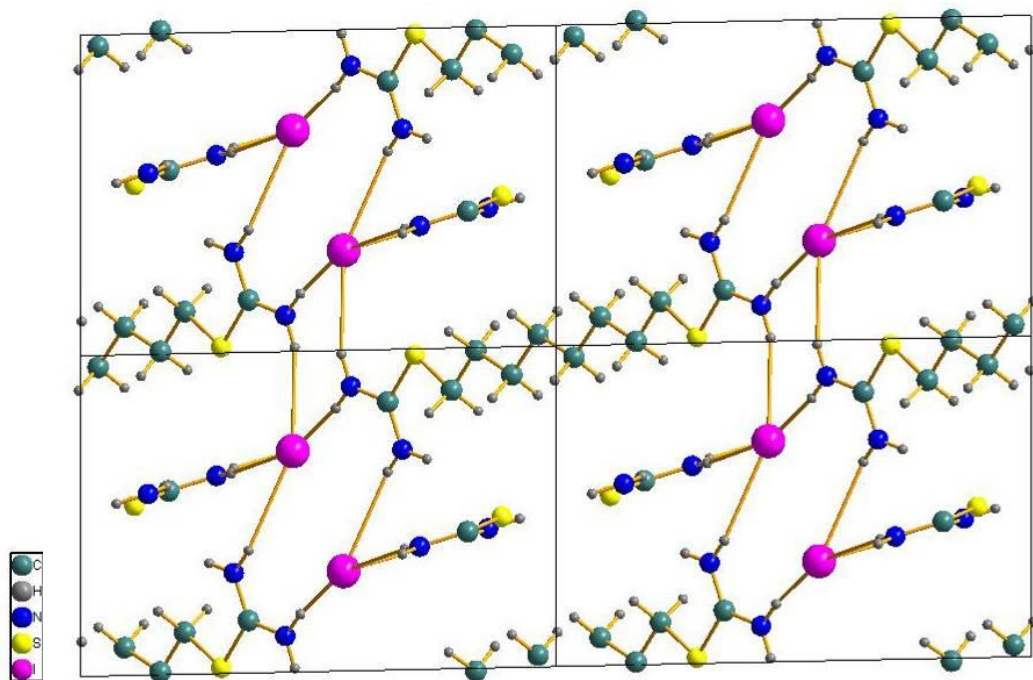
Fig. 6.4 *Structure of the n = 8 material, viewed along the a axis with the b axis vertical and the c axis horizontal.*
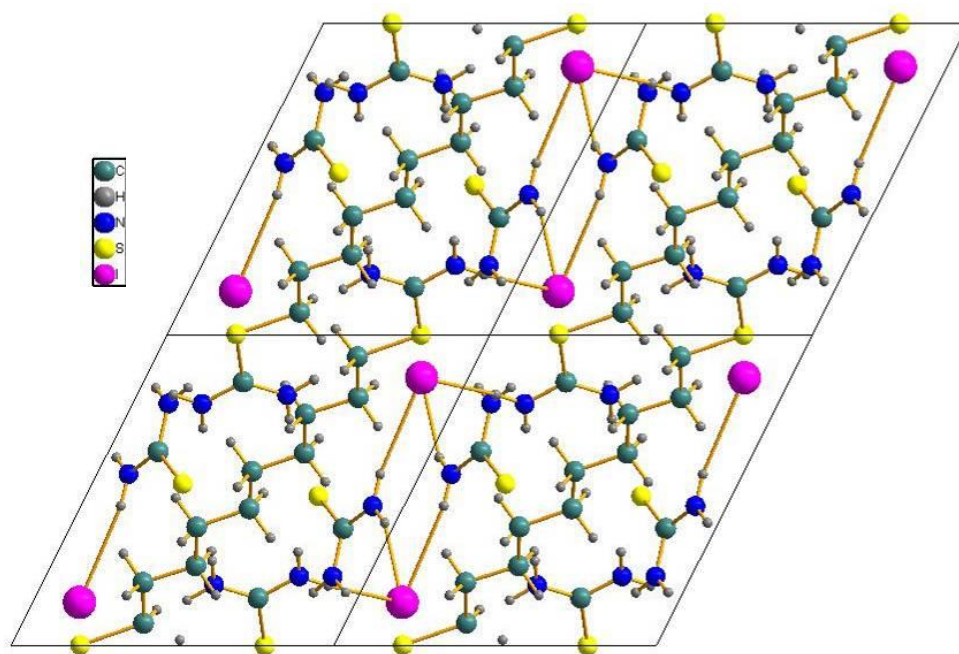
Fig. 6.5 *Structure of the n = 10 material, viewed along the b axis with the a axis horizontal vertical and the c axis diagonal.*

The shorter chains (n = 4 and n = 6) have 4 alkane molecules in the unit cell whilst the longer chains (n = 8 and n = 10) have 1 alkane molecule in the unit cell. Typically the structures have a 4:1 thiourea:alkane ratio but the 1,6-diiodohexane + thiourea reaction co-crystal shows a 3:1 thiourea:alkane ratio. The bound thiourea is always co-planar with the alkane chain (aligned), but the free thiourea is perpendicular to it. Additionally the 1,6-diiodohexane + thiourea reaction co-crystal has two independent iodine sites in the unit cell whereas the others have only one iodine site. The contents of the unit cells are summarized in Table 2.

Unit Cell Contents and Characteristics				
	n = 4	**n = 6**	**n = 8**	**n = 10**
Content				
-Iodide	8	8	2	2
-Alkane chain	4	4	1	1
-Thiourea	16 (4:1 vs. alkane)	12 (3:1 vs. alkane)	4 (4:1 vs. alkane)	4 (4:1 vs. alkane)
-B-Thiourea	8	8	2	2
-F-Thiourea	8	4	2	2
Iodide sites	1	2	1	1
I^-----H−N contacts	4 per iodide	1) 4 per iodide 2) 4 per iodide	5 per iodide	3 per iodide
Thiourea orientation relative to alkane				
-Aligned	8	8	2	2
-Perpendicular	8	4	2	2

***Table 2** Unit cell contents and characteristics for the four materials produced.*

In each structure I^-----H−N contacts are the only type of close contacts formed by iodide. The n = 4 iodide site and both n = 6 iodide sites have 4 close contacts per iodine, but the iodide in the n = 8 structure has 5 and the iodide in the n = 10 has 3 close contacts. The I^-----H contacts range from 2.7160 Å to 2.9575 Å without any apparent trends with chain length and the I^-----H−N angle is usually around 160° but in extreme cases can be significantly higher (175°) or lower (138°). This information is summarized in Tables 3 and 4, and interpreting this data suggests that the structures do not exhibit strong hydrogen bonding: the I^-----H distance is longer than a strong hydrogen bond (1.5-2.5 Å), the I^-----H−N angle varies significantly but is usually far away from 180° and the number of I^-----H contacts is not dependent on the number of lone pairs on the iodide. This suggests that in these structures the intermolecular interactions between iodine and hydrogen are primarily

electrostatic rather than covalent and the structure is not being dictated by hydrogen bonding.

I⁻····H−N Contacts					
	n = 4		n = 6 (site 1)		n = 6 (site 2)	
	I⁻····H / Å	I⁻····H−N/°	I⁻····H / Å	I⁻····H−N/°	I⁻····H / Å	I⁻····H−N/°
1	2.7220	167.277	2.7448	138.257	2.8080	165.476
2	2.8725	149.66	2.7538	143.244	2.9144	159.908
3	2.9272	158.157	2.7540	153.023	2.9239	162.744
4	2.9575	156.413	2.8667	175.450	2.9560	174.719

Table 3 I^-····H contact distances and I^-····H−N angles for the n = 4 and n = 6 materials. H atoms are in calculated positions so no e.s.d.s are unavailable.

I⁻····H−N Contacts				
	n = 8		n = 10	
	I⁻····H / Å	I⁻····H−N / °	I⁻····H / Å	I⁻····H−N / °
1	2.7160	162.015	2.8414	157.799
2	2.7454	175.370	2.8523	160.369
3	2.7761	159.267	2.8664	159.912
4	2.8578	144.159	-	-
5	2.8777	168.509	-	-

Table 4 I^-····H contact distances and I^-····H−N angles for the n = 8 and n = 10 materials. H atoms are in calculated positions so no e.s.d.s are unavailable.

The C−S bond lengths also fail to show any significant trends with chain length but it is interesting to observe the differences between the three different types of C−S bond within a given material (see Fig. 6.6). The length of the bond between the alkane

chain carbon and the sulphur (~1.81 Å) is consistently longer than the bond length between the sulphur and the reacted thiourea carbon (~1.73 Å) which in turn is consistently longer than the C−S bond length for unreacted thiourea (~1.70 Å) as shown in Table 5. As the reacted bond distances are only slightly longer than the unreacted material it shows bonds have been formed rather than intermolecular interactions, and as the bound thiourea retains a similar C−S bond length to the free thiourea it suggests much C=S double bond character – i.e. with the charge on the S rather than the C. The C−S−C bond angles are around 103.5°, with little variation (102.1(3)° to 105.4(3)°) as shown in Table 6. This description of the structure places a formal positive charge on the sulphur, balanced by a formal negative charge on the iodide. Additionally, the reacted thiourea molecules capping the alkane chains are in the same plane as the reacted "guest" molecules, but the unreacted thiourea molecules are nearly perpendicular to this plane.
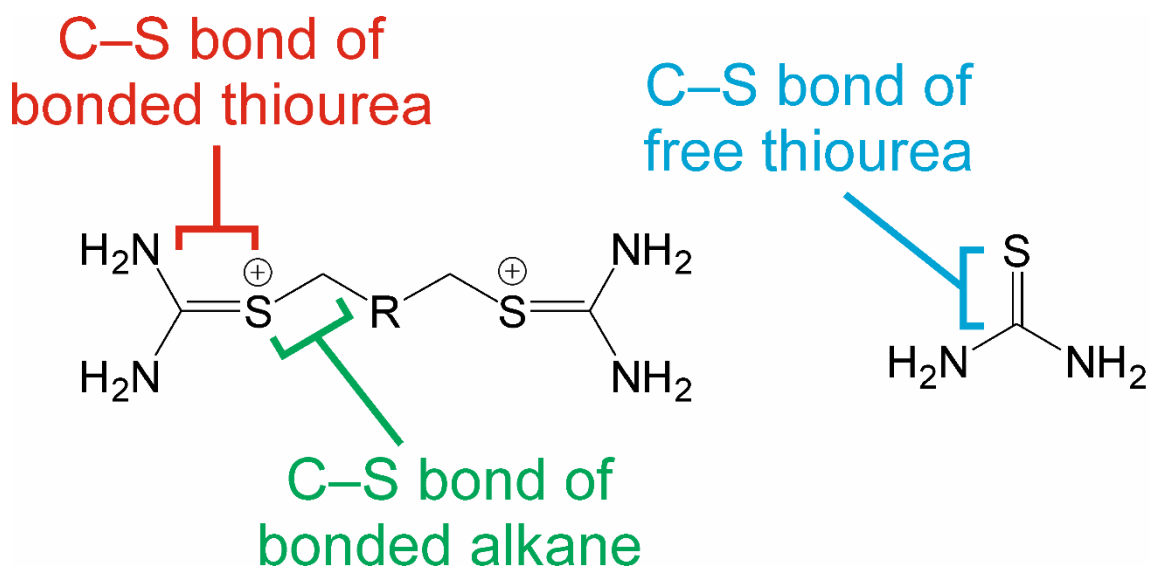
Fig. 6.6 *Schematic of the three different types of C−S bond present in each material.*

C−S Bond Distances				
	n = 4	n = 6	n = 8	n = 10
Free Thiourea / Å	1.7185(54)	1.6984(64)	1.7053(38)	1.7058(48)
Bound-Thiourea / Å	1.7309(70)	1.7268(70)	1.7377(32)	1.7461(59)
Alkane / Å	1.8140(71)	1.8099(64)	1.8181(33)	1.8143(76)
BThiourea/Thiourea %	100.72%	101.67%	101.90%	102.36%
Alkane/Thiourea %	105.56%	106.57%	106.61%	106.36%

Table 5 *Table of C−S bond lengths of free thiourea, bound thiourea and bonded alkane (see Fig. 6.6) in the four different structures. Comparison of these different bond lengths within the same structure shows us that the C−S bond in bonded thiourea is approximately 1-2% longer than non-bonded thiourea, and the alkane sulphur C−S bond distances are approximately 6-7% longer than non-bonded thiourea.*

C−S−C Bond Angles				
	n = 4	n = 6	n = 8	n = 10
C−S−C Angle	105.4(3)°	102.1(3)° 103.2(3)°	103.89(15)°	103.0(2)°

Table 6 *Table of C−S−C bond angles in the four different materials.*

Figs 6.7, 6.9, 6.11, and 6.13 show only the alkane chains within the crystal structures for the sake of clarity. Note the anti-parallel stacking of the alkane in the butane and hexane materials and the parallel alkane stacking in the octane and decane materials. Figs 6.8, 6.10, 6.12, and 6.14 show only the thiourea units within the crystal structures for the sake of clarity, but with bonded thiourea including the attachment site on the alkane chain.
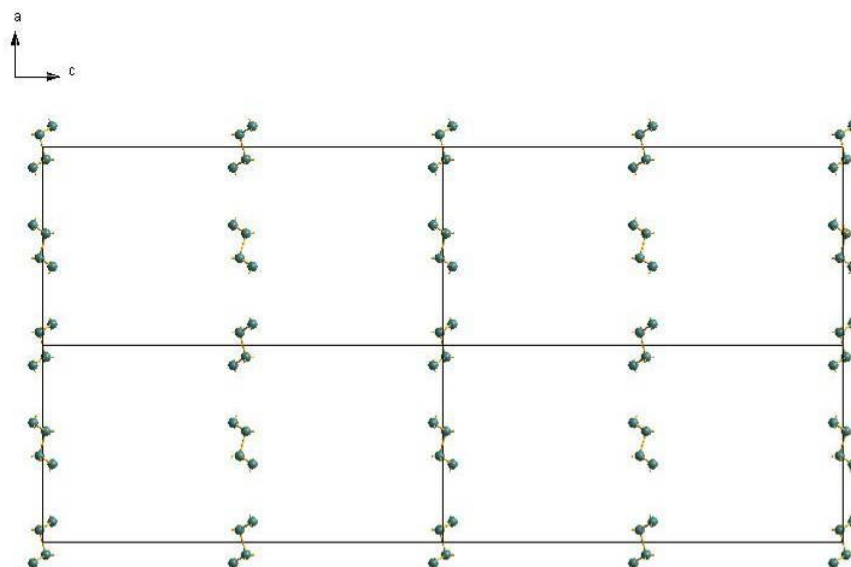
Fig. 6.7 *Structure of the n = 4 material, viewed along the b axis with the a axis vertical and the c axis horizontal, but showing only the alkane molecules.*
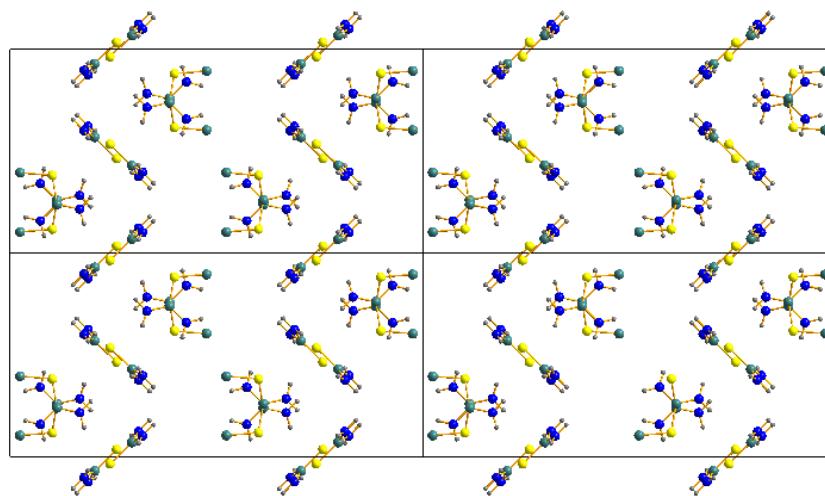
Fig. 6.8 *Structure of the n = 4 material, viewed along the b axis with the a axis vertical and the c axis horizontal, but showing only the thiourea units.*

Fig. 6.9 *Structure of the n = 6 material, viewed along the a axis with the b axis vertical and the c axis horizontal, but showing only the alkane molecules.*
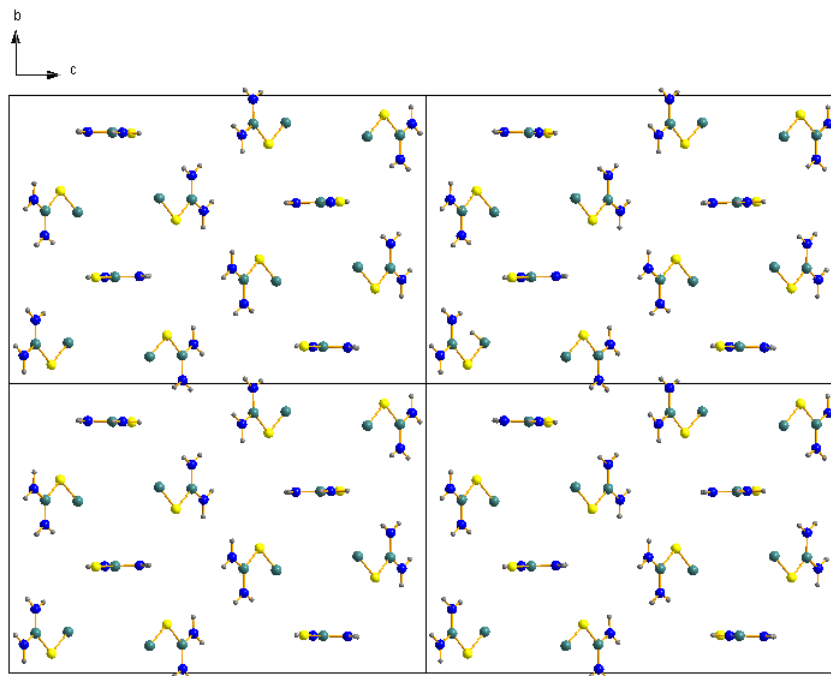
Fig. 6.10 *Structure of the n = 6 material, viewed along the a axis with the b axis vertical and the c axis horizontal, but showing only the thiourea units.*
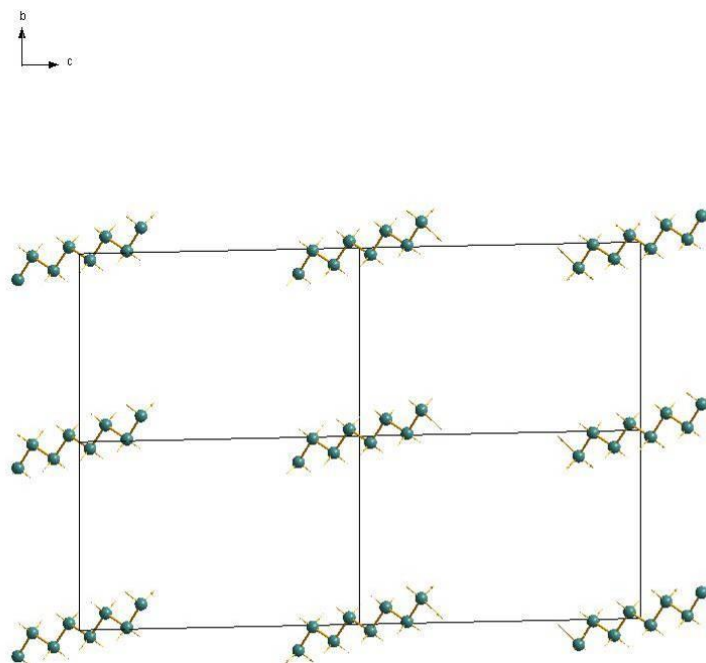
Fig. 6.11 *Structure of the n = 8 material, viewed along the a axis with the b axis vertical and the c axis horizontal, but showing only the alkane molecules.*
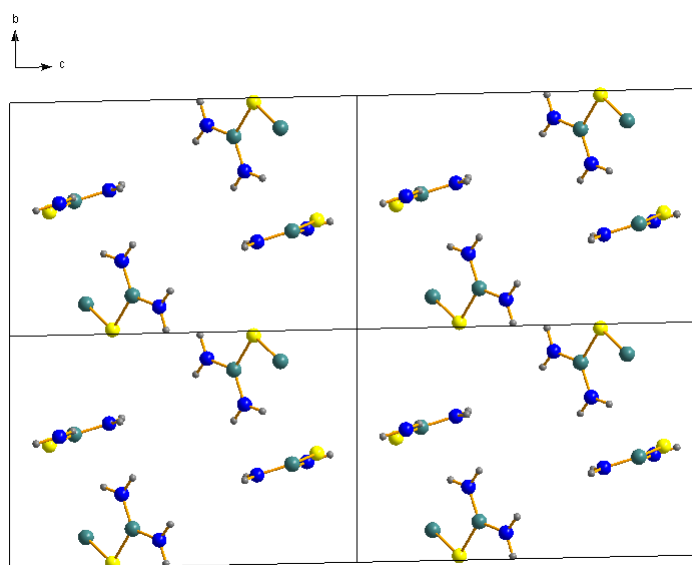
Fig. 6.12 *Structure of the n = 8 material, viewed along the a axis with the b axis vertical and the c axis horizontal, but showing only the thiourea units.*
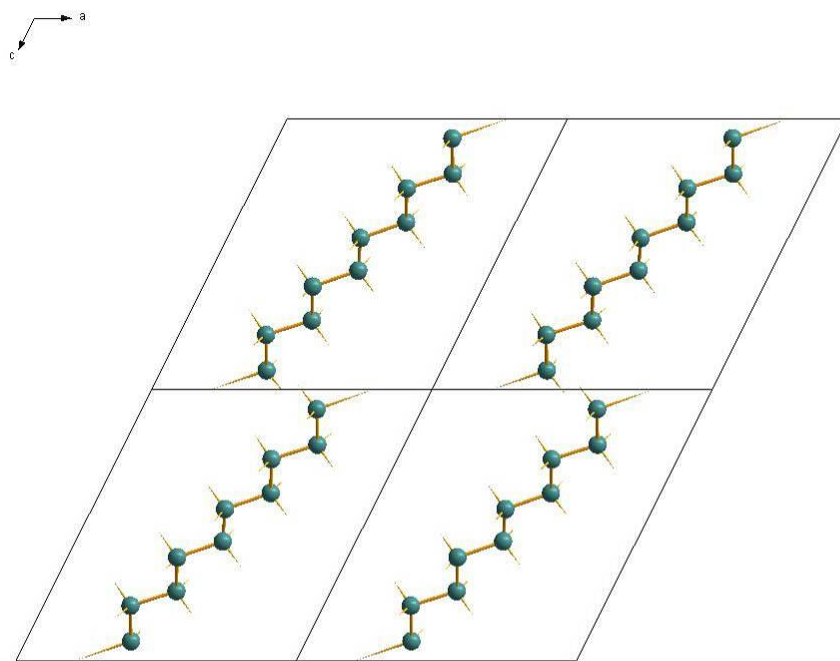
Fig. 6.13 *Structure of the n = 10 material, viewed along the b axis with the a axis horizontal and the c axis diagonal, but showing only the alkane molecules.*
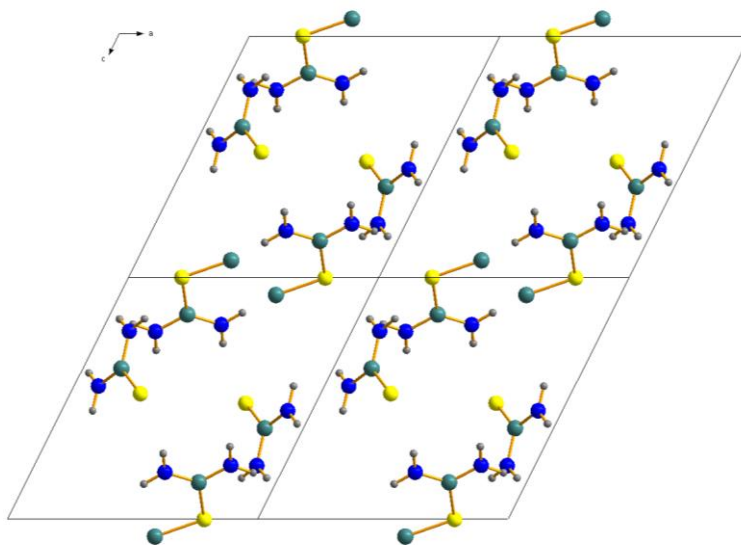
Fig. 6.14 *Structure of the n = 10 material, viewed along the b axis with the a axis horizontal and the c axis diagonal, but showing only the thiourea units.*

In each case the distance between identical guest positions is equal to the size of the unit cell, however, there may be similar positions partway along the unit cell and the distances between these positions are summarized in Table 7. Figs 6.11-14 show these distances on the guest only crystal structures.

Alkane-Alkane Distances				
	n = 4	n = 6	n = 8	n = 10
a repeat / Å	11.3617	5.9789	6.0463	8.7877
b repeat / Å	8.4283	15.2850	8.4495	9.4753
c repeat / Å	23.0579	22.0067	12.7157	9.6865
other b repeat / Å	5.3563	6.9269 7.5643	-	-
other c repeat / Å	11.6079 11.8658	11.3730 11.7871	-	-
close contact / Å	-	-	-	4.6353

Table 7 table of alkane-alkane distances
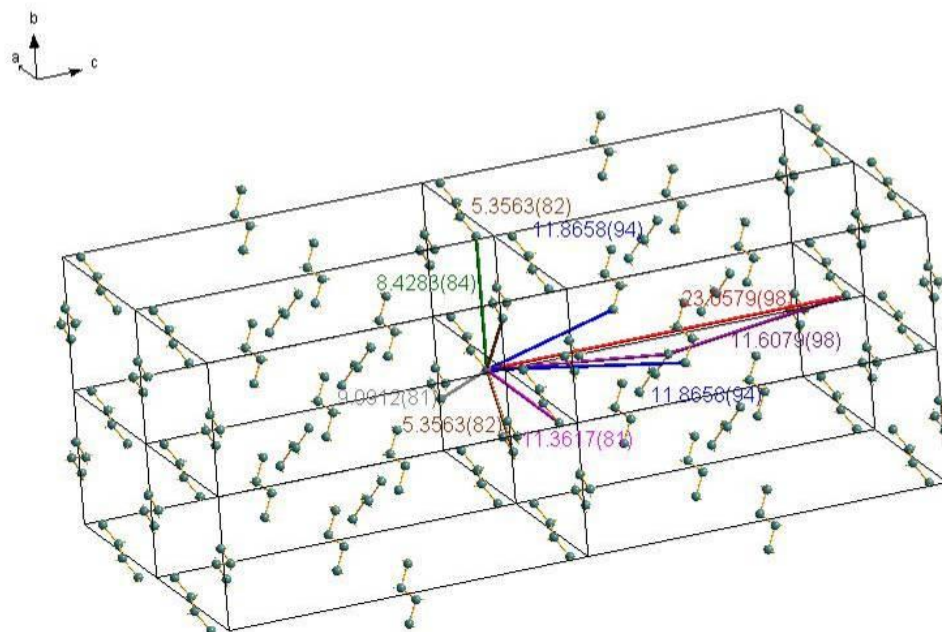
Fig. 6.15 *Structure of the n = 4 material showing only the alkane molecules and with alkane-alkane distances marked.*

142
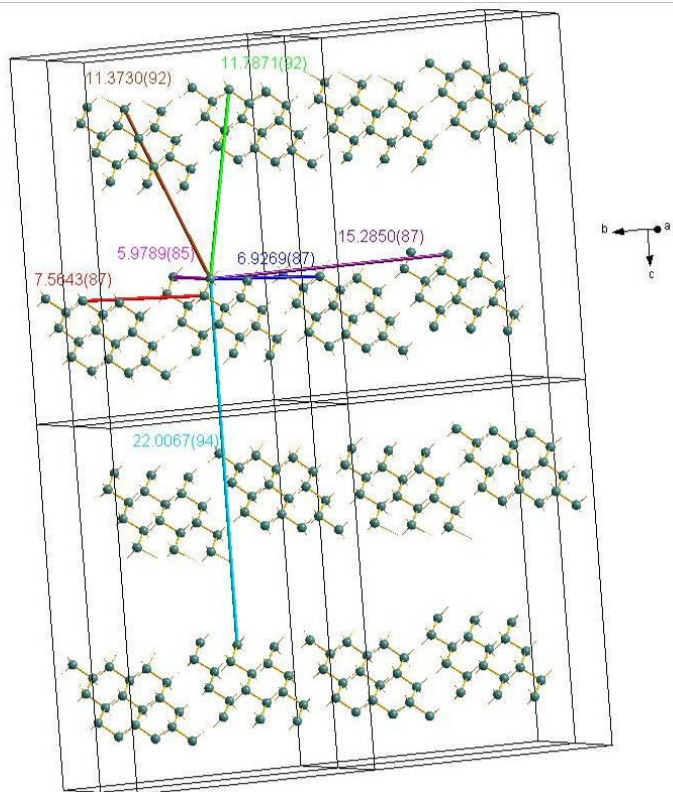
Fig. 6.16 *Structure of the n = 6 material showing only the alkane molecules and with alkane-alkane distances marked.*
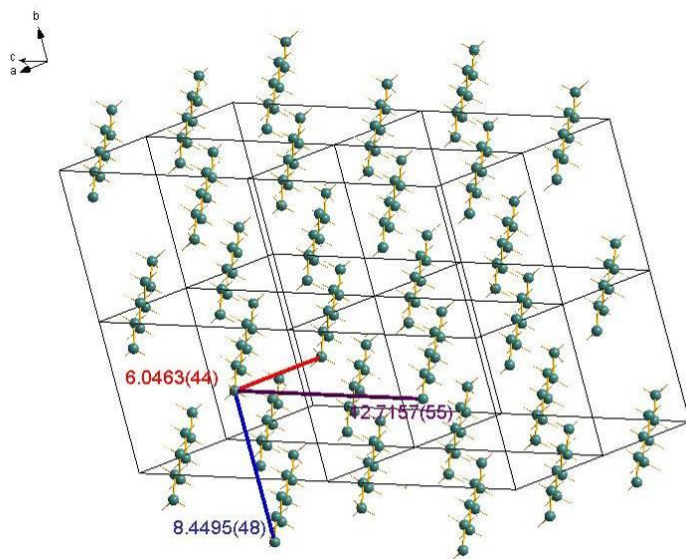
Fig. 6.17 *Structure of the n = 8 material, showing only alkane molecules and with alkane-alkane distances marked.*
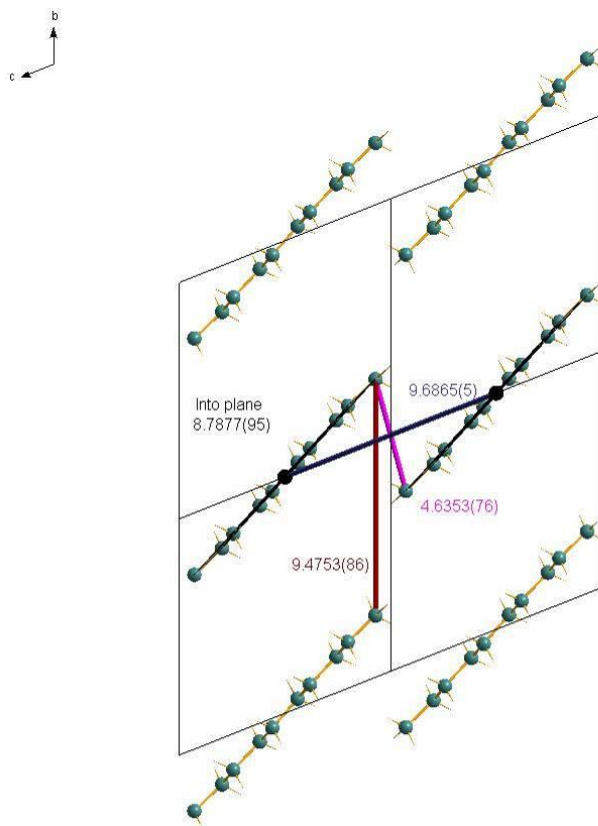
Fig. 6.18 *Structure of the n = 10 material, showing only alkane molecules and with alkane-alkane distances marked.*

6.3.2 Structures of Odd Chain Length Co-Crystals

The structure of the co-crystal formed by reacting 1,5-diiodopentane with thiourea is shown in Fig. 6.19 and Fig. 6.20. This material shows the biggest differences with regard to the other structures and it is very likely that the odd chain length is responsible. The co-crystal structure gives a monoclinic space group $P2_1/c$ with the unit cell dimensions $a = 7.6126(3)$ Å, $b = 22.5949(5)$ Å, $c = 9.0534(3)$ Å, $\beta = 90.303(2)°$. More complete structural information is available in 6.3.3 Structure Data Tables and the CIF file is available in the digital data.
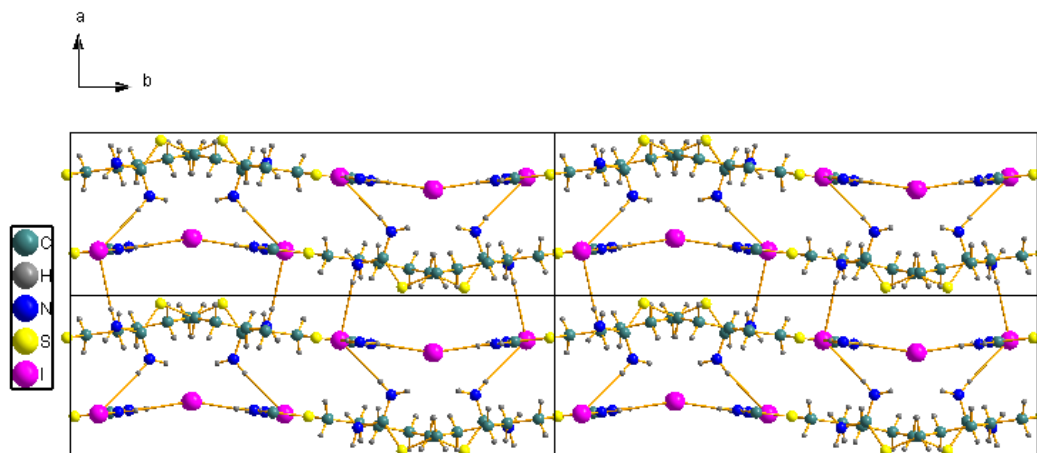
Fig. 6.19 Structure of the n = 5 material, viewed along the c axis with the a axis vertical and the b axis horizontal.
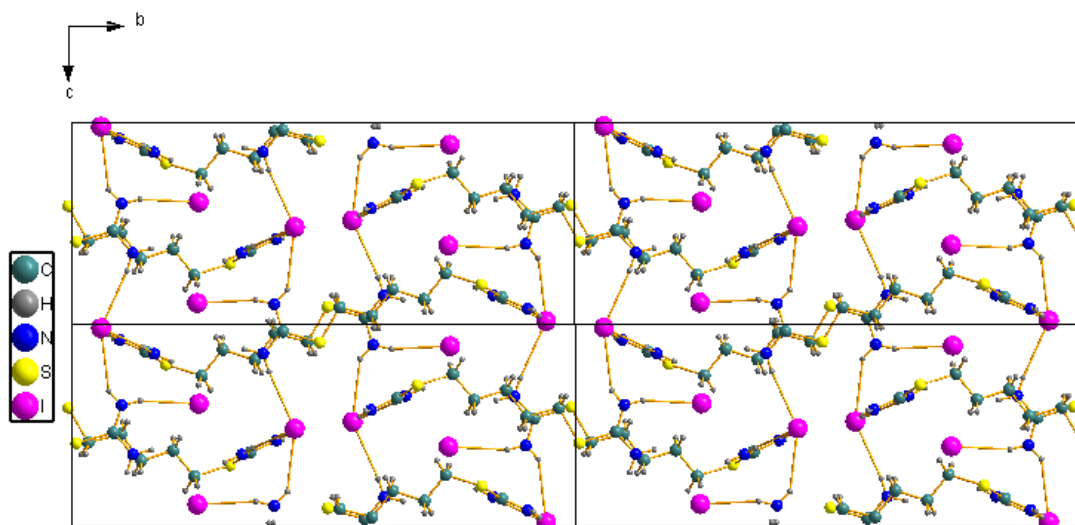
Fig. 6.20 Structure of the n = 5 material, viewed along the a axis with the c axis vertical and the b axis horizontal.

The unit cell contains eight iodide ions and four $(H_2N)_2CS^+(CH_2)_5S^+C(NH_2)_2$ molecules, note that unlike the even chain length co-crystals all the thiourea has reacted in this material. This means there are no free thiourea molecules to compare bond distances with but still we see a difference in C−S bond lengths of the bound thiourea

145

(1.739 Å) and the alkane C−S (1.815 Å). Again this suggests the bound thiourea retains much of its double bond character. Also note that this material has the highest density of these structures (n = 4 has 1.848 g/cm^3, n = 5 has 2.031 g/cm^3, n = 6 has 1.871 g/cm^3, n = 8 has 1.747 g/cm^3, n = 10 has 1.698 g/cm^3), because the absence of any unreacted thiourea space units allows the heavy iodine atoms to be packed more densely.

Figs 6.21 shows only the alkane within this material and illustrate the anti-parallel stacking of the pentane molecules. Fig. 6.22 shows only the thiourea units and demonstrates how all the thiourea has reacted.
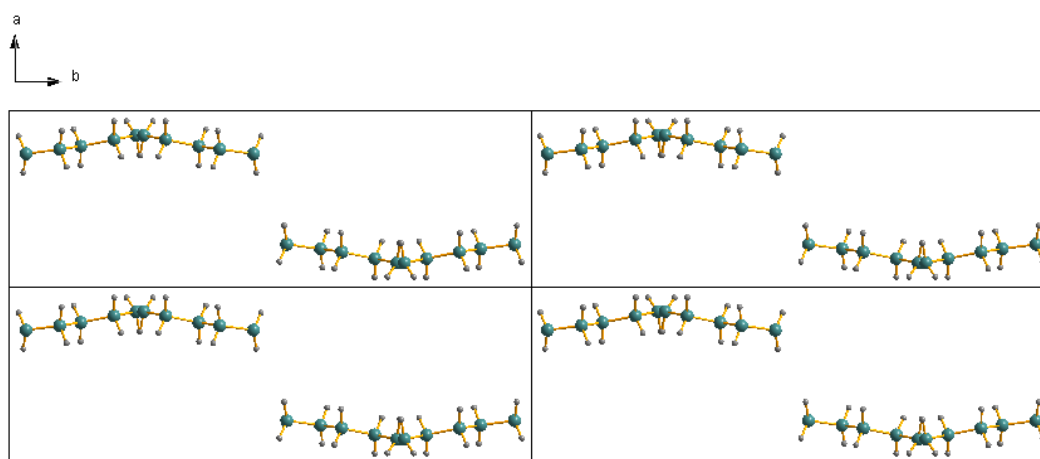
Fig. 6.21 *Structure of the n = 5 material, viewed along the c axis with the a axis vertical and the c axis horizontal, but showing only the alkane molecules.*
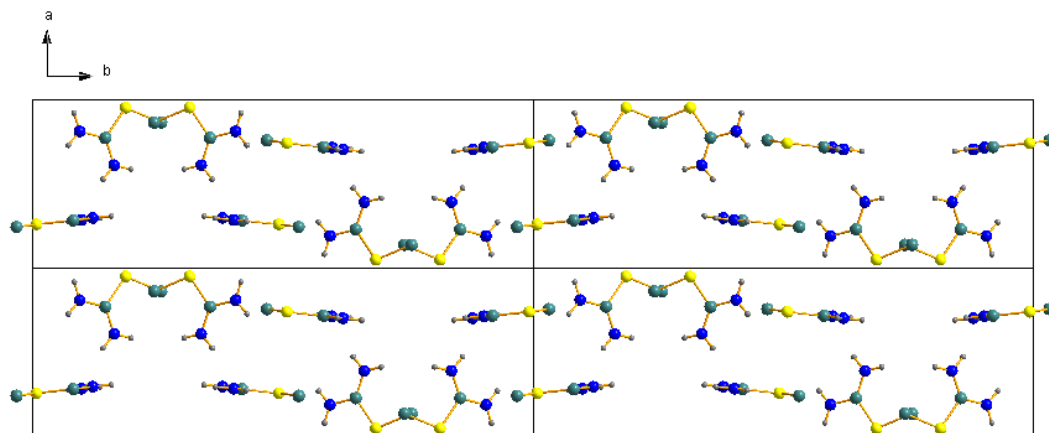
Fig. 6.22 *Structure of the n = 5 material, viewed along the c axis with a axis vertical and c axis horizontal, but showing only the thiourea units.*

6.3.3 Structure Data Tables

Material	Butane + Thiourea	
Empirical formula	C4 H12 I N4 S2	
Formula weight	614.39	
Temperature	296(2) K	
Wavelength	0.71073 Å	
Crystal system	Orthorhombic	
Space group	*Pbca*	
Unit cell dimensions	a = 11.3617(6) Å	$\alpha = 90°$.
	b = 8.4283(4) Å	$\beta = 90°$.
	c = 23.0579(11) Å	$\gamma = 90°$.
Volume	2208.02(19) Å^3	
Z	4	
Density (calculated)	1.848 g/cm^3	
Absorption coefficient	3.234 mm^{-1}	
F(000)	1192	
Crystal size	0.30 x 0.30 x 0.30 mm^3	
Theta range for data collection	2.52 to 28.72°.	
Index ranges	-9<=h<=15, -11<=k<=10, -24<=l<=30	
Reflections collected	8144	
Independent reflections	2598 [R(int) = 0.0432]	
Completeness to theta = 28.72°	90.8 %	
Absorption correction	Empirical	
Max. and min. transmission	0.4437 and 0.4437	
Refinement method	Full-matrix least-squares on F^2	
Data / restraints / parameters	2598 / 0 / 101	
Goodness-of-fit on F^2	1.098	
Final R indices [I>2sigma(I)]	R1 = 0.0558, wR2 = 0.1516	
R indices (all data)	R1 = 0.0711, wR2 = 0.1683	
Extinction coefficient	0.0089(10)	
Largest diff. peak and hole	2.358 and -1.218 e.Å^{-3}	

Table 8 *Crystal data and structure refinement details for the co-crystal produced by reacting 1,4-diiodobutane and thiourea.*

Material	Pentane + Thiourea	
Empirical formula	C7 H18 I2 N4 S2	
Formula weight	476.17	
Temperature	296(2) K	
Wavelength	0.71073 Å	
Crystal system	Monoclinic	
Space group	$P2_1/c$	
Unit cell dimensions	a = 7.6126(3) Å	α= 90°.
	b = 22.5949(5) Å	β= 90.303(2)°.
	c = 9.0534(3) Å	γ = 90°.
Volume	1557.22(9) Å^3	
Z	4	
Density (calculated)	2.031 g/cm^3	
Absorption coefficient	4.288 mm^{-1}	
F(000)	904	
Crystal size	0.30 x 0.30 x 0.25 mm^3	
Theta range for data collection	1.80 to 28.27°.	
Index ranges	-10<=h<=10, -30<=k<=29, -12<=l<=12	
Reflections collected	5567	
Independent reflections	3435 [R(int) = 0.0229]	
Completeness to theta = 28.27°	89.2 %	
Absorption correction	Empirical	
Max. and min. transmission	0.4136 and 0.3594	
Refinement method	Full-matrix least-squares on F^2	
Data / restraints / parameters	3435 / 0 / 137	
Goodness-of-fit on F^2	1.107	
Final R indices [I>2sigma(I)]	R1 = 0.0378, wR2 = 0.0882	
R indices (all data)	R1 = 0.0443, wR2 = 0.0928	
Extinction coefficient	0.0159(7)	
Largest diff. peak and hole	1.028 and -0.630 e.Å^{-3}	

Table 9 *Crystal data and structure refinement details for the co-crystal produced by reacting 1,5-diiodopentane and thiourea.*

Material	Hexane & Thiourea	
Empirical formula	C9 H24 I2 N6 S3	
Formula weight	566.32	
Temperature	150(2) K	
Wavelength	0.71073 Å	
Crystal system	Monoclinic	
Space group	*P2$_1$/n*	
Unit cell dimensions	a = 5.97890(10) Å	α= 90°.
	b = 15.2850(6) Å	β= 91.459(2)°.
	c = 22.0067(8) Å	γ = 90°.
Volume	2010.48(11) Å^3	
Z	4	
Density (calculated)	1.871 g/cm^3	
Absorption coefficient	3.440 mm^{-1}	
F(000)	1096	
Crystal size	0.30 x 0.20 x 0.15 mm^3	
Theta range for data collection	1.62 to 28.78°.	
Index ranges	-8<=h<=8, -20<=k<=18, -29<=l<=29	
Reflections collected	7819	
Independent reflections	4865 [R(int) = 0.0309]	
Completeness to theta = 28.78°	93.2 %	
Absorption correction	Empirical	
Max. and min. transmission	0.6264 and 0.4251	
Refinement method	Full-matrix least-squares on F^2	
Data / restraints / parameters	4865 / 0 / 182	
Goodness-of-fit on F^2	1.083	
Final R indices [I>2sigma(I)]	R1 = 0.0582, wR2 = 0.1529	
R indices (all data)	R1 = 0.0843, wR2 = 0.1795	
Extinction coefficient	0.0141(10)	
Largest diff. peak and hole	1.830 and -1.376 e.Å^{-3}	

Table 10 *Crystal data and structure refinement details for the co-crystal produced by reacting 1,6-diiodohexane and thiourea.*

Material	Octane + Thiourea	
Empirical formula	C6 H16 I N4 S2	
Formula weight	670.50	
Temperature	150(2) K	
Wavelength	0.71073 Å	
Crystal system	Triclinic	
Space group	$P\bar{1}$	
Unit cell dimensions	a = 6.0463(2) Å	α= 87.970(2)°.
	b = 8.4495(3) Å	β= 80.012(2)°.
	c = 12.7157(6) Å	γ = 85.108(2)°.
Volume	637.31(4) Å^3	
Z	1	
Density (calculated)	1.747 g/cm^3	
Absorption coefficient	2.809 mm^{-1}	
F(000)	330	
Crystal size	0.25 x 0.20 x 0.08 mm^3	
Theta range for data collection	3.25 to 28.27°.	
Index ranges	-7<=h<=7, -11<=k<=11, -13<=l<=16	
Reflections collected	4462	
Independent reflections	3075 [R(int) = 0.0228]	
Completeness to theta = 28.27°	97.2 %	
Absorption correction	Empirical	
Max. and min. transmission	0.8065 and 0.5402	
Refinement method	Full-matrix least-squares on F^2	
Data / restraints / parameters	3075 / 0 / 119	
Goodness-of-fit on F^2	1.115	
Final R indices [I>2sigma(I)]	R1 = 0.0308, wR2 = 0.0716	
R indices (all data)	R1 = 0.0339, wR2 = 0.0744	
Extinction coefficient	0.070(3)	
Largest diff. peak and hole	1.506 and -1.202 e.Å^{-3}	

Table 11 *Crystal data and structure refinement details for the co-crystal produced by reacting 1,8-diiodooctane and thiourea.*

Material	Decane + Thiourea	
Empirical formula	C7 H18 I N4 S2	
Formula weight	698.54	
Temperature	150(2) K	
Wavelength	0.71073 Å	
Crystal system	Triclinic	
Space group	$P\bar{1}$	
Unit cell dimensions	a = 8.7877(3) Å	α= 105.673(2)°.
	b = 9.4753(3) Å	β= 112.177(2)°.
	c = 9.6865(5) Å	γ = 100.130(2)°.
Volume	683.31(5) Å^3	
Z	1	
Density (calculated)	1.698 g/cm^3	
Absorption coefficient	2.624 mm^{-1}	
F(000)	346	
Crystal size	0.35 x 0.35 x 0.10 mm^3	
Theta range for data collection	2.35 to 28.29°.	
Index ranges	-11<=h<=10, -11<=k<=12, -12<=l<=11	
Reflections collected	4496	
Independent reflections	3315 [R(int) = 0.0310]	
Completeness to theta = 28.29°	97.3 %	
Absorption correction	Empirical	
Max. and min. transmission	0.7794 and 0.4603	
Refinement method	Full-matrix least-squares on F^2	
Data / restraints / parameters	3315 / 0 / 128	
Goodness-of-fit on F^2	1.085	
Final R indices [I>2sigma(I)]	R1 = 0.0502, wR2 = 0.1147	
R indices (all data)	R1 = 0.0593, wR2 = 0.1219	
Extinction coefficient	0.062(3)	
Largest diff. peak and hole	2.976 and -2.090 e.Å^{-3}	

Table 12 *Crystal data and structure refinement details for the co-crystal produced by reacting 1,10-diiododecane and thiourea.*

6.4 Conclusions

Five new materials have been produced and their crystal structures have been obtained, these materials contain a large number of potential hydrogen bond donors and hydrogen bond acceptors but little evidence of hydrogen bonding is present in the crystal structure. These products exploit unusual reactivity but there are a small number of mentions in the literature[1-3] and SN_2 provides a plausible mechanism (SN_1 may be more prone to produce side products).

Given that the different chain lengths show substantial structural differences it is worth investigating whether a given $\alpha,\omega-$diiodoalkane can produce different structures according to solvent or preparation influences and preliminary experiments with different solvents have produced the 1,10-diiododecane/urea inclusion compound. Also it is important to note that the different materials show different thiourea:alkane ratios inside their crystal structure (4:1 for the n = 4 , 8 and 10 materials; 3:1 for the n = 6 material; and 2:1 for the n = 5 materials) and different numbers of non-reacting thiourea (2, 1, 0). Clearly thiourea can form many different structures with straight chains so it seems plausible that varying the ratios of the starting materials could yield co-crystals with different ratios.

Only one material was produced using an odd chain length $\alpha,\omega-$diiodoalkane but it is likely that other odd chain length $\alpha,\omega-$diiodoalkanes react similarly. Other iodoalkane chains may also be able to react in a similar manner, particularly $\alpha-$iodoalkanes and branched diiodoalkanes. If these chains demonstrate the same reactivity then it is likely that they will form interesting structures of their own. $\alpha,\omega-$dibromoalkanes and $\alpha,\omega-$dichloroalkanes have also been mixed with thiourea but no co-crystals were produced.

6.5 References

[1]   J.-P. Collin, D. Jouvenot, M. Koizumi, J.-P. Sauvage, *Inorg. Chim. Acta*, **2007**, 360(3), 923–930.

[2]   E. Anklam, *Synthesis-Stuttgart*, **1987**, 9, 841-843.

[3]   S. E. Drewes, M. W. Drewes, I. J. McNaught, *S. Afr. J. Chem.,* **1985**, 38(1), 12-16

[4]   G. M. Sheldrick, *Acta Crystallogr. A*, **2008**, 64, 112-122.

Chapter 7 – Conclusions and Further work.

This thesis successfully details:

- The development of new experimental techniques to study solid materials (X-ray Birefringence Imaging);

- The application of *in-situ* techniques to further our understanding of crystallization processes (*In-Situ* Solid-State NMR);

- The production of new crystalline materials (α,ω-diiodoalkane + thiourea Co-Crystals)

These achievements fulfil the initial aims of the project and in each case there is great scope to continue the work and further our scientific understanding. Each category will now be examined to note what was accomplished and to consider further avenues of investigation.

7.1.1 X-ray Birefringence Imaging

X-ray Birefringence Imaging (XBI) is a new technique for the spatially resolved investigation of the local orientation of specific energy-matching bonds (C−Br bonds in the current work). Despite still being in its infancy this technique has already achieved a great deal of interest[1, 4] and we hope to fully realize the potential of this new strategy. Specifically we aim to conduct XBI experiments on different elements (demonstrating that it is more versatile than just looking at bromine), and new materials (investigating if XBI can provide unique insight on liquid crystals and mesogenic materials) to ascertain the strengths and limitations of XBI.

XBI has been recently performed on organometallic inclusion compounds, specifically ferrocene/thiourea, benzene chromium tricarbonyl/thiourea and cyclohexadiene iron tricarbonyl/thiourea. These materials were selected on the criteria of a) attainable x-ray energies, b) relatively simplistic bonding, c) relatively easy to produce and d) the possibility of interesting temperature dependence. These experiments probed

the iron K-edge (7.1 keV) and chromium K-edge (6.0 keV). XBI experiments at these wavelengths encountered some complications due to X-ray absorption by the air which reduced the transmitted signal but satisfactory data was achieved using slightly longer exposure times. These experiments show that XBI is sensitive to iron and chromium absorption edges so it is not limited to merely bromine, additionally it shows XBI is effective on atoms that form multiple bonds so it is not limited to single-bonding atoms. However simple bonding behaviour does make it easier to predict the X-ray axis and also to relate observed birefringence back to bond orientations.

Further XBI experiments are scheduled from on beamline B16 at Diamond Light Source, with the goal of investigating the iodine K-edge (33.2 keV) and the sulphur K-edge (2.47 keV) in certain inclusion compounds, namely 1-iodoadamantane/thiourea, iodocyclohexane/thiourea, 4-aminothiophenol/thiourea and 1-methylpyridinium-4-thiolate/thiourea. During this beamtime we plan to perform the sulphur experiments using a helium tube to minimize X-ray absorption by the air.

Additional beamtime has been scheduled for XBI experiments on liquid crystals and bending crystals at the bromine and iodine K-edges. Materials with mesogenic or disordered properties are a particularly interesting avenue for XBI because the lack of crystallinity makes these materials unsuitable for XRD yet anisotropic bond orientations should still be detectable by XBI.

7.1.2 *In-Situ* NMR

We have gathered good data on the mixed guest α,ω-dibromoalkane + alkane / urea inclusion compounds but clearly there is great scope to expand this work. In our experiments we did not see any evidence of transition states or intermediates, we did see evidence of peak splitting by neighbour environment which contains information about guest ordering with the solid, we did observe loss of liquid / solution signal and gain of solid signal over the crystallization process.

We have investigated three different combinations of guest molecules but this represents only a small portion of the different alkanes and haloalkanes capable of forming

inclusion compounds with urea. These alternative guest molecules may show slightly different behaviour or might allow us to extract different information. Guest molecules with iodine end-groups are particularly interesting as they give rise to very large splitting effects by neighbour environment. Another interesting avenue of research is in mono-halogen alkane guest molecules such as α-bromoalkanes where the population of number of CH_2Br sites must equal the population of CH_2CH_3 and CH_3 sites. Guests of this type would make it easier to assess guest ordering within the inclusion compound and would also provide insight on the different signal intensities of different carbon positions (which can be related back to lattice relaxation times).

7.1.3 Co-crystals of α,ω-Diiodoalkanes and Thiourea

The discovery of these materials opens up many possibilities for producing new co-crystals. This iodine sulphur replacement reaction proceeds under mild conditions and gives range to significantly different structures for slightly different chain lengths. If this reactivity occurs with other types of iodoalkanes (e.g. branched or mono-substituted alkanes) then this procedure could produce a large number of new and varied co-crystals.

7.2 Conclusions

In our XBI experiments we have pioneered a new experimental technique using the urea and thiourea host structures as a directing influence to simplify the behaviour of our test materials i.e. using model materials to develop new techniques. In our *In-Situ* NMR experiments we have utilized existing techniques (recently pioneered by our group) to better our understanding of the urea inclusion compound crystallization process i.e. using documented techniques to better understand unknown processes. In our α,ω-diiodoalkanes and thiourea experiments we have produced new materials i.e. using chemical knowledge to develop new materials.

7.3 References

[1]   B. A. Palmer, G. R. Edwards-Gau, B. M. Kariuki, K. D. M. Harris, I. P. Dolbnya, S. P. Collins, *Science*, **2014**, 344, 1013-1016

[2]   S. Lidin *Science*, **2014**, 344, 969-970

[3]   J. P. Sutter, I. P. Dolbnya, S. P. Collins, K. D. M. Harris, G. R. Edwards-Gau, B. A. Palmer, *J. Appl. Phys.*, **2015**, 117, 164902

[4]   B. A. Palmer, G. R. Edwards-Gau, B. M. Kariuki, K. D. M. Harris, I. P. Dolbnya, S. P. Collins, J. P. Sutter, *J. Phys. Chem. Lett.*, **2015**, 6, 561-567